

國立交通大學

電子物理研究所

博士論文

液態晶體於兆赫波段之元件設計與測量

Design and Measurement of Liquid Crystals Devices in

Terahertz Frequency Range

研究生：謝卓帆

指導教授：趙如蘋 教授

潘犀靈 教授

中華民國九十八年七月

液態晶體於兆赫波段之元件設計與測量

Design and Measurement of Liquid Crystals Devices in Terahertz

Frequency Range

研究生：謝卓帆

Student : Cho-Fan Hsieh

指導教授：趙如蘋 教授

Advisor : Prof. Ru-Pin Pan

潘犀靈 教授

Prof. Ci-Ling Pan



Submitted to Department of Electrophysics

College of Science

National Chiao Tung University

in partial Fulfillment of the Requirements

for the Degree of

Doctor of Philosophy

in

Electrophysics

July 2009

Hsinchu, Taiwan, Republic of China

中華民國九十八年七月

# 液態晶體於兆赫波段之元件設計與測量

學生：謝卓帆

指導教授：趙如蘋 教授  
潘犀靈 教授

國立交通大學  
電子物理研究所 博士班

## 摘要

目前兆赫波段之元件相當缺乏，大部分元件有著可調範圍過小及操作溫度過低的缺點。我們已成功的研究出一種利用磁場對液晶作用之可調變的相位延遲器，並進一步製作應用性較高的電控液晶相位延遲器，這些元件皆可在室溫下操作且其調變量皆大於  $2\pi$ ，並以此元件為基礎設計可調波長之二色性濾波器。

另一方面我們使用二維金屬孔洞陣列之異常穿透光特性，在兆赫波段下達到濾波的效果。其狹窄的穿透頻帶及其高的穿透率讓此類研究受到重視，可惜的是此穿透頻率是固定的。於是我們利用旋轉磁場控制液晶分子方向，搭配二維金屬孔洞陣列，成功的製作出兆赫波段下之磁控可調濾鏡。

除了上述與頻率相關之元件外，利用液態晶體具有雙折射特性與參考光學邦加球，我們設計並製作與頻率無關的四分之一波板。此四分之一波板在特定頻率範圍下皆可適用(0.20 到 0.50 THz)且可藉由控制液態晶體，使其可適用範圍改變到 0.30 到 0.70 THz。

上述元件對於兆赫波之實用化及對材料之非破壞性檢測，有很大的助益。

# Design and Measurement of Liquid Crystals Devices in Terahertz Frequency Range

Cho-Fan Hsieh

Advisors: Prof. Ru-Pin Chao Pan

Prof. Ci-Ling Pan

Doctor of Philosophy in Department of Electrophysics

National Chiao-Tung University

## Abstract

Presently, optical components are short in the terahertz (THz) frequency range. Most THz tunable devices have the problems with small tunable range and cryogenic operating temperature. We have demonstrated a magnetically controlled liquid-crystal (LC) THz phase shifter. In addition, we study and design the electrically controlled LC-based THz phase shifter. Tunable phase shift up to  $360^\circ$  at 1 THz is achieved and can be operated over a broad range near room temperature. These components are used to solve the current lack of the THz birefringent filter.

The filter is an important component in optics. It has been shown that a two-dimensional metallic-hole array (2-D MHA) can work as a filter for THz waves. The narrow central frequency and high efficiency of the MHA draws much attention. Previously, we have measured the temperature-dependent refractive indices of LCs (5CB and E7) in THz range. The measured results show that the LCs have large birefringence ( $\sim 0.2$ ) and small absorption. Here we use a rotary magnetic field to rotate the direction of the LC molecules. Then we combine the characteristics of the MHA to design a magnetically tunable THz filter.

Nonetheless, traditional birefringent devices can be used only at a single corresponding frequency, because the phase retardation has strong wavelength dependence. An achromatic tunable THz birefringence quarter-wave plate is demonstrated. The phase retardation of this device is  $90^\circ \pm 9^\circ$  from 0.20 to 0.50 THz and the operation range could be changed from 0.30 to 0.70 THz by using magnetically controlled birefringence in three nematic liquid crystal phase retarders. The above mentioned devices can promote the practicability of THz biological material nondestructive testing.

## 致 謝

博士班能畢業，要感謝的人很多。

父母親與叔叔阿姨的拉拔與在經濟上的支持，趙如蘋老師與潘犀靈老師在學術上與做人處事上的指導，親朋好友在生活上的扶持陪伴與同窗夥伴在實驗上的合作幫助。

交大這七年，不管在課業上、做人處事上與日常生活上，皆成長了許多，過得也相當充實。

這七年的點滴將會永遠銘記在心。希望往後的日子，大家都能順順利利平平安安，追求自己的夢想並繳出漂亮的成績單。



卓帆

# Contents

中文摘要	i
Abstract	ii
致謝	iii
Contents	iv
List of Figures	vi
<b>Chapter 1. Introduction</b>	
1.1. Terahertz Technology	2
1.2.	4
1.2.1. Generation of Wide Band THz Signal by Using Photoconductive Antennas	4
1.2.2. Detection of Wide Band THz Signal by Using Photoconductive Antennas	5
1.2.3. Terahertz Time-Domain Spectroscopy System (THz-TDS)	7
1.3. Nematic Liquid Crystals	8
1.3.1. Deformation Energy of NLCs	8
1.3.2. Birefringence of NLCs	9
1.3.3. Variety Combination of Alignment	10
1.4. Optical Properties of Metallic Hole Arrays in Sub-wavelength Frequency Range	11
1.4.1. Guiding Mode of MHA	11
1.4.2. Surface Plasmons (SPs) Mode of MHA	14
<b>References</b>	17
<b>Figures</b>	19
<b>Chapter 2. Optical Constants and Birefringence of Nematic Liquid                 Crystals PCH-5 and E7 in Terahertz Frequency Range</b>	25
2.1. Nematic Liquid Crystal PCH-5 and E7	25
2.2. Nematic Liquid Crystal in THz Wave	25
2.3. Experimental Methods	26
2.4. Determination of Optical Constants	27
2.5. Results and Discussions of PCH-5	29
2.5.1. Complex Optical Constants	29
2.5.2. Temperature Dependence	30
2.5.3. Birefringence and Order Parameter	31

2.6.	Complex Optical Constants of E7 in THz Frequency Range	32
2.7.	Conclusions	33
	<b>References</b>	34
	<b>Figures</b>	36
<b>Chapter 3.</b>	<b>Tunable Room-Temperature Terahertz Phase Shifter</b>	
	<b>Based on Controlled Birefringence in Nematic Liquid Crystals</b>	41
3.1.	Phase Shifters	41
3.2.	Phase Shifter Based Nematic Liquid Crystals	43
3.3.	Magnetically Tunable Liquid-Crystal-Based Terahertz Phase Shifter	45
3.4.	Electrically Tunable Liquid-Crystal-Based Terahertz Phase Shifter	49
3.5.	Discussion	57
	<b>References</b>	60
	<b>Figures</b>	62
<b>Chapter 4.</b>	<b>Control of Extraordinary Transmission of Metallic Holes</b>	
	<b>Array by Nematic Liquid Crystal</b>	75
4.1.	Metallic Holes Array	75
4.2.	Theoretical Prediction	77
4.3.	Experimental Methods	78
4.4.	Results and Discussions	80
4.5.	Summary	83
	<b>References</b>	85
	<b>Figures</b>	87
<b>Chapter 5.</b>	<b>A Liquid-Crystal-Based Tunable Terahertz Achromatic</b>	
	<b>Quarter-Wave Plate</b>	91
5.1.	Achromatic Quarter-Wave Plate	91
5.2.	Experiment	92
5.3.	Result	95
	<b>References</b>	97
	<b>Figures</b>	99
<b>Chapter 6.</b>	<b>Conclusion</b>	102
<b>Appendix Sample dimensions</b>		
<b>Biography</b>		

# Chapter 1 Introduction

Every frequency of electromagnetic wave is a treasury. The terahertz (THz) spectrum ranges from 100 GHz to 10 THz ( $10^9$  to  $10^{13}$  Hz) as shown in Fig. 1.1.1 The wavelength of THz signals corresponds to from 3 to 0.03 mm, and lies between the microwave and infrared regions. At sub-THz frequencies, microwaves and millimeter-waves can be investigated by electronic devices such as those components in cell phones. At super-THz frequencies, near-infrared and visible light are exploited by optical devices such as the semiconductor lasers. THz wave is quite wide band, but undeveloped due to the deficient in generators and detectors.

THz science ranges from investigations of ultrafast dynamics in materials to biological tissue imaging. In the past two decades, the development of ultrashort pulse (~fs) lasers and advanced optoelectronic THz-devices create a new era of THz technologies. For promotion of THz applications, quasi-optic components such as phase shifters, grating, polarizers and filters are indispensable.

On the other hand, Ebbesen et al. first explored abnormal transmission of visible light through a sub-wavelength metallic holes array (MHA) [1] in 1998. The most scientists consider these unusual phenomena are arisen from the coupling between the incident electromagnetic waves and the surface plasmon polaritons (SPPs) of MHA [2]. Since the dimensions of MHA must lie on the order of wavelength. For this



reason, it is much easier to fabricate THz MHA.

However, many tunable THz devices have the common problems that are small tunability and cryogenic operating temperature. Liquid crystals (LCs) are well known for its large birefringence which can be easily controlled by external field at ambient temperature. The LC-based devices have been explored in visible and infrared regime [3, 4]. Here, we propose to study the optical properties of Liquid crystals (LCs) in THz range and then design the LC based tunable THz devices with MHA. We believe that the investigations and applications of LC-THz optics should improve THz technologies.

## 1.1 Terahertz Technology

Mourou and Auston et al. first demonstrated the generation and detection of time resolved pulse THz radiation by photo-conducting switch with phase-lock technique [5, 6]. In 1996, Zhang et al. developed free-space electro-optic sampling technique to enhance the THz signal (S/N ratio is beyond  $10^3$  in amplitude spectrum) [7]. This dramatic progress was made by applying semiconductor sciences and ultrafast laser. Now, THz techniques have been utilized in spectroscopy and inspection. The spectroscopic technique by using pulsed THz radiation is called “THz time-domain spectroscopy (THz-TDS)” [8]. THz-TDS is a powerful technique that allows broadband THz generation and detection for the field and phase of the THz

wave. Our system is depicted in Fig. 1.2.1. The mode-locked femtosecond Ti:sapphire laser (Spectra Physics, Tsunami) is split into two beams by a beam splitter; one is pump beam, the other is labeled as probe beam. The pulse width and the repetition rate of the light are 100 fs and 90 MHz, respectively. The pump pulses are illuminated on a low-temperature grown (LTG) GaAs photoconductive dipole antenna (Fig. 1.2.2) to emit THz signals. The average power of pump pulse is about 35 mW. The antennas are gated by pump pulses to produce electro-hole pairs. The bias 5 volt (rms) with ac frequency 5 kHz is applying to the dipole antenna. These carriers are accelerated by applying electric field and then produce a photocurrent to radiate THz signals. A hemispherical silicon substrate lens attached to the antenna to reduce the effect of multiple reflections within the LTG-GaAs substrate. The generated THz pulses are collected and guided by one gold-coated off-axis parabolic mirrors onto the sample. The transmitted pulses from the sample are focused by another parabolic mirror onto the THz detector which is also a photoconductive antenna. The transmitted THz pulse was monitored by the probe beam from the same laser with the same type of antenna. The average power of probe pulse is 15mW. The transient of detector is connected to a lock-in amplifier (Stanford Research Systems, Model SR830). By moving a delay stage, it is possible to monitor the time evolution of the THz pulse field.

## 1.2.1 Generation of Wide Band THz Signal by Using Photoconductive Antennas

When the ultra-short pulse is incident to photoconductive antenna, then free electron-hole pairs are excited. The time dependence of carrier density is given by:

$$\frac{dn}{dt} = -\frac{n}{\tau_c} + G, \quad (1.2.1)$$

where  $n$  is the density of the carrier,  $G$  is the generation rate of the carrier by the light pulse and  $\tau_c$  is the carrier trapping time. Photo carriers are accelerated by applying bias on the electrodes of antenna. The acceleration of carriers in the electric field is:

$$\frac{dv_c}{dt} = -\frac{v_c}{\tau_s} + \frac{q_c}{m_c} E, \quad (1.2.2)$$

where  $v_c$  is the average velocity of the carrier,  $q_c$  is the charge of the carrier (an electron or a hole),  $m_c$  is the effective mass of the carrier (electron or hole),  $\tau_s$  is the momentum relaxation time, and  $E$  is the electric field. The local electric field  $E$  is smaller than the applied bias electric field,  $E_b$ , due to the shielding effects of the space charges,

$$E = E_b - \frac{P}{\alpha \epsilon}, \quad (1.2.3)$$

where  $P$  is the induced polarization due to the spatial distance of the electron and hole,  $\epsilon$  is the dielectric constant of the LTG-GaAs, and  $\alpha$  is the geometrical factor of the photoconductive material. By considering screening effect of the electric field, the

time dependence of polarization  $P$  can be written as

$$\frac{dP}{dt} = -\frac{P}{\tau_r} + J, \quad (1.2.4)$$

where  $\tau_r$  is the recombination time between an electron and hole ( $\tau_r=10$  ps for LTG-GaAs).  $J$  is the current density contributed by an electron and hole,

$$J = env_h - env_e, \quad (1.2.5)$$

where  $e$  is the electric charge. According to Maxwell's equations, the change of acceleration of electrons leads to radiation of electromagnetic wave. In a simple

Hertzian dipole theory, the far-field of the radiation  $E_{THz}$  is proportional to  $\frac{\partial J}{\partial t}$ .

We introduce a different speed  $v$  between an electron and hole,  $v = v_h - v_e$ , then the electric field of THz wave can be expressed as,

$$E_{THz} \propto ev \frac{\partial n}{\partial t} + en \frac{\partial v}{\partial t}. \quad (1.2.6)$$

## 1.2.2 Detection of Wide Band THz Signal by Using Photoconductive Antennas

We measure THz field by tracing the photocurrent which is induced by the simultaneous arrival of the THz pulse and the gating probe beam in the detector [9].

The non-instantaneous conductivity of the detector  $\sigma_d$ , the transient  $J$  induced by the arrival THz electric field at time  $t_p$  is:

$$J(t_p) = \int_{t_p}^{\infty} E_{THz}(t') \sigma_d(t' - t_p) dt'. \quad (1.2.7)$$

The conductivity can be described as

$$\sigma_d(t' - t_p) = \begin{cases} 0 & \text{if } t_p > t' \\ \frac{\sigma_0}{\tau_d} \exp\left[\frac{-(t' - t_p)}{\tau_d}\right] & \text{if } t_p \leq t' \end{cases} \quad (1.2.8)$$

where  $\sigma_0$  is the peak conductivity of photoconductive antenna. The rise in the conductivity can be assumed to be a short duration because of the gating optical pulse.

It is assumed that  $\tau_d \gg t' - t_p$ , and  $\sigma_d(t' - t_p)$  can be rewritten as

$$\sigma_d(t' - t_p) = \begin{cases} 0 & \text{if } t_p > t' \\ \frac{\sigma_0}{\tau_d} & \text{if } t_p \leq t' \end{cases} \quad (1.2.9)$$

Substitution of Eq. (1.2.9) into Eq. (1.2.7) which is obtained

$$J_p(t_p) = \frac{\sigma_0}{\tau_d} \int_{t_p}^{\infty} E_{THz}(t') dt', \quad (1.2.10)$$

The radiated THz waveform is assumed to be symmetric, then

$$J \approx \frac{\sigma_0}{2\tau_d} \int_{-\infty}^{\infty} E_{THz}(t') dt', \quad (1.2.11)$$

Because there is the interface between the back side of LTG GaAs and free space, the Fresnel reflection formulas must be considered. It indicates that the field of

the transmitted pulse is decreased relative to its initial value by the factor

$$\frac{2\sqrt{n}}{n+1}, \quad (1.2.12)$$

where  $n$  is the index of refraction of the LTG-GaAs at THz frequency range.

In short, the current density  $J$  is relative to the THz electric field and the response function of the detector. The carrier life time and transmission characteristics of LTG-GaAs, resonance characteristics of dipole or bow-tie antenna, pulse waveform and power distribution of probe beam, and diffraction effect of the THz beam and so on, all parameters affect the transient response of the THz detection.

### 1.2.3 Terahertz Time-Domain Spectroscopy System (THz-TDS)

Because electronic detectors are too slow to measure the THz transients directly, repetitive photoconductive sampling is used. Converting LTG-GaAs antenna to a THz detector, a current-to-voltage lock-in amplifier is connected to the electrodes of antenna. The electric field of the THz wave provides the driving field to the photocarriers. The time dependent transient through the gate varies with both the magnitude and direction of THz wave. The lifetime of photocarrier,  $\tau$  is much shorter ( $\sim$ fs) than the THz pulse ( $\sim$ ps), the photoconductive switch acts as a sampling gate which characterizes the THz field within  $\tau$ . Figure 1.2.3 shows how the THz waveform is traced by using femtosecond pulse and changing the optical delay line. The spot size of THz wave is about 2 cm.

Figure 1.2.4 (a) is the experimental data of the time domain THz signal passing through the air with and without  $N_2$  purge. The pulse after main signal is smoother

under dry air condition while the tail of pulse fluctuates severely under wet air condition due to vapor absorption. By applying Fast Fourier Transform (FFT) to THz time domain signal, the spectrum in frequency domain is obtained as shown in Fig.

1.2.4 (b). There are nine absorption lines below 1.5 THz [10].

## 1.3 Nematic Liquid Crystals

The first observation and discovery of liquid crystalline materials behavior were made in 1888 by Reinitzer and Lehmann [11, 12]. The most common LC phase is the nematic phase. The LCs used in this thesis are all rod-like and thermotropic nematic LCs. Thermotropic LC exhibits temperature-dependent phase transition (Fig. 1.3.1).

Nematic liquid crystal (NLC) materials summarily have following characteristics:

1. LC phase is located between the crystalline solid and the isotropic liquid.
2. LC has strongly anisotropic property in molecular shape (rod-like or disc-like), refractive index, dielectric constant and permeability.
3. The molecules are spontaneously oriented with an identical axis, labeled as director. The states of the director  $\hat{n}$  and  $-\hat{n}$  are indistinguishable in NLC.

Nematics could be uniaxial. The director usually varies from different positions in the medium. The particularly treated surface of LC cell can be utilized to orientate director [13]. A uniformly aligned sample is optically and electrically anisotropic.

### 1.3.1 Deformation Energy of NLCs

If the NLC molecules don't orientate parallel to each other due to external forces (such as electric or magnetic field), there are three types of the deformation (splay, twist, and bend) occurring in NLCs as shown in Fig. 1.3.2 [14]. Briefly, the LC molecules tend to align parallel or perpendicular to the external field and the extra energy density is a function of the direction and magnitude of the field. In a strong boundary case, the LC molecules near the substrate will be strongly aligned and some deformations exist in the bulk due to the principle of the lowest total energy. If we apply a external electric/magnetic field to a LC cell, the total energy  $F$  is described as

$$F = \int (f_d + f_{E/M}) d\rho, \quad (1.3.1)$$

where the  $f_d$  and  $f_{E/M}$  are the energies from the deformation and the external field and  $\rho$  is the unit volume. From Eq. 1.3.1, the deformation energy dominates mainly in weak fields whereas the field term dominates in strong fields. According to the continuum theory, the director spatially varies slowly and smoothly.

### 1.3.2 Birefringence of NLCs

Let's define the birefringence. The difference between refractive indices measured with polarization parallel or normal to director is very large. The ordinary index of refraction  $n_o$  is for light with the polarization direction perpendicular to the director and the extraordinary refractive index  $n_e$  is for light with the electric field direction parallel to the director. The birefringence of the nematic is defined as [15]



$$\Delta n = n_e - n_o, \quad (1.3.2)$$

When the incident polarization of light is not perfect parallel or perpendicular to the director, the effective index of the refraction is

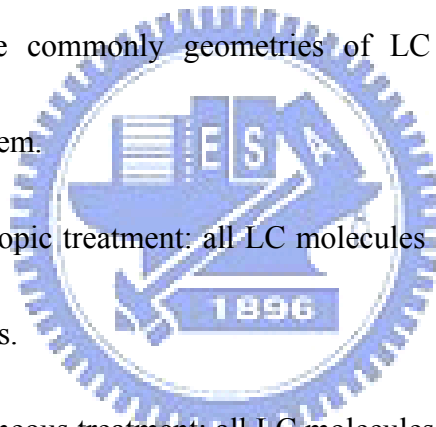
$$n_{eff} = \left( \frac{\sin^2 \theta}{n_e^2} + \frac{\cos^2 \theta}{n_o^2} \right)^{-1/2}, \quad (1.3.3)$$

where  $\theta$  is the angle between the propagation directions of the incident light and the optical axis. Therefore, the effective birefringence is  $\Delta n = n_{eff} - n_o$ .

### 1.3.3 Variety Combination of Alignment

Here we list some commonly geometries of LC cells and give a simple explanation to each of them.

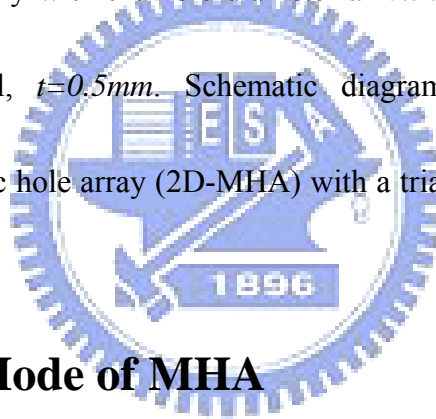
- (1) Homoetropic treatment: all LC molecules are vertical aligned to both substrates.
- (2) Homogeneous treatment: all LC molecules are parallel aligned to both substrates and have the same director.
- (3) Hybrid treatment: LC molecules are vertical to one substrate, but parallel to the other substrate; therefore, LC directors are continuously changed between both substrates.
- (4) Twisted treatment: all LC molecules are parallel aligned to both substrates, but the alignment direction of each substrates are mutually orthogonal.



## 1.4 Optical Properties of Metallic Hole Arrays in Sub-wavelength Frequency Range

Metal films perforated with two-dimensional periodic array of holes exhibit extraordinary transmission in sub-wavelength frequency range [1]. This is worthy to explore its potential applications for subwavelength optics. The enhanced power transmittance and specific phase ripple result from the effective resonance. It is due to the coupling mode of incident light with metallic surface [2] and cavity. The enhanced peak changes significantly with the hole diameter  $d=0.56mm$ , pitch  $s=0.99mm$ , and thickness of the metal,  $t=0.5mm$ . Schematic diagram and real picture of a two-dimensional metallic hole array (2D-MHA) with a triangular lattice are shown in

Fig. 1.4.1.



### 1.4.1 Guiding Mode of MHA

Consider a cylindrical hole made by metal with radius  $a$ . Time-harmonic electric and magnetic field equations can be written as [16]:

$$\begin{aligned}\nabla^2 E + k^2 E &= 0 \\ \nabla^2 H + k^2 H &= 0\end{aligned}\tag{1.4.1}$$

We can decompose the 3-D Laplacian operator  $\nabla^2$  into two components:  $\nabla_r^2$  and  $\nabla_z^2$  for transverse and longitudinal parts, respectively.

For TM waves in cylindrical waveguides,  $H_z = 0$  and  $E_z \neq 0$ , all fields can be expressed in terms of  $E_z = E_z^0 e^{-\gamma z}$ , where  $E_z^0$  satisfies the homogeneous

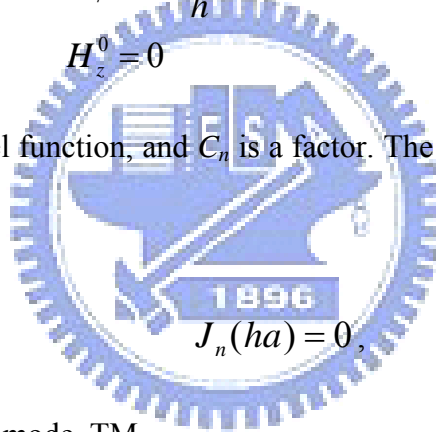
Helmholtz equation

$$E_z(r, \phi, z) = E_z^0(r, \phi)e^{-\gamma z}. \quad (1.4.2)$$

The solutions are as follows,

$$\begin{aligned} E_z^0 &= C_n J_n(hr) \cos n\phi \\ E_r^0 &= -\frac{i\beta}{h} C_n J_n'(hr) \cos n\phi \\ E_\phi^0 &= -\frac{i\beta n}{h^2 r} C_n J_n(hr) \sin n\phi \\ H_r^0 &= -\frac{i\omega\varepsilon n}{h^2 r} C_n J_n(hr) \sin n\phi \\ H_\phi^0 &= -\frac{i\omega\varepsilon}{h} C_n J_n'(hr) \cos n\phi \\ H_z^0 &= 0 \end{aligned}, \quad (1.4.3)$$

where  $i\beta = \gamma$ ,  $J_n$  is Bessel function, and  $C_n$  is a factor. The boundary condition is  $E_z^0 = 0$  at  $r = a$ :



$$J_n(ha) = 0, \quad (1.4.4)$$

For the fundamental TM mode,  $TM_{01}$ ,

$$(h)_{TM_{01}} = \frac{2.405}{a}, \quad (1.4.5)$$

and then the lowest cutoff frequency is:

$$(f_c)_{TM_{01}} = \frac{(h)_{TM_{01}}}{2\pi\sqrt{\mu\varepsilon}} = \frac{0.383}{a\sqrt{\mu\varepsilon}} \text{ (Hz)}, \quad (1.4.6)$$

For TE waves in cylindrical waveguides,  $E_z = 0$  and  $H_z \neq 0$ , all fields can be expressed

in terms of  $H_z = H_z^0 e^{-\gamma z}$ , where  $H_z^0$  satisfies the same homogeneous Helmholtz

equation

$$H_z(r, \phi, z) = H_z^0(r, \phi)e^{-\gamma z}, \quad (1.4.7)$$

The solutions are as below

$$\begin{aligned} H_z^0 &= C_n' J_n(hr) \cos n\phi \\ H_r^0 &= -\frac{i\beta}{h} C_n' J_n'(hr) \cos n\phi \\ H_\phi^0 &= \frac{i\beta n}{h^2 r} C_n' J_n(hr) \sin n\phi \\ E_r^0 &= \frac{i\omega\mu n}{h^2 r} C_n' J_n(hr) \sin n\phi \\ E_\phi^0 &= \frac{i\omega\mu}{h} C_n' J_n'(hr) \cos n\phi \\ E_z^0 &= 0 \end{aligned}, \quad (1.4.8)$$

where  $C_n'$  is also a factor. The boundary condition is  $H_z^0 = 0$  at  $r = a$ :

$$J_n'(ha) = 0, \quad (1.4.9)$$

For the lowest TE mode,  $TE_{11}$ ,

$$(h)_{TE_{11}} = \frac{1.841}{a}, \quad (1.4.10)$$

the lowest cutoff frequency for TE mode is:

$$(f_c)_{TE_{11}} = \frac{(h)_{TE_{11}}}{2\pi\sqrt{\mu\varepsilon}} = \frac{0.293}{a\sqrt{\mu\varepsilon}} \text{ (Hz)}, \quad (1.4.11)$$

from Eq 1.4.6 and 1.4.11, the lowest cutoff frequency for an infinitely long cylindrical

waveguide is determined by TE mode

$$v_{cutoff} = 1.841 \frac{c}{\pi d}, \quad (1.4.12)$$

where  $d = 2a$  is the diameter of hole and  $c$  is the speed of light in vacuum.

## 1.4.2 Surface Plasmons (SPs) Mode of MHA

A p-polarized electromagnetic wave passes along the interface between dielectric material ( $\epsilon_d$ ) and metal ( $\epsilon_m$ ) in the x-direction. The interface locates at  $z=0$  as shown in Fig. 1.4.2.

Every electromagnetic wave must obey the Maxwell's equations, and then considering the boundary conditions, we can obtain the following results:

$$k_{xd} = k_{xm} \equiv k_x = \frac{\omega}{c} \left( \frac{\epsilon_d \epsilon_m}{\epsilon_d + \epsilon_m} \right)^{1/2}, \quad (1.4.13)$$

This is the wave number formula for the surface plasmons in metal. From Eq. 1.4.13, we can find that

$$k_x = \frac{\omega}{c} \left( \frac{\epsilon_d \epsilon_m}{\epsilon_d + \epsilon_m} \right)^{1/2} > \frac{\omega}{c} \epsilon_d^{1/2}, \quad (1.4.14)$$

The wave vector of electromagnetic wave in the surface plasmon form is larger than the incident wave. Figure 1.4.3 shows the dispersion relation of the incident electromagnetic wave in dielectric medium and the surface plasmon in metal.

These two curves never cross with each other so the regular incident photons can't couple with surface plasmon polaritons (SPPs). However, periodic structures in the metallic film can result in the extra in-plane momentum which links the incident photons and SPP modes [17]. The corresponding relation for conservation of

momentum is

$$\vec{k}_{sp} = \vec{k}_x + \vec{k}_y + n\vec{G}_x + m\vec{G}_y, \quad (1.4.15)$$

where  $\vec{k}_{sp}$  is the wave vector in the SPP mode,  $\vec{k}_x$  and  $\vec{k}_y$  are the components of the wave vector of the incident light that lies in the interface,  $\vec{G}_x$  and  $\vec{G}_y$  are the wave vector components resulted from the two-dimensional periodic structure, and  $n$  and  $m$  are integers.

For normal incidence,

$$k_{sp} = \frac{\omega}{c} \left( \frac{\varepsilon_d \varepsilon_m}{\varepsilon_d + \varepsilon_m} \right)^{\frac{1}{2}} = n\vec{G}_x + m\vec{G}_y, \quad (1.4.16)$$

where  $\omega$  is the frequency of the incident signal,  $c$  is the speed of light in vacuum,  $\varepsilon_d$  and  $\varepsilon_m$  are the dielectric constant of the dielectric medium and the metal, respectively. The complex propagation constant for the SPP wave can be presented as

$k_{sp} = k_{spr} + ik_{spi}$  due to the complex dielectric constant of metal [18]

$$k_{spr} = \frac{\omega}{c} \left[ \frac{\varepsilon_d}{(\varepsilon_{mr} + \varepsilon_d)^2 + \varepsilon_{mi}^2} \right]^{\frac{1}{2}} \left[ \varepsilon_d \varepsilon_{mr} + \varepsilon_{mr}^2 + \varepsilon_{mi}^2 \right]^{\frac{1}{2}}, \quad (1.4.17)$$

$$k_{spi} = \frac{\omega}{c} \left[ \frac{\varepsilon_d}{(\varepsilon_{mr} + \varepsilon_d)^2 + \varepsilon_{mi}^2} \right]^{\frac{1}{2}} \left[ \varepsilon_d \varepsilon_{mi} \right]^{\frac{1}{2}}$$

where  $\varepsilon_{mr}$  and  $\varepsilon_{mi}$  are the real and imaginary components of the dielectric constant of the metal, respectively. In the THz frequencies range,  $\varepsilon_{mi} > |\varepsilon_{mr}|$  and  $|\varepsilon_{mr}|, \varepsilon_{mi} \gg \varepsilon_d$ , the real part of the SPP propagation constant is simplified as

$$k_{spr} \simeq \frac{\omega}{c} \sqrt{\epsilon_d}, \quad (1.4.18)$$

and the imaginary part of the SPP propagation constant is simplified as

$$k_{spi} = \frac{\omega}{c} \frac{\epsilon_d}{\epsilon_{mi}^{\frac{1}{2}}}, \quad (1.4.19)$$

At normal incidence, in 2-D triangular metallic hole array, the SPP frequency is

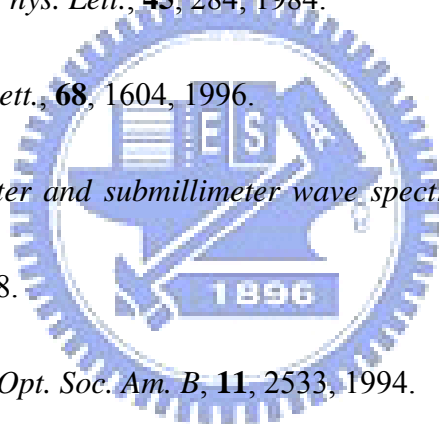
$$\nu_{sp} = \frac{2c}{s\sqrt{3}}, \quad (1.4.20)$$

where  $s$  is the hole spacing.

Figure 1.4.4 is the experimental data of transmittance of 2D triangular aluminum hole array in THz frequency range. The dimensions of this sample are in legend of Fig. 1.4.4. The data are in good agreement with theoretic prediction. There is a resonant peak at 0.3 THz. From Eq. 1.4.19, there is no power loss in this SPP resonant frequency.

## References:

1. T.W. Ebbesen, *Nature.*, **391**, 667, 1998.
2. H. Raether, “*Surface Plasmons on Smooth and Rough Surfaces and on Gratings*”.  
Berlin, Springer-Verlag, 1988.
3. S. T. Wu, U. Efron, and L. V. Hess, *Appl. Phys. Lett.* **44**, 1033, 1984.
4. I. C. Khoo, R. R. Michael, and G. M. Finn, *Appl. Phys. Lett.* **52**, 2108, 1988.
5. G. Mourou, *Appl. Phys. Lett.*, **38**, 470, 1981.
6. D. H. Auston, *Appl. Phys. Lett.*, **45**, 284, 1984.
7. Q. Wu, *Appl. Phys. Lett.*, **68**, 1604, 1996.
8. G. Gruner, “*Millimeter and submillimeter wave spectroscopy of solids*,” Berlin,  
Springer-Verlag, 1998.
9. P. K. Benicewicz, *J. Opt. Soc. Am. B*, **11**, 2533, 1994.
10. Martin van Exter, *Opt. Lett.* **14**, 1128, 1989.
11. F. Reinitzer, *Monatsch Chem.*, **9**, 421, 1888.
12. O. Lehmann, *Z. Physik. Cham.*, **4**, 462, 1989.
13. P. G. de Gennes and J. Prost, “*The Physics of Liquid Crystals*”, **2nd ed.** (Oxford,  
New York, 1983).
14. P. Yeh and C. Gu, “*Optics of Liquid Crystal Displays*”, **1<sup>st</sup> ed.** (John Wiley & Sons,  
New York, 1999).





15. Eugene Hecht, “*Optics*”, **3rd ed.** (Addison Wesley Longman, New York, 1998).
16. David K. Cheng., “*Field and wave electromagnetics*”, **2nd ed.** New York, Addison-Wesley, 1989.
17. William L. Barnes, *Nature.*, **424**, 824, 2003.
18. Hua Cao, *Opt. Exp.*, **12**, 1004, 2004.



## Figures:

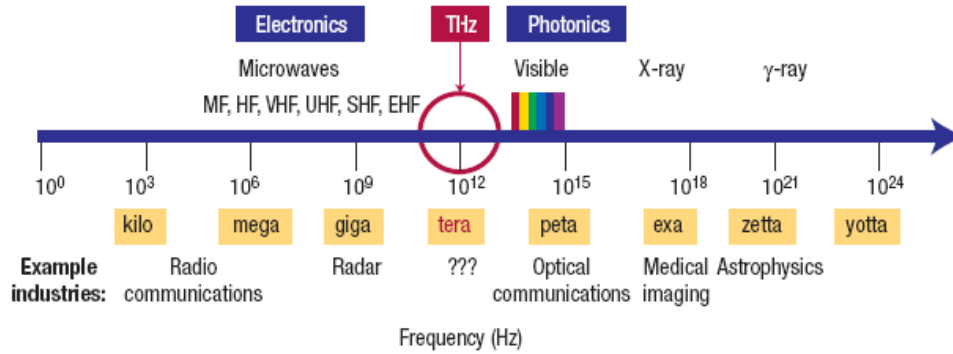


Figure 1.1.1 Electromagnetic frequency spectrum. The THz gap lies between photonics and electronics regimes, this gap is indicated as a red arrow.

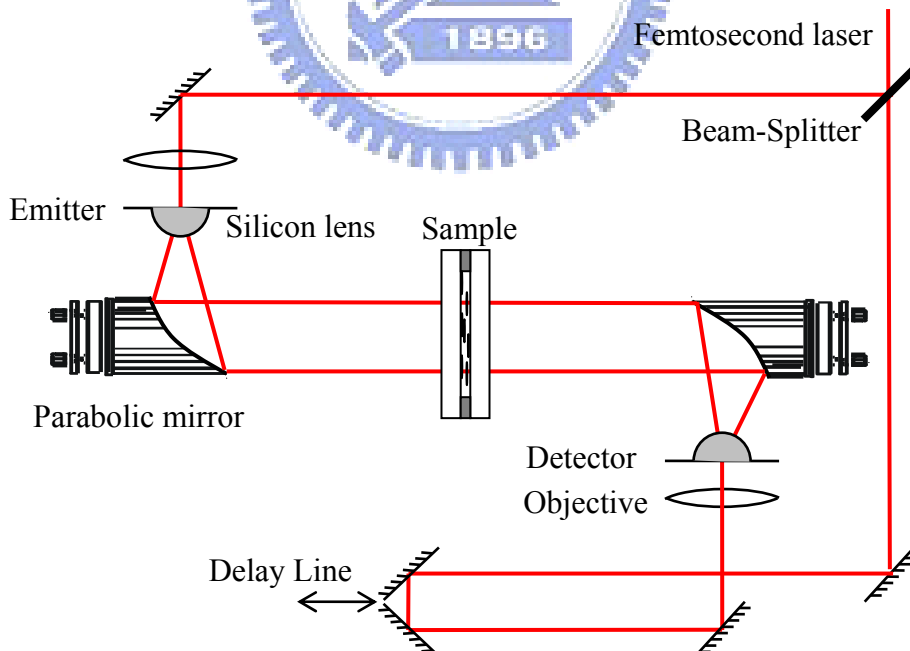


Figure 1.2.1 Traditional setup of the antenna-based transmission-type THz TDS system. The spot size of THz is about 2.0 cm and the step of delay stage is 10  $\mu$ m.

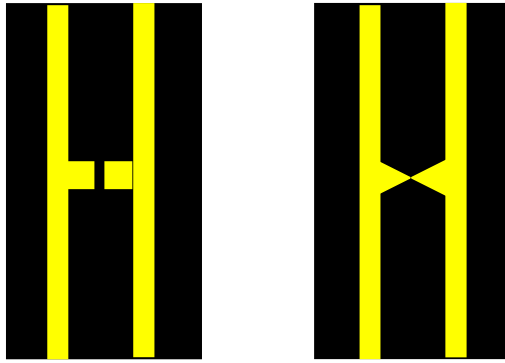


Figure 1.2.2 LTG-GaAs PC dipole (left) and bow-tie (right) antenna. The gap is  $5\mu\text{m}$ .

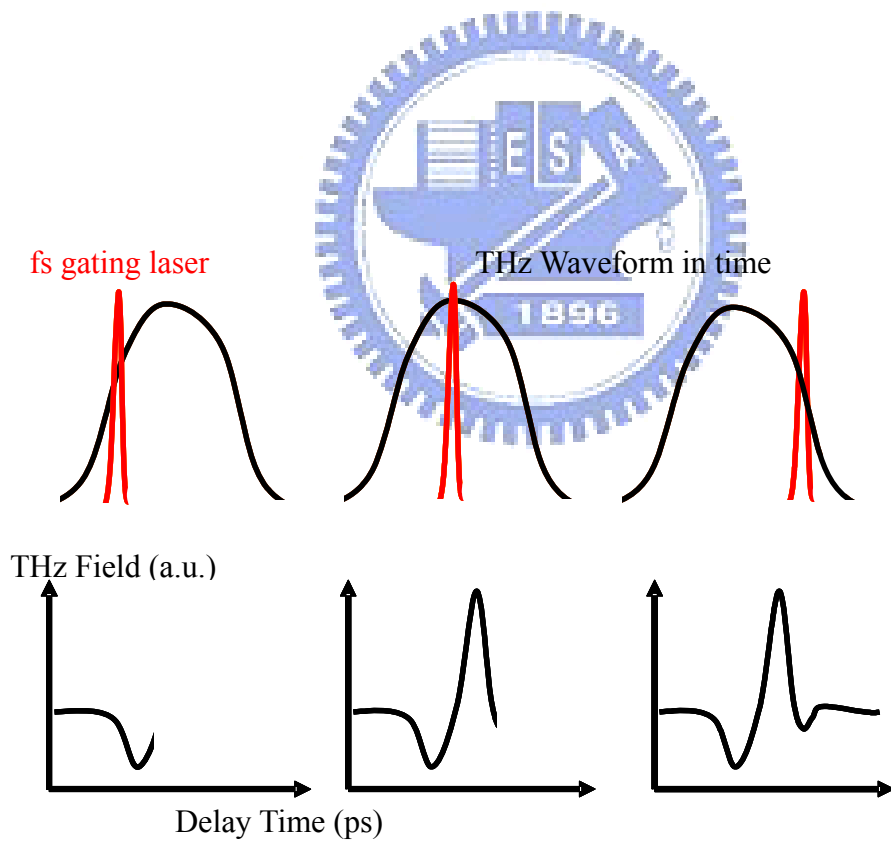


Figure 1.2.3 The photoconductive detector acts as a sampling gate that measures the electric field  $E(t)$  of THz signal within the sampling time  $\tau$ . The entire waveform of THz waveform in time domain can be mapped out.

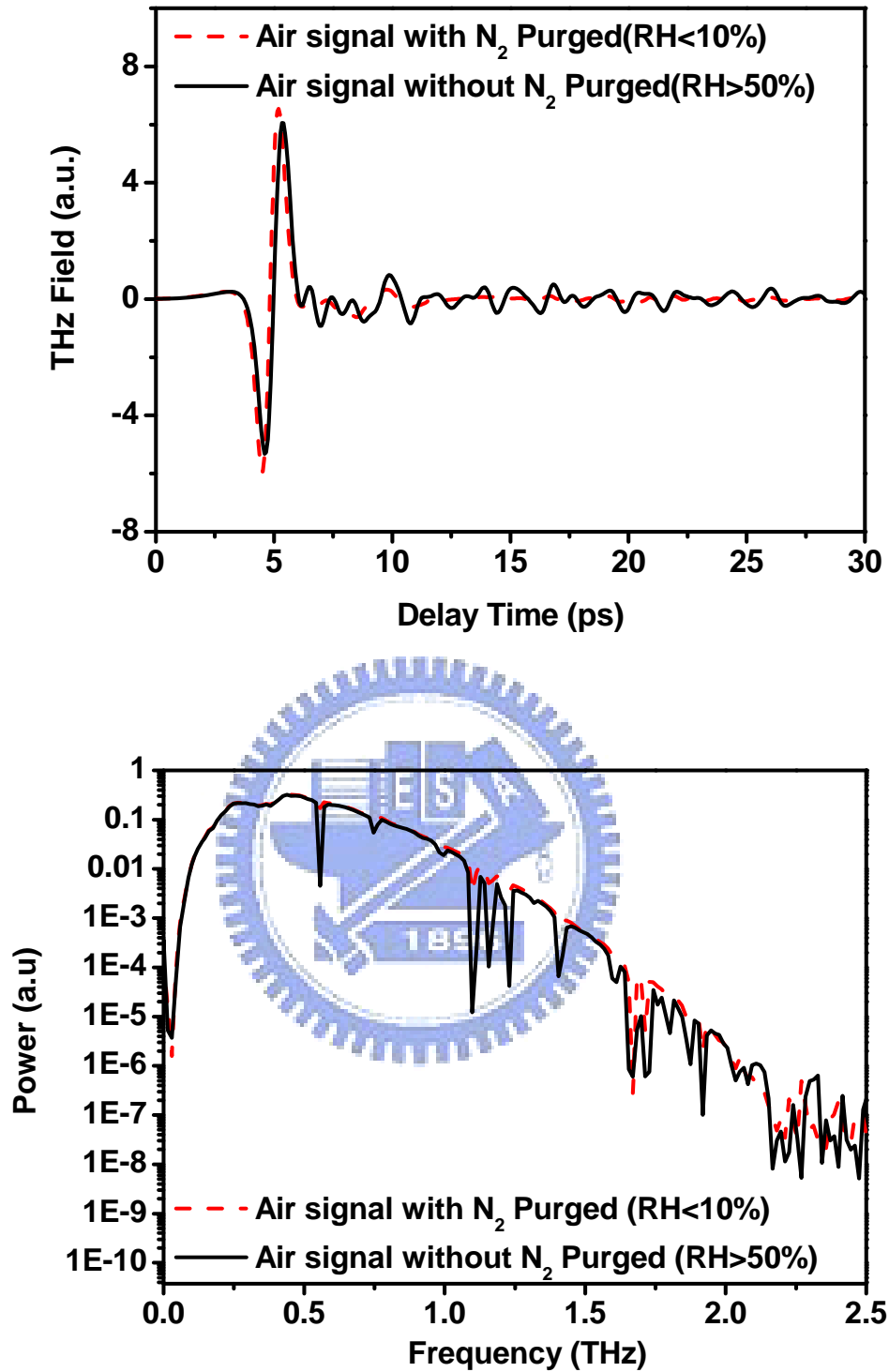


Figure 1.2.4 (a) The results of the THz signals in time domain passing through the air; (b) the power spectrum of transmitted THz signals in frequency domain. The red dash and black solid line represent the air with and without  $N_2$  purge, respectively.

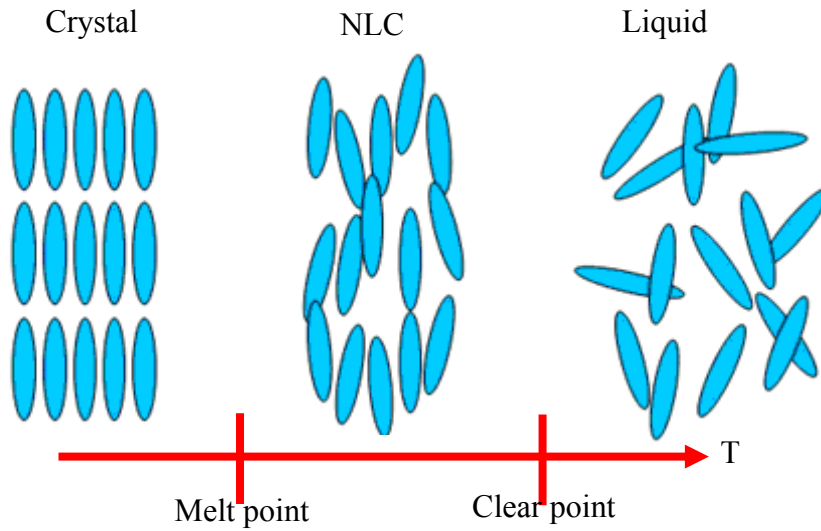


Figure 1.3.1 Schematic illustration of thermotropic NLCs with temperature-dependent phase transition.

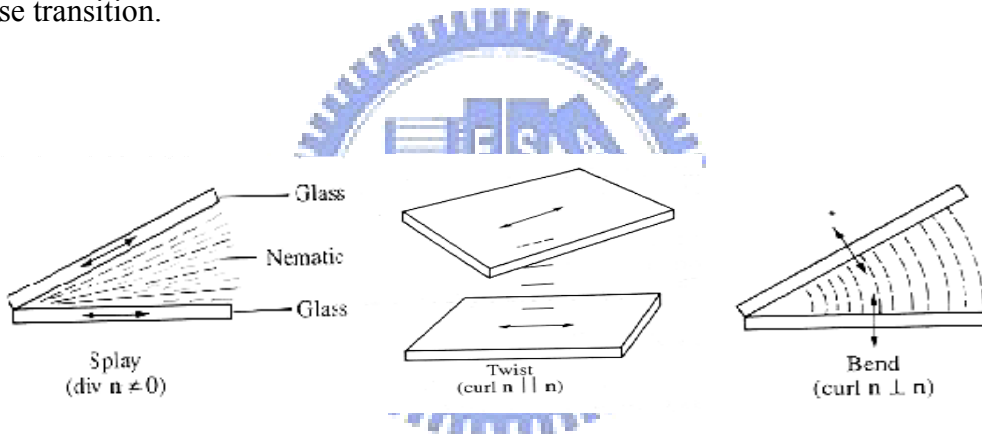


Figure 1.3.2. Three different types of deformation occurring in nematics cell.

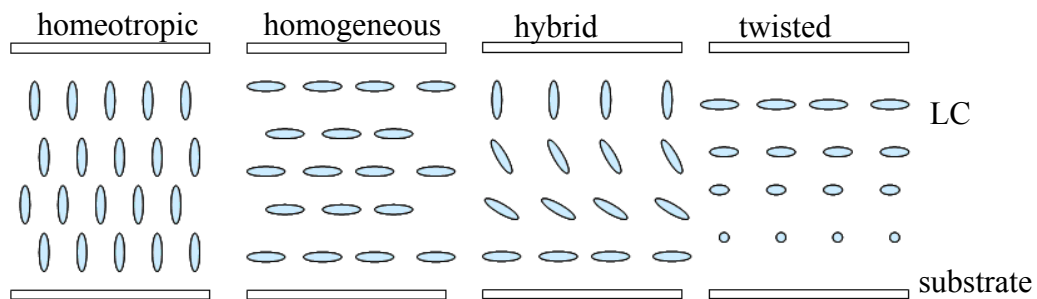


Figure 1.3.3 Different combinations of various aligned substrates.

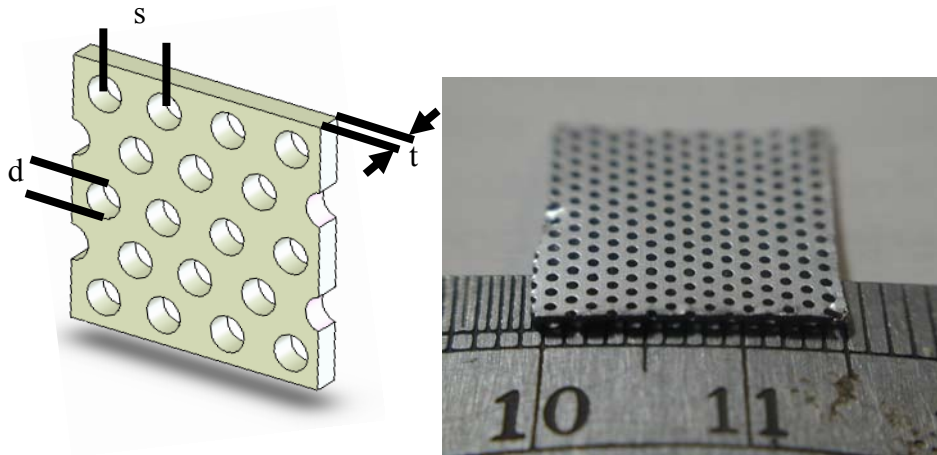


Figure 1.4.1 Schematic diagram (left) and real picture (right) of a 2D-MHA. The thickness of 2D-MHA is  $500\ \mu\text{m}$ . The  $s$  and  $d$  are  $0.99$  and  $0.56$  mm, respectively.

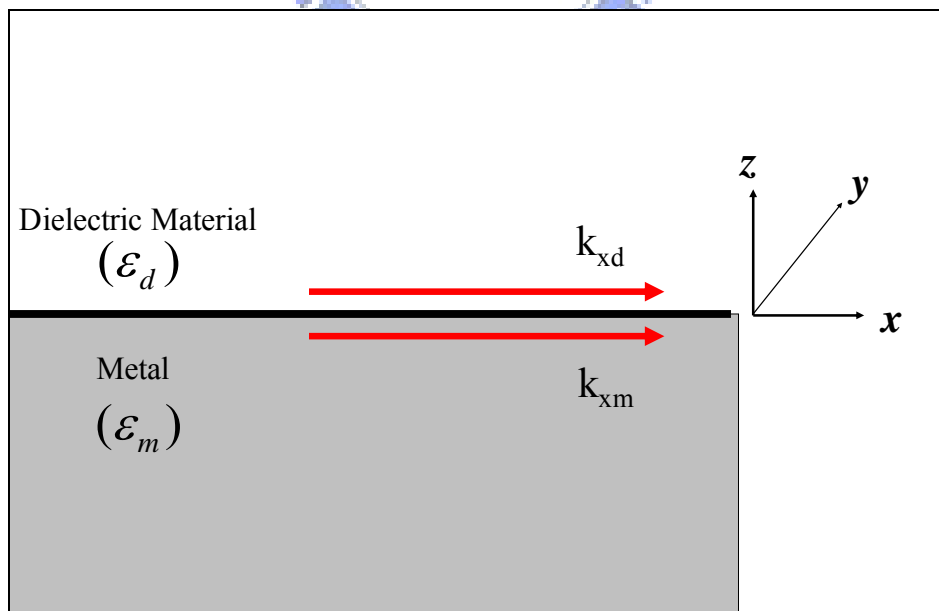


Figure 1.4.2 Polarization of electromagnetic wave propagating along the x-direction.

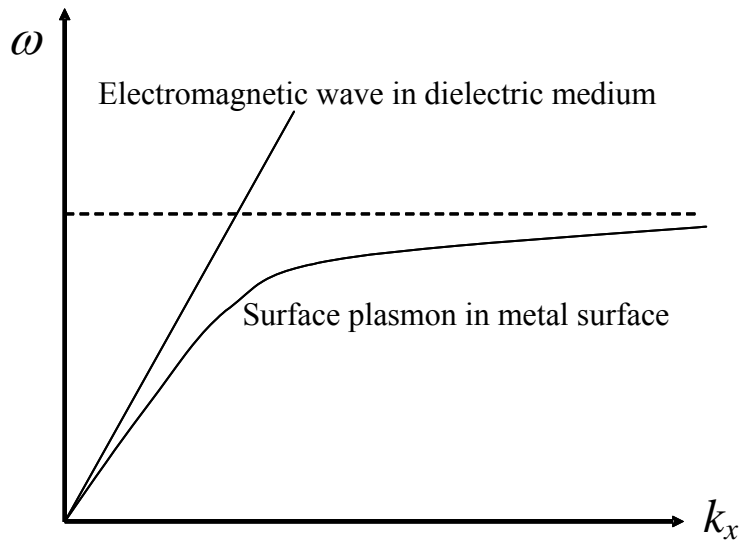


Figure 1.4.3 Dispersion relation of the electromagnetic wave in dielectric medium and the surface plasmon in metal surface.

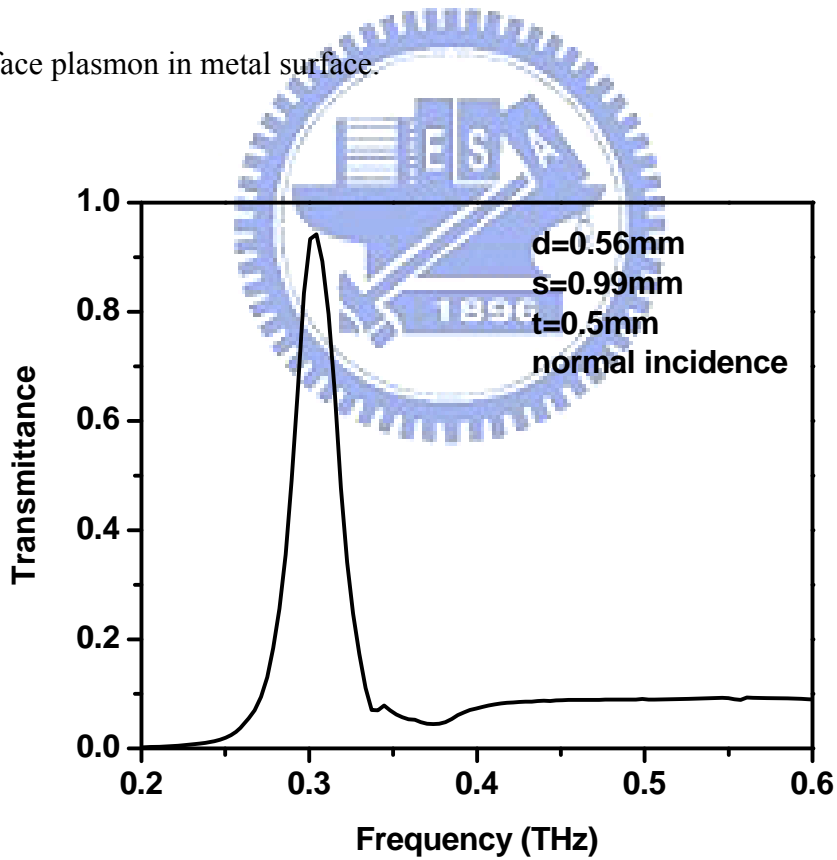


Figure 1.4.4 Experimental data of transmittance of a 2D triangular aluminum hole array in THz frequency range. The resonant peak is around 0.3 THz.

# Chapter 2 Optical Constants and Birefringence of Nematic Liquid Crystals PCH-5 and E7 in Terahertz Frequency Range

## 2.1 Nematic Liquid Crystal PCH-5 and E7

The molecules in the nematic phase are oriented on average along a particular direction by the boundary. Consequently, there is a macroscopic anisotropy in many material properties, such as dielectric constants, permeability and refractive index. It has great potential to apply this phase in many LC devices, because the anisotropic properties can manipulate the polarization or transmission of light. The molecular formula and weight of the nematic liquid crystal PCH-5 [4-(trans-4'-pentylcyclohexyl)-benzotrile] (Aldrich) are  $\text{CH}_3(\text{CH}_2)_4\text{C}_6\text{H}_{10}\text{C}_6\text{H}_4\text{CN}$  and 255.40, respectively. And E7 (Merck) is a mixture which is composed of 47% K15 (4-pentyl-4'-cyanobiphenyl), 25% K21 (4-heptyl-4'-cyanobiphenyl), 18% M24 (4-octyloxy-4'-cyanobiphenyl) and 10% T15 (4-pentyl-4'-cyanoterphenyl) [1]. We will probe the frequency-dependent optical constant and birefringence of PCH-5 and E7 in THz frequency range.

## 2.2 Nematic Liquid Crystal in THz Wave

In the far-infrared (sub-millimeter wave) or THz frequency range, the absorption spectra (6-200  $\text{cm}^{-1}$ ) of typical liquid crystal compounds



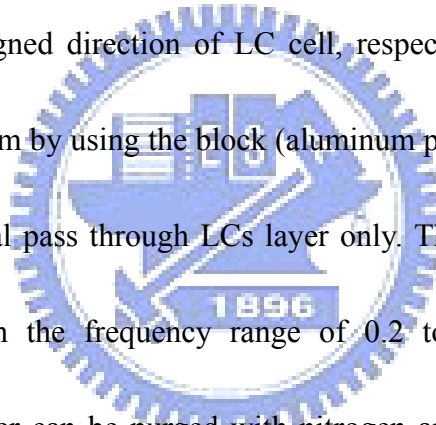
N-(p-methoxybenzylidene)-p-n- butylaniline (MBBA) and 4,4'-azoxydianisole (PAA) were studied over two decades ago [2, 3]. More recently, the refractive indices and transmission losses for some nematic LCs, including 4'-n-pentyl-4-cyanobiphenyl (5CB), have been measured by Nose *et al.* [4] at three discrete wavelengths (118, 215, and 435  $\mu\text{m}$ ): The refractive indices of 5CB for ordinary ( $n_o$ ) and extraordinary rays ( $n_e$ ) in the submillimeter wave region were found to be slightly larger than those in the visible range. Employing THz time-domain spectroscopy (THz-TDS) [5], we have shown that the THz birefringence of 5CB is  $0.20 \pm 0.02$  [6]. The imaginary part of refractive index of 5CB is less than 0.02 and without sharp absorption features in the frequency range of 0.2 – 1.0 THz. The extraordinary and ordinary indices of refraction at 25°C are around 1.77 and 1.58, respectively.

## 2.3 Experimental Methods

Two types of cells, a reference cell and a homogeneously aligned liquid crystal cell, were prepared in this work. These are shown schematically in Fig. 2.1. The reference cell was constructed by two fused silica windows coated with polyimide and with nominal thickness of 3.0 mm each and in contact to each other. For the liquid crystal cell, a nematic liquid crystal layer (PCH-5, Aldrich) was sandwiched between two fused silica windows as substrates (the thickness of fused silica is 3.32 mm). Thickness of the liquid crystal layer was controlled with Teflon spacers and measured

by subtracting the substrates thicknesses from the total cell thickness. The LC layer thickness in this work is  $617 \pm 3 \mu\text{m}$ . Homogeneous alignment was achieved by coating polyimide on inner surfaces of the substrates followed by mechanical rubbing [7]. The substrates were chosen such that the total thicknesses of the two substrates for these two cells are equal with an accuracy of  $2 \mu\text{m}$ .

An antenna-based THz-TDS system with a collimated beam at the sample position [8] had been used. The THz fields of e-ray and o-ray are parallel and perpendicular to the aligned direction of LC cell, respectively. We usually confine spot size of THz as 0.8 cm by using the block (aluminum plate with a circular hole) to make sure all THz signal pass through LCs layer only. There are several absorption lines of water vapor in the frequency range of 0.2 to 1.5 THz [9]. Our THz time-domain spectrometer can be purged with nitrogen and maintained at a relative humidity of  $3.5 \pm 0.5\%$ .



## 2.4 Determination of Optical Constants

We assume that the THz signal is a plane wave passing through the cell at normal incidence. The electric field of the THz wave transmitted through the reference cell at an angular frequency  $\omega$ , can then be written as

$$E_{ref}(\omega) = E_0(\omega) \cdot \eta(\omega) \cdot P_{air}(\omega, d), \quad (2.1)$$

where  $E_0(\omega)$  is the electric field of the incident THz wave. The parameter  $\eta(\omega)$  takes into account the Fabry-Perot effect due to the Fresnel reflection of the THz wave at the quartz-air interfaces and its propagation in fused silica. The propagation coefficient in air over a distance  $d$  is denoted by  $P_{air}(\omega, d) = \exp[(-i\tilde{n}_{air}\omega d)/c]$ , where  $\tilde{n}_{air}$  is the complex refractive index of air and the value of  $1+0i$  is assumed in this work. The length  $d$  is chosen to be the same as that of the LC layer (see Fig. 2.1). Similarly, the electric field of the THz wave transmitted through the LC cell can be written as

$$E_{LC}(\omega) = E_0(\omega) \cdot \eta(\omega) \cdot T_{q-LC}(\omega) \cdot P_{LC}(\omega, d) \cdot T_{LC-q}(\omega) \cdot FP_{LC}(\omega, d), \quad (2.2)$$

where  $T_{q-LC}(\omega) = (2 \cdot \tilde{n}_q) / (\tilde{n}_q + \tilde{n}_{LC})$  and  $T_{LC-q}(\omega) = (2 \cdot \tilde{n}_{LC}) / (\tilde{n}_{LC} + \tilde{n}_q)$  are the transmission coefficients of the quartz-LC and LC-quartz interfaces, respectively;  $P_{LC}(\omega, d) = \exp[(-i\tilde{n}_{LC}\omega d)/c]$  and  $FP_{LC}(\omega, d)$  are propagation and Fabry-Perot coefficients in the LC layer with a thickness of  $d$ . The coefficient,  $\eta(\omega)$  for the LC cell is the same as that for the reference cell because of the thicknesses of the fused silica windows used are the same (tolerance  $< 2\mu\text{m}$ ). The complex transmittance  $T(\omega)$  of the LC layer can then be obtained by dividing  $E_{LC}(\omega)$  by  $E_{ref}(\omega)$ :

$$T(\omega) = \frac{4 \cdot \tilde{n}_{LC} \cdot \tilde{n}_q}{(\tilde{n}_{LC} + \tilde{n}_q)^2} \cdot \exp\left[-i(\tilde{n}_{LC} - \tilde{n}_{air}) \frac{\omega \cdot d}{c}\right] \cdot FP_{LC}(\omega, d), \quad (2.3)$$

where  $\tilde{n}_q$  is the complex refractive index of fused silica (The measured frequency-dependent index of the 3-mm-thick fused silica substrates at room temperature is  $1.951+0i$  without dispersion and absorption in the range of 0.2-1.5 THz, in good agreement with data from the literature [10]) and  $\tilde{n}_{LC}$  is either the ordinary index ( $\tilde{n}_o = n_o - i\kappa_o$ ) or extraordinary index ( $\tilde{n}_e = n_e - i\kappa_e$ ) of the LC layer.

For optically thick samples, the echoes of THz waves from the multiple reflections of the sample are temporally well separated from the main signal. These can be easily removed without affecting accuracies of the measurements. Thus we can set  $FP_{LC}(\omega, d) = 1$  in Eq. 2.3 [11]. On the left of Eq. (2.3),  $T(\omega)$  is experimentally measured complex transmission coefficients. On the right of Eq. (2.3), only  $\tilde{n}_{LC} = n_{LC} - i\kappa_{LC}$  is unknown parameter which can be easily calculated with a given trial set of  $(n_{LC}, \kappa_{LC})$ . Approximate values of  $n_{LC}$  and  $\kappa_{LC}$  were obtained by setting  $FP(\omega) = 1$  in Eq. (2.3) and then this set was used as the initial trial values. After equalizing Eq. (2.3), the optical constants  $n_{LC}$  and  $\kappa_{LC}$  are determined for any angular frequency,  $\omega$ .

## 2.5 Results and Discussions of PCH-5

### 2.5.1 Complex Optical Constants

The amplitude and the phase spectra of the THz wave passing through the LC cell and reference cell are obtained by applying a fast Fourier transform (FFT) to the

time-domain waveforms. The optical constants of the LC are then determined using the procedure described in the previous section.

The real part and imaginary part of the optical constants of PCH-5 at 30 °C are shown as a function of frequency in Fig. 2.2. The nematic temperature range of PCH-5 is from 30 °C to 55 °C [1]. The filled circles and the open circles are the extraordinary and ordinary indices,  $n_e$ ,  $n_o$ , respectively. The real parts of the indices show clear anisotropy, with  $n_e = 1.55$  and  $n_o = 1.51$ , giving rise to a birefringence of 0.04. We note that birefringence of PCH-5 is 0.12 in the visible [12]. The imaginary part of the refractive index of PCH-5 is smaller than 0.04 in the frequency range from 0.2 THz to 1.0 THz. It does not exhibit appreciable anisotropy.

## 2.5.2 Temperature Dependence

The temperature dependence of the real indices of PCH-5 at frequencies of 0.3, 0.5, 0.7, and 0.8 THz are shown in Fig. 2.3. The filled and open circles are experimental data for  $n_e$  and  $n_o$  respectively. Following Brugioni *et al.* [13], we fit the temperature dependence of the real part of the refractive indices with

$$n = A \times (B - T_R)^C, \quad (2.4)$$

where  $n$  is the refractive index,  $T_R$  is the reduced temperature defined as the difference between measured sample temperature and measured clearing point ( $T - T_c$ ). In our work,  $T_c$  is 54°C. The fitting parameters  $A$ ,  $B$  and  $C$  thus obtained are shown in Table

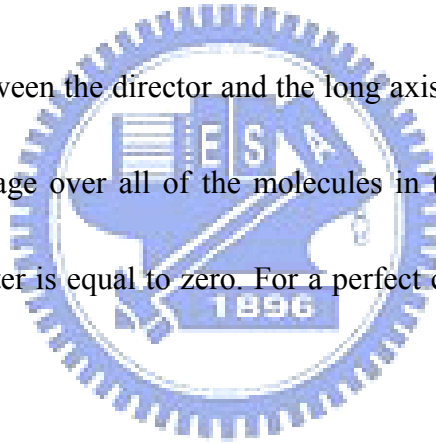
2.1. The fitting curves are also shown in Fig. 2.3 as the solid line with the measured data. Above the transition temperature, i.e., in isotropic phase, the experimental points are shown in Fig. 2.3 with stars. Below the transition temperature, the dash lines show the average indices,  $(2n_o + n_e)/3$ , from the fitting results.

### 2.5.3 Birefringence and Order Parameter

To quantify just how much order is present in a LC, an order parameter,  $S$  is defined as

$$S = \langle 3 \cos^2 \theta - 1 \rangle / 2, \quad (2.5)$$

where  $\theta$  is the angle between the director and the long axis of each LC molecule. The brackets denote an average over all of the molecules in the sample. In an isotropic liquid, the order parameter is equal to zero. For a perfect crystal, the order parameter evaluates to one.



The temperature-dependent birefringence of PCH-5 at the frequencies of 0.4 THz is plotted in Fig. 2.4, in which the solid curves are the fitting results by using

$$\Delta n(T) = D \times \left(1 - \frac{E \cdot T}{T_C}\right)^F, \quad (2.6)$$

where  $D$ ,  $E$  and  $F$  are fitting parameters. The order parameter of PCH-5 can be extracted from the fitting parameters as

$$S = \left(1 - \frac{E \cdot T}{T_C}\right)^F. \quad (2.7)$$

We find that  $E = 0.981 \pm 0.01$  and  $F = 0.148 \pm 0.02$ .

We did not chemically analyze the purity of the PCH-5 (Aldrich) we used. The clearing point of LCs, however, correlates directly to its purity. It was found to be 54 °C in our work. We can, however, conclude that there is no resonant absorption in this frequency range as the measured real indices are spectrally flat and smooth. Results from this sample also suggest that there is no sharp resonance in this frequency range and the imaginary part of refractive index of PCH-5 in the nematic phase is less than 0.04 in the frequency range of 0.2-1.0 THz.

## **2.6 Complex Optical Constants of E7 in THz**

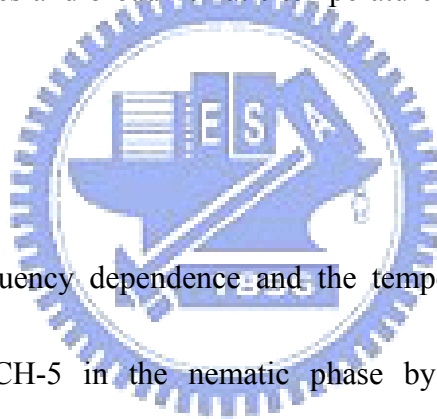
### **Frequency Range**

We also measured the complex refractive index of E7, which exhibits birefringence larger than that of PCH-5. Further, the nematic range of E7 (-10°C ~ 61°C) is significantly larger than that of 5CB (24°C ~ 35°C), making it more convenient for practical applications. For THz applications, the LC devices usually have thicker thickness than that in the visible because of the long wavelength of THz band. It is expected that the thickness of the LC layer, the alignment quality of LC cell and the purity of LC will all affect the accuracy of the extracted optical constants. In principle, the thicker the layer is, the more accurate the results are. However, the E7 layer thickness is 8.087 mm and aligned by the magnetic field of 2.5 Tesla. The

optical constants of E7 for both the o-ray and e-ray are determined using the method and procedure described in our previous section. In Figure 2.5, the THz-band extraordinary and ordinary refractive indices of E7 are shown. Clearly, E7 exhibits a positive birefringence ( $n_e > n_o$ ), which is consistent with that in the visible range [14]. There is no sharp resonance in the 0.2-0.9 THz range. The birefringence of E7 is 0.13 for the same frequency range (see Fig. 2.5 (b)). The corresponding imaginary indices of E7 are relatively small ( $< 0.02$ , see Fig. 2.5 (c)). Thus E7 exhibits high birefringence, small losses and broad nematic temperature range, which are attractive for applications.

## 2.7 Conclusions

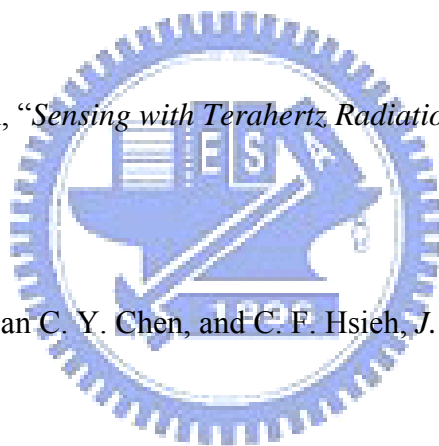
We report the frequency dependence and the temperature dependence of the optical constants of PCH-5 in the nematic phase by using THz time-domain spectroscopy. And we also measure the frequency dependence of the optical constants of E7 in nematic phases. We found that the imaginary part of refractive index of PCH-5 and E7 are relatively small and without sharp absorption features in the frequency range of 0.2 – 1.0 THz. By using thick E7 layer, we can obtain the  $\kappa_o$  is larger than  $\kappa_e$  in THz frequency range. Further studies are in progress to probe the origin of the significantly different THz properties of these well-known LCs and its applications.



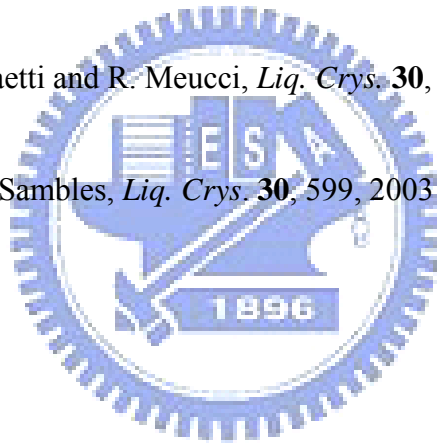


## References

1. Pochi Yeh, *Optics of LC Displays*, John Wiley & Sons, Inc, 1999.
2. Myron Evans, Mansel Davies and Ian Larkin, *J. Chem. Soc., Faraday Trans.* **69**, 1011, 1973.
3. Bernard J. Bulkin and Wai Bong Lok, *J. Phys. Chem.* **77**, 326, 1973.
4. T. Nose, S. Sato, K. Mizuno, J. Bae and T. Nozokido, *Appl. Opt.* **36**, 6383, 1997.
5. Daniel Mittleman, “*Sensing with Terahertz Radiation*”, 1<sup>st</sup> ed. (Springer, New York, 2002).
6. R. P. Pan, C. L. Pan, C. Y. Chen, and C. F. Hsieh, *J. Appl. Phys.*, **103**, 093523, 2008.
7. M. Nakamura, *J. Appl. Phys.* **52**, 4561, 1981.
8. C. L. Pan, C. F. Hsieh, R. P. Pan, M. Tanaka, F. Miyamaru, M. Tani, and M. Hangyo, *Opt. Exp.* **13**, 3921, 30, 2005.
9. Martin van Exter, Ch. Fattinger, and D. Grischkowsky, *Opt. Lett.* **14**, 1128, 1989.



10. D. Grischkowsky, S. R. Keiding, M. van Exter, and C. Fattinger, *J. Opt. Soc. Am. B* **7**, 2006, 1990.
11. Eugene Hecht, "Optics", 3rd ed. (Addison Wesley Longman, New York, 1998), Chap. 4.
12. Pochi Yeh, *Optics of LC Displays*, John Wiley & Sons, Inc, 1999.
13. Birendra Bahadur, *liquid crystals applications and uses vol.1*, world scientific, Singapore, 1995.
14. S. Brugioni, S. Faetti and R. Meucci, *Liq. Crys.* **30**, 927, 2003.
15. F. Yang and J.R. Sambles, *Liq. Crys.* **30**, 599, 2003



## Table

Table 2.1 The fitting parameters of Eq. (2.4) for frequencies from 0.220 to 0.938 THz.

(Ao, Bo, Co) and (Ae, Be, Ce) are for no and ne, respectively.

frequency (THz)	Ao	Bo	Co	Ae	Be	Ce
0.220	1.536974	0.091224	-0.001464	1.536314	0.109918	0.003082
0.249	1.529620	0.020114	-0.001354	1.542728	0.142034	0.003319
0.283	1.520333	0.052674	-0.001834	1.540186	0.102467	0.030982
0.313	1.516310	0.029743	-0.001538	1.536628	0.107228	0.003462
0.347	1.522189	0.043110	-0.001752	1.538151	0.107614	0.003369
0.376	1.522280	0.042697	-0.001813	1.541148	0.074692	0.003170
0.405	1.518499	0.070253	-0.002002	1.539666	0.074792	0.003250
0.435	1.517076	0.037892	-0.001775	1.539426	0.073134	0.003354
0.469	1.516892	0.052528	-0.001860	1.540956	0.081881	0.003571
0.498	1.518674	0.069830	-0.002053	1.543390	0.069361	0.003421
0.532	1.520512	0.061170	-0.001965	1.545724	0.070161	0.003363
0.562	1.522489	0.070639	-0.002100	1.544499	0.109702	0.003534
0.596	1.520141	0.050545	-0.001965	1.543707	0.098567	0.003554
0.625	1.519309	0.048150	-0.002010	1.544307	0.075056	0.003484
0.654	1.519971	0.035887	-0.001872	1.545144	0.081350	0.003601
0.689	1.522051	0.071168	-0.002111	1.545682	0.011670	0.003801
0.718	1.521817	0.126605	-0.002331	1.545295	0.106932	0.003793
0.752	1.521307	0.023228	-0.001768	1.545996	0.080762	0.003546
0.781	1.521557	0.036723	-0.001931	1.546356	0.057002	0.003492
0.811	1.522027	0.022177	-0.001691	1.547168	0.057139	0.003608
0.845	1.524328	0.050783	-0.002140	1.548887	0.042575	0.003391
0.874	1.520577	0.002723	-0.001362	1.545746	0.073071	0.003804
0.908	1.522623	0.011956	-0.001631	1.544815	0.136560	0.004155
0.938	1.521162	0.013339	-0.001331	1.544524	0.090155	0.004188

## Figures:

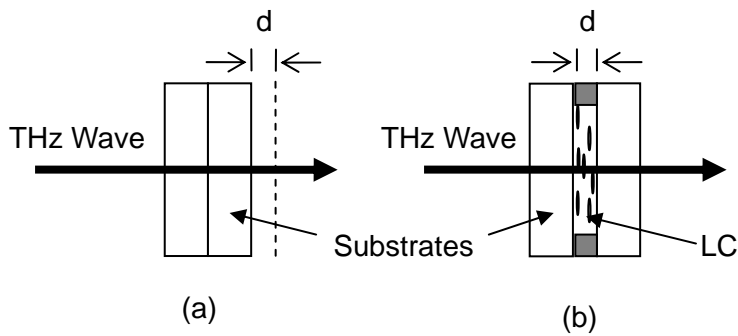


Figure 2.1 Sketches of (a) the reference cell and (b) the LC cell. The substrates are fused silica and the alignment of LC cell is homogeneous.

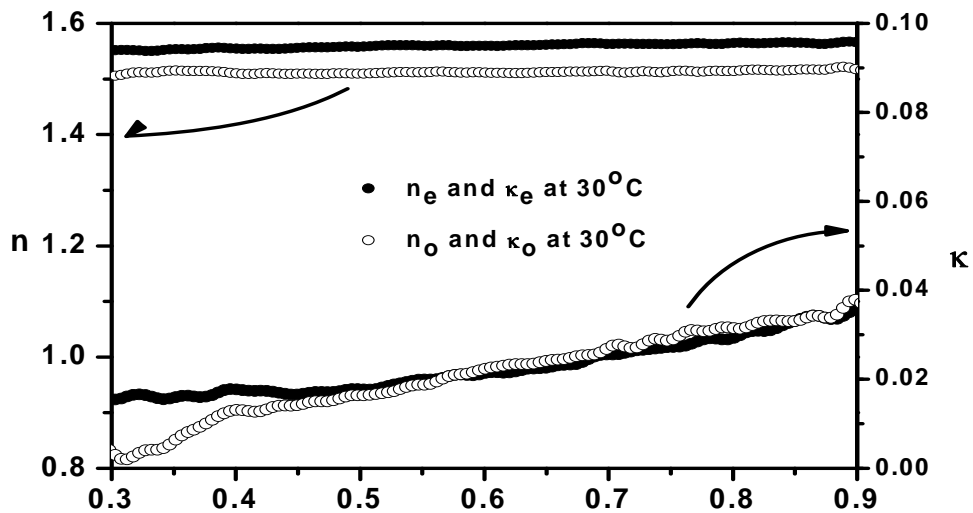


Figure 2.2 The optical constants of PCH-5,  $n$  and  $\kappa$ , are plotted as functions of frequency. The solid circles and the open circles are the extraordinary and ordinary indices at  $30^\circ\text{C}$ , respectively.

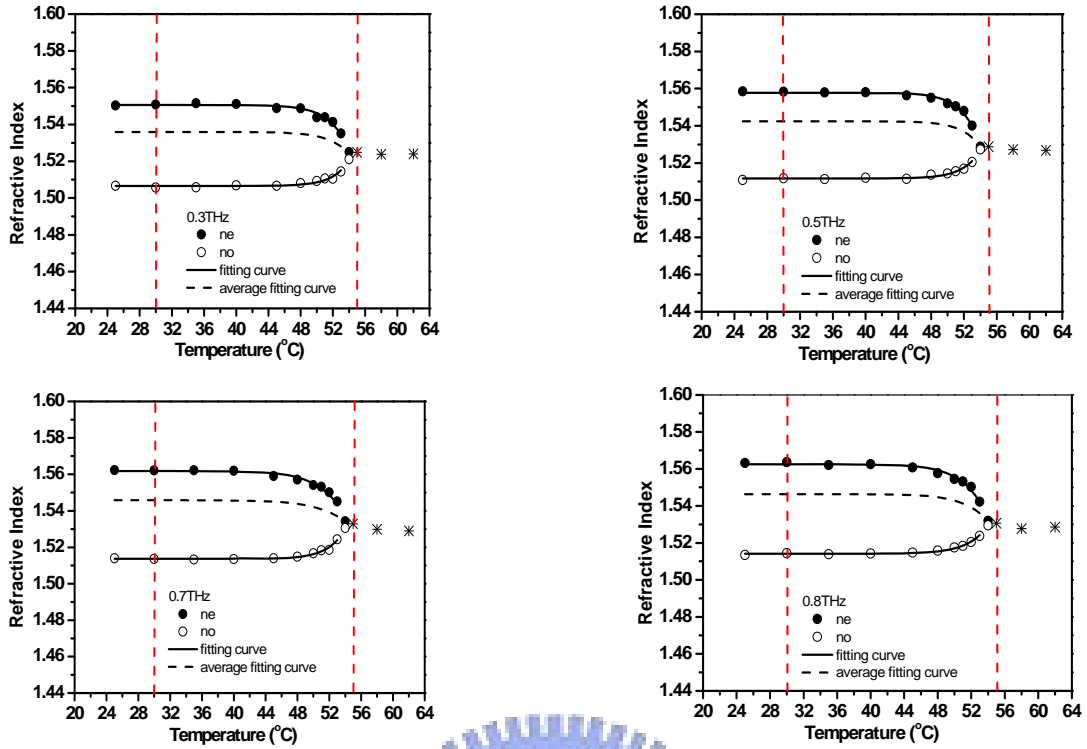


Figure 2.3 Extraordinary and ordinary refractive indices of PCH-5 are plotted as functions of temperature at frequencies of 0.3, 0.5, 0.7 and 0.8 THz. The solid and the open circles represent  $n_e$  and  $n_o$ , respectively. The dash lines are the average index,  $(2n_o + n_e)/3$  at temperatures below  $T_c$ .

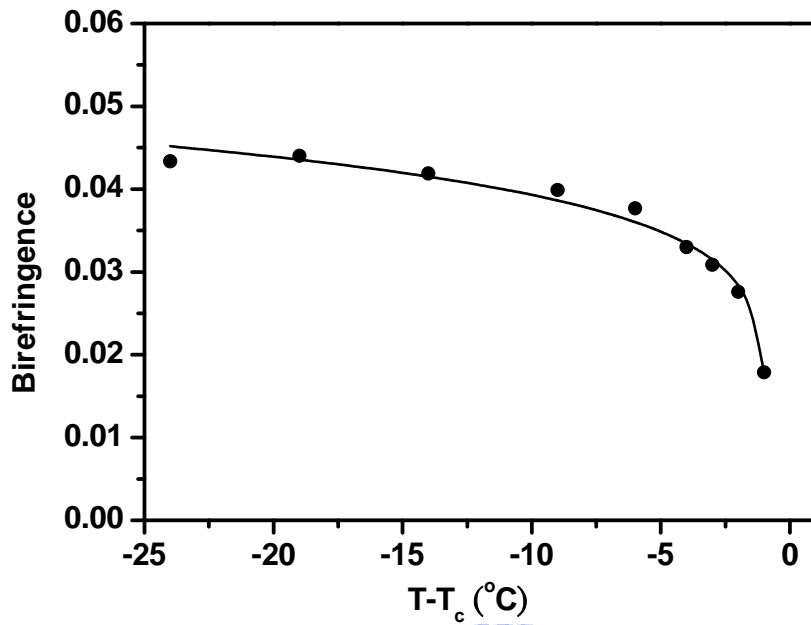
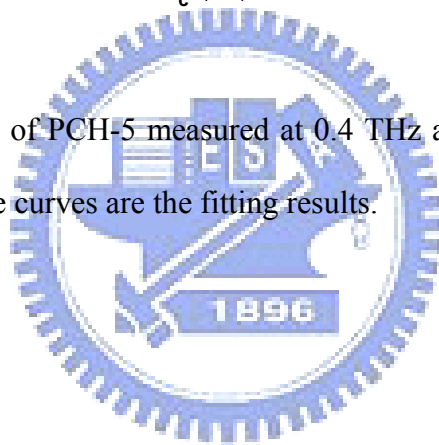


Figure 2.4 Birefringence of PCH-5 measured at 0.4 THz are plotted as a function of reduced temperature. The curves are the fitting results.



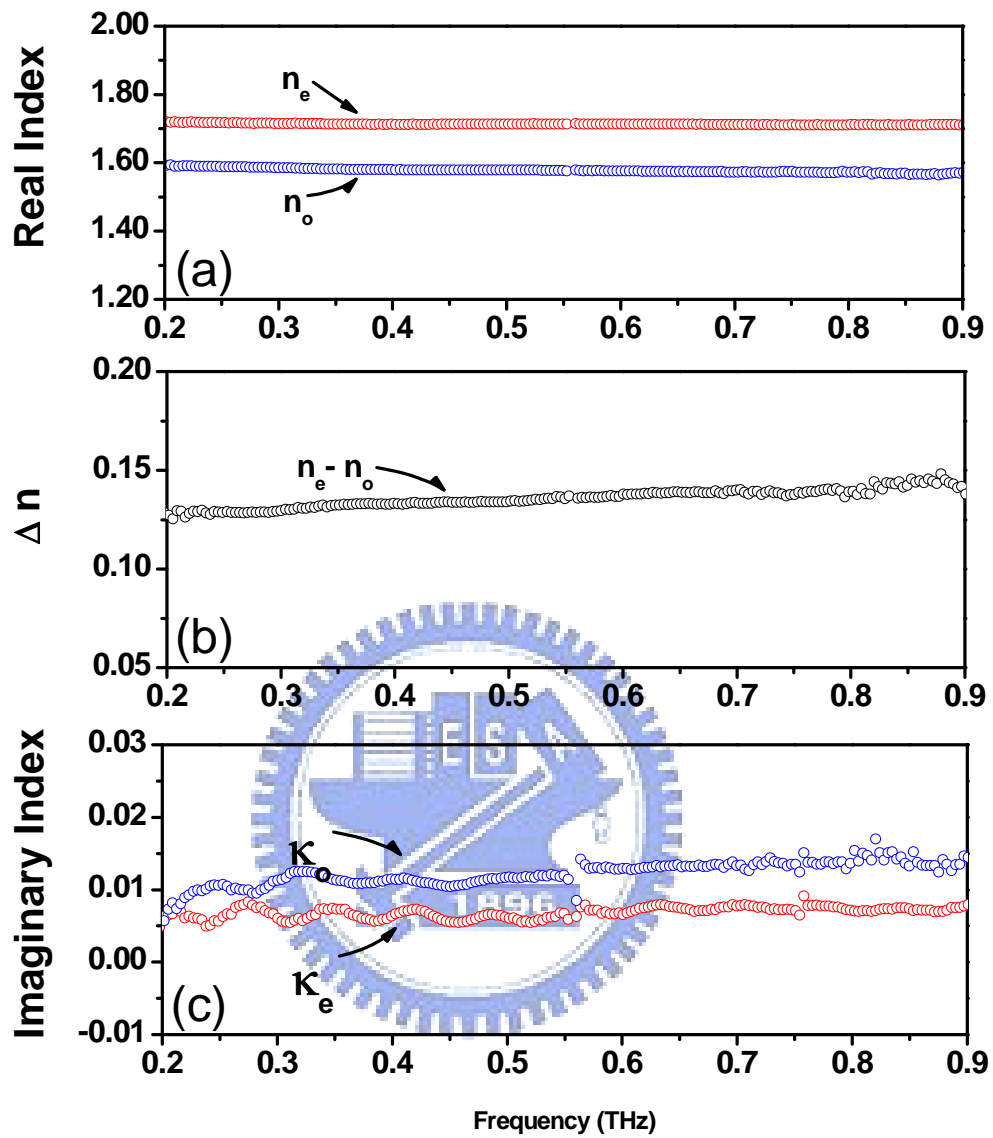


Figure 2.5 The room-temperature (a) extraordinary (red circles) and ordinary (blue circles) refractive indices, (b) birefringence, and (c) imaginary extraordinary (blue circles) and ordinary (red circles) refractive indices of E7 are shown as a function of frequency between 0.2 to 0.9 THz.

# Chapter 3 Tunable Room-Temperature Terahertz Phase Shifter Based on Controlled Birefringence in Nematic Liquid Crystals

## 3.1 Phase Shifters

The phase shifters are very common optical devices in a variety of fields, such as in wireless communications and radar systems. These devices can be approximately classified as mechanical and electronic controlled phase shifters, depending on the operation methods to change the phase of electromagnetic wave. We briefly introduce some common phase shifters used in micro wave and millimeter wave below.

1. Mechanical phase shifters are operated by means of mechanical tuning. We mechanically manipulate the effect length of the light path inside a waveguide for example. Comparing with the electronic phase shifters, mechanical ones are rugged, easy to fabricate, and less loss.
2. The working principle of Ferrite phase shifters is base on interacting the electromagnetic waves and the spinning electrons in a magnetized ferrite. The magnetic dipole moment of the spinning electron is tuned with applying dc magnetic field. Ferrite phase shifters have been achieved mostly in waveguide geometry.
3. The semiconductor phase shifters are composed of semiconductor junctions. These act as electronic switches such as the p-i-n diode, GaAs FET, and the Schottky diodes.
4. The operation method of traveling-wave phase shifter is based on the interaction between an electron beam and electromagnetic signal on a traveling-wave structure. There are several practical limitations of this phase



shifter: a high noise figure and interdependent phase and gain, moreover, the devices are bulky and heavy.

However, these phase shifters are not exercised in the THz frequency. For THz phase shifting application, several groups have demonstrated tunable phase shifters based on optically or electrically controlled carrier concentration in quantum well structures [1-3]. For example, Libon *et al* [1] recently demonstrated a tunable THz phase shifter based on optically induced change of the carrier concentration in GaAs multiple quantum well (MQW) structures. Control of the electron occupation and hence absorption of the THz radiation in MQW by an applied electric field has been used by Kersting *et al* [2] to shift the phase of the THz wave. Owing to their Lorentz-type dielectric function, parabolic quantum well structure has been used to enable efficient phase modulation of electromagnetic waves up to 4 THz. Gated two-dimensional electron gas in semiconductor nanostructures is proposed to change the phase of the THz carrier wave by up to 0.5 radians [3]. Both of these quantum-well-based THz phase shifters, nevertheless, have limited range of tunability (have not yet demonstrated  $2\pi$  phase shift) and in general need to be operated at cryogenic temperatures far below room temperature [1, 2].

In chapter 2, we have recently determined the complex index of refraction of a NLC 4'-n-pentyl-4-cyanobiphenyl (5CB), E7 and PCH-5 for both the o-ray and e-ray at room temperature by THz time-domain spectroscopic (THz-TDS) technique [4]. Significantly, the nematic 5CB exhibits relatively large birefringence ( $\sim 0.2$ ) and small extinction coefficient ( $\sim 0.01$ ) at frequencies around 1.0 THz. This indicates that 5CB in the nematic phase is potentially useful for tunable device applications in the THz frequency range. The nematic range of E7 ( $-10^{\circ}\text{C} \sim 61^{\circ}\text{C}$ ) is noteworthy larger

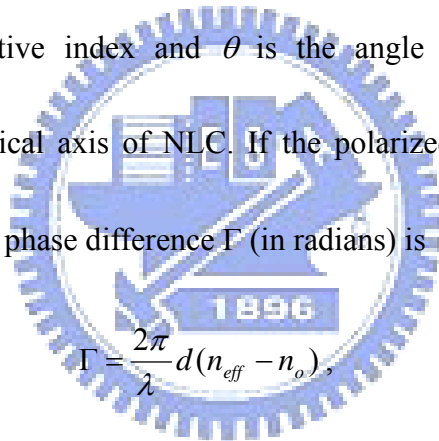
than that of 5CB (24°C ~ 35°C), making it more convenient and attractive for practical applications.

### 3.2 Phase Shifter Based Nematic Liquid Crystals

The refractive indices of NLC associated with ordinary-ray and extraordinary-ray are given by

$$\begin{aligned} \text{ordinary - ray:} \quad n &= n_o \\ \text{extraordinary - ray:} \quad \frac{1}{n_{eff}(\theta)^2} &= \frac{\cos^2 \theta}{n_o^2} + \frac{\sin^2 \theta}{n_e^2}, \end{aligned} \quad (3.1.1)$$

where  $n_{eff}$  is the effective index and  $\theta$  is the angle between the direction of propagation and the optical axis of NLC. If the polarized electromagnetic wave is incident to NLC cell, the phase difference  $\Gamma$  (in radians) is



$$\Gamma = \frac{2\pi}{\lambda} d(n_{eff} - n_o), \quad (3.1.2)$$

where  $\lambda$  is the wavelength of wave and  $d$  is the length of NLC sample. Once the director of the NLC is changed, the effective index related to the polarized electromagnetic waves is also changed. So the phase of electromagnetic wave can be controlled by manipulating the director of NLC. If the orientation of the LC molecules is not uniform, the effective birefringence is the function of the position in the NLC layer.  $\Gamma$  is shown as follows

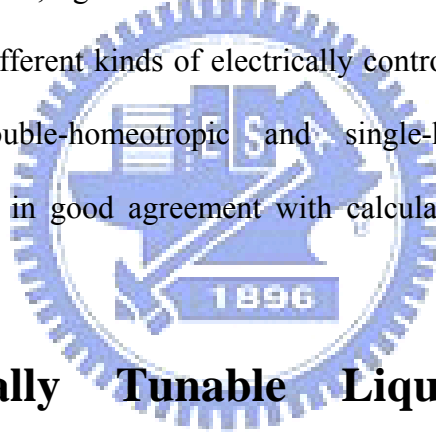
$$\text{phase difference} = \int_0^d \frac{2\pi f}{c} \Delta n_{eff}(z) dz, \quad (3.1.3)$$

where  $n_{eff}$  is the change of effective birefringence,  $f$  is the frequency of the waves and  $c$  is the speed of light in vacuum.

By using the simple estimation  $\Delta\Gamma = \Delta n_{eff}kd$ , where  $k$  is the wave number of 1.00 THz, the thickness  $d$  of the NLCs layer required to achieve a  $2\pi$  phase shift at 1.00 THz would be 1.5 mm (birefringence of 5CB  $\sim 0.2$ ). This presents a problem, as alignment of the NLC becomes difficult with such thick cells. In order to quench the fluctuation of thick NLCs layer, we align the 5CB (Merck) molecules in a cell with nominal thickness of 1.5 mm by applying the magnetic field. We demonstrate a room temperature THz phase shifter based on magnetically controlled birefringence in NLCs. The magnetic field is used to change the orientation of NLC molecules and hence the effective index of refraction for THz waves. Consequently, we are able to achieve just a maximum phase shift of  $141^\circ$  at 1.03 THz [5]. Because the rotated permanent magnet is blocking the THz beam, the magnetic inclination angle (the angle between the easy direction and the magnetic field direction that is the same  $\theta$  in Eq. 3.1.1) is limited and smaller than  $55^\circ$ . The phase shifter needs larger thickness of 5CB layer about 3.0 mm in order to achieve a  $2\pi$  phase shift at 1.00 THz. This is overcome by employing a NLC cell with a sandwiched double structure (We use Teflon spacers for controlling the thickness of LC layers to 1.5 mm each is shown in Fig. 3.1.2 (b)). The new device is based on magnetically controlled birefringence in a sandwiched dual NLC cell, 3.0 mm in total thickness. Finally, we demonstrate the first continuous tunable room-temperature THz phase shifter capable of more than  $360^\circ$  of phase shift at 1.03 THz [6].

Nonetheless, electrically controlled phase shifters are deemed desirable for many applications. In our early attempt, an electrically controlled room temperature THz

phase shifter with 5CB has been performed [7]. We report the experimental demonstration, between 0.32 and 1.07 THz, a maximum phase shift of  $4.07^\circ$  is achieved at 1.07 THz when the interaction length is  $38.6 \mu\text{m}$  in the homogeneously aligned NLC cell. The driving ac voltage ( $f = 1 \text{ KHz}$ ) and corresponding field are 177 V (rms) and 589 V/cm, respectively. After that, we illustrate electrically tunable phase shifts beyond  $90^\circ$  at 1.00 THz in a homeotropically aligned  $570 \mu\text{m}$ -thick NLC cell driving at 125 V (rms) or 105 V/cm [8]. The feasibility of the device as a THz quarter-wave ( $\lambda/4$ ) plate is also verified. More recently, we successfully fabricate the first electrically tunable room-temperature  $2\pi$  NLC THz phase shifter [9]. We also compare with the parameter, figure of merit which is defined as phase shift (degrees) / insertion loss (dB), in different kinds of electrically controlled phase shifters such as single-homeotropic, double-homeotropic and single-hybrid NLC cell. The experimental results are in good agreement with calculations using the continuum theory of the NLC.



### **3.3 Magnetically Tunable Liquid-Crystal-Baesd Terahertz Phase Shifter**

The NLC THz phase shifter device consists of a homeotropically aligned NLC cell and a rotary magnet as shown in Fig. 3.1.1 The rotation axis is parallel to x-axis. The magnetic inclination angle,  $\theta$  is defined as the angle between the magnetic field direction and z-axis. The effective refractive index of NLC for THz wave changes with the NLC molecular orientation [10], which is controlled by the angle .

The phase shift due to magnetically controlled birefringence is given by Eq.3.1.3

If the magnetic field is large enough, the LC molecules are reoriented parallel to the magnetic field direction. The phase shift in Eq.3.1.3 can then be simplified as

$$\Gamma(\theta) = 2\pi d \frac{f}{c} \left\{ \left[ \frac{\cos^2(\theta)}{n_o^2} + \frac{\sin^2(\theta)}{n_e^2} \right]^{\frac{1}{2}} - n_o \right\}, \quad (3.1.4)$$

where  $n_o$  and  $n_e$  are the ordinary and extra-ordinary refractive indices of the NLC. The theoretical phase shift can be calculated from Eq. 3.1.4.

Three NLC cells have been used for magnetically tuning THz phase shifters. The structure of the first two cells is shown in Fig. 3.1.2 (a), and of the other one is shown in Fig. 3.1.2 (b). The actual total thicknesses measured by a vernier caliper are 0.93,

1.32 and 3.00 mm, respectively. When the LC layer is thicker than 2.0 mm, the orientation of LC molecules in the bulk is usually unstable and has many domains.

One obvious solution is employing multiple NLC cells. Previously, two NLC cells are used by Kwok *et al.* [11] in a polarizing color filter in visible range. Another double cell design has been used in a pulse shaper for ultrafast coherent control of excitons

by Hidaka *et al.* [12]. A NLC cell with a sandwiched structure is used in this work (Fig. 3.1.2 (b)). Compared to the use of two cells, the sandwiched cell has two less

air-silica interfaces. The reflective losses are reduced. The NLC cells have 5CB sandwiched between fused silica plates with an area of 1.0 cm by 1.0 cm for samples

of Fig. 3.1.2 (a). The two compartments for cell of the Fig. 3.1.2 (b) are filled with E7.

We use Teflon spacers for controlling the thickness of NLC layers. The inner surfaces

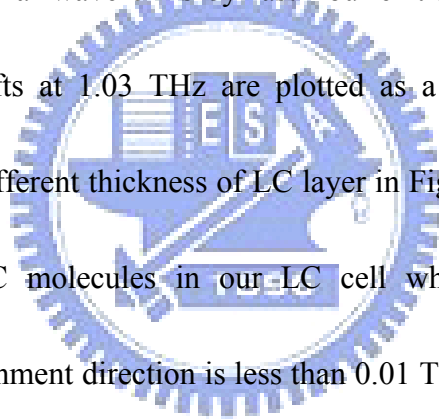
of the plates are all coated with DMOAP (N,N-dimethyl-N-octadecyl-3-aminopropyltrimethoxysilyl chloride) such that the NLC molecules are perpendicular to the substrates [13]. We employ an Nd-Fe-B sintered magnet on a rotation stage, which provides a rotatable magnetic field for tuning the phase shift of the THz wave. Further, one magnet is required instead of two. The magnetic field at the center of the LC cell is 0.43 Tesla. The achievable maximum magnetic inclination angle is 54°. Beyond that, the THz beam would be blocked by the magnet in the present setup.

The temporal THz profiles passing through the 3-mm-thick LC phase shifter at various magnetic inclination angles ( $\theta = 0^\circ, 30^\circ$  and  $50^\circ$ ) are shown in Fig. 3.1.3. The total scan range for the time delay was 12 ps. The transmitted THz waves show obviously longer time delay for larger angle,  $\theta$ . The transmitted THz field increases with  $\theta$  for  $\theta < 43^\circ$ . This can be explained by the increasing transmittance at the quartz-LC interface according to the Fresnel equations [14] shown as

$$T(\omega) = \frac{2 \cdot n_{in}}{n_{in} + n_{out}}, \quad (3.1.5)$$

where the  $T(\omega)$  and  $\omega$  are the transmittance and the frequency of the electric field of the THz wave passing through the interface and the  $n_{in}$  and the  $n_{out}$  are the refractive indices of the materials, which are in incident-side and output-side, respectively. Here we ignore the dispersion of the materials and the imaginary part of

the indices. Since both LCs we use and the fused silica have neglected dispersion and small imaginary indices. The  $n_o$  and  $n_e$  of E7 are 1.58 and 1.71, respectively, at 1.00 THz. With increasing  $\theta$ , the effective refractive index of LC will rise from 1.58 to 1.71 and become closer to the refractive index of quartz substrate, which is 1.95. The transmitted field amplitudes will then increase according to Fresnel equations. The transmitted THz field decrease for  $\theta > 43^\circ$  due to partial blocking of the THz wave by the magnet. The spectral amplitude and phase of the transmitted THz wave are deduced from the temporal waveforms by fast Fourier transform (FFT) algorithms. The deduced phase shifts at 1.03 THz are plotted as a function of the magnetic inclination angle with different thickness of LC layer in Fig. 3.1.4 The threshold field required to reorient LC molecules in our LC cell when the magnetic field is perpendicular to the alignment direction is less than 0.01 T [10], which is much lower than the magnetic field employed in this work ( $\sim 0.43$  T). This means that Eq. 3.1.4 is valid and can be used to predict the phase shifts. With Eq. 3.1.4 and the previously measured  $n_o$  and  $n_e$  of 5CB and E7 in the THz range [4, 6], we have calculated the theoretically predicted phase shifts, which are also plotted as the solid curves in Fig. 3.1.4 They show good agreements with the experimental results. According to Eq. 3.1.4 the phase shift is proportional to the product of the effective index change  $\Delta n_{eff}$ , frequency of the electromagnetic wave and the thickness of LC layer. The terahertz



wave is thus expected to experience a larger phase shift at the larger above-mentioned physical parameters in the measurement. This is also confirmed in Fig. 3.1.4. A maximum phase shift of  $108^\circ$ ,  $141^\circ$  and  $368^\circ$  are obtained at 1.03 THz and  $\theta = 54^\circ$  by using this 0.93-mm-thickness, 1.32-mm-thickness and 3.00-mm-thickness LC cell, respectively. We will discuss the merits and demerits between magnetically and electrically controlled phase shifter in the last part of this chapter.

### **3.4 Electrically Tunable Liquid-Crystal-Based Terahertz Phase Shifter**

The feasibility of electrically controlled NLC in the THz frequency range has been performed by our group [7]. The cell is prepared by sandwiching the commercial available NLC, 5CB, between two fused silica windows as substrates. The thickness of the cell is  $38.6 \pm 1.5 \mu\text{m}$ . A maximum phase shift of  $4.07^\circ$  is achieved at 1.07 THz.

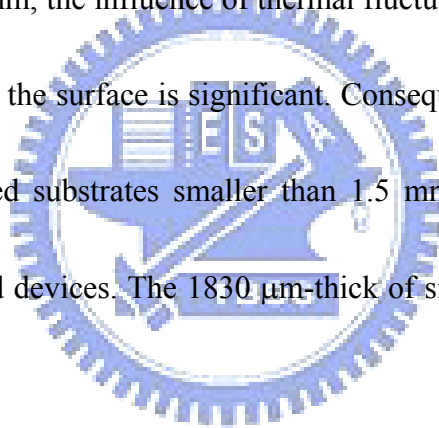
In principle, the phase shift can be increased with a thicker LC layer and optimization of the electrode geometry. The configurations of improved components are exhibited in Fig. 3.1.5 (a). Single-homeotropic, double-homeotropic and single-hybrid (one fused silica coated with DMOAP, the other coated with polyimide) E7 layer devices are drawn in Fig. 3.1.5 (b), (c) and (d) [15], respectively. In Fig. 3.1.5 (b), the thicknesses of the E7 layer is  $1830 \mu\text{m}$  for phase shift of  $2\pi$ . In Fig. 3.1.5 (c), the thickness of each E7 layer is  $1012 \mu\text{m}$ . And in Fig. 3.1.5 (d), the thickness of the E7 layer is  $1019$



$\mu\text{m}$ . The precision casting copper pieces (purity of 99.94%) worked both as spacers and electrodes for the cell. They are parallel to each other and separated by 10.2 mm.

It would require an NLC cell about 2.0 mm in thickness to obtain the  $2\pi$  phase shifts at 1.00 THz. For such thick cells, alignment of LC molecules in the bulk of the cell is not assured. The uniformity of electric field within the thick cell is also a concern. To study the alignment effects induced by DMOAP-coated substrates on NLC molecules in such thick cells, a series of cells are fabricated with different spacing and are visually analyzed using conoscopy to investigate the alignments of NLC (The data are measured and supported by Hsin-Ying Wu). The conoscopic patterns for the homeotropic aligned NLC cells with spacing of 0.44 mm, 1.64 mm, and 2.10 mm are shown in Fig. 3.1.6 (a), (b) and (c), respectively. The stripe-like patterns are due to the phase difference between the ordinary and extraordinary rays with respect to the optical axis of NLC molecules at different incident angles. The symmetry and intensity appeared in the patterns are related to the pretilt angle and thickness of NLC layers respectively. Therefore, we can obtain the thickness and pretilt angle of NLC layer simultaneously by fitting the conoscopic intensity pattern with theory used in the crystal rotation method [16]. Figure 3.1.7 shows the measured thickness of well-aligned NLC layer as indicated by  $d^*$  from conoscopic intensity pattern of cells with different spacing  $d$ . The solid line with slope  $d^*/d = 1$  indicates

that the whole LC molecules in the cell are fully aligned by surfaces. The difference between  $d^*$  and  $d$  becomes apparently large while increasing the cell spacing. It is well-known that the alignment effects of LCs in the bulk are due to the anchoring force from the oriented molecules on anisotropic surfaces. However, the reduction of the measured thickness as shown in Fig. 3.1.7 indicates that only partial LC molecules near the surface are effectively influenced by surface anchoring force. Under the long-term observation of the conoscopic intensity pattern of the NLC cell with spacing larger than 1.5 mm, the influence of thermal fluctuations on the alignments of NLC molecules far from the surface is significant. Consequently, the spacing of NLC cell with DMOAP-coated substrates smaller than 1.5 mm is the proper choice for applications of LC-based devices. The 1830  $\mu\text{m}$ -thick of single layer used is near the limit of good alignment.



A square-wave ac voltage at 1 kHz was applied to the electrodes to avoid multi domain formation. The applied voltages quoted in this dissertation are all rms values. Consider a linearly polarized THz beam passing through the cell with E7 having positive dielectric anisotropy. Without any bias field or the bias field is smaller than a threshold value, the NLC molecules are in the initially stable state and the transmitted THz beam will remain linearly polarized because the polarization of the incident THz beam is perpendicular to the NLC director. Once the bias field is larger than a

threshold value, this bias field will reorient the direction of NLC toward the bias field direction, this phenomenon is called a Fréedericksz transition [10].

The distortion free energy density per unit volume of NLC in the cell can be shown as

$$f_d = \frac{1}{2} K_1 (\nabla \cdot \hat{n})^2 + \frac{1}{2} K_2 (\hat{n} \cdot \nabla \times \hat{n})^2 + \frac{1}{2} K_3 (\hat{n} \times \nabla \times \hat{n})^2. \quad (3.1.6)$$

In our case,  $n_x=0$ ,  $n_y=\sin\phi$ ,  $n_z=\cos\phi$ , where  $\phi$  is angle from initial director,  $f_d$  is derived as

$$f_d = \frac{1}{2} K_1 \sin^2 \phi \left(\frac{d\phi}{dz}\right)^2 + \frac{1}{2} K_3 \cos^2 \phi \left(\frac{d\phi}{dz}\right)^2, \quad (3.1.7)$$

$K_1$ ,  $K_2$ , and  $K_3$  are the splay, twist, and bend elastic constant of E7, respectively.

The energy density per unit volume produced from electrical field is

$$f_e = -\int D \cdot dE = -\frac{\epsilon_v}{2} E^2 - \frac{\epsilon_a}{2} (\hat{n} \cdot \vec{E})^2, \quad (3.1.8)$$

where  $\epsilon_a = \epsilon_p - \epsilon_v$ ,  $\epsilon_v$  and  $\epsilon_p$  are the vertical and parallel dielectric constant of E7, respectively.

The total energy per unit volume is expressed as

$$f_t = f_d + f_e = \frac{1}{2} K_1 \sin^2 \phi \left(\frac{d\phi}{dz}\right)^2 + \frac{1}{2} K_3 \cos^2 \phi \left(\frac{d\phi}{dz}\right)^2 - \frac{\epsilon_v}{2} E^2 - \frac{\epsilon_a}{2} (\hat{n} \cdot \vec{E})^2. \quad (3.1.9)$$

At equilibrium, Eq. 3.1.9 is derived to

$$\frac{d}{dz} \left[ \left( k_1 \sin^2 \phi \left(\frac{d\phi}{dz}\right)^2 + k_3 \cos^2 \phi \left(\frac{d\phi}{dz}\right)^2 \right) + \epsilon_a \epsilon_o E^2 \sin^2 \phi \right] = 0, \quad (3.1.10)$$

At center of E7 sample,  $\phi = \phi_m$  is the maximum value and  $\frac{d\phi_m}{dz} = 0$

$$\epsilon_a \epsilon_o E^2 \sin^2 \phi_m = (K_1 \sin^2 \phi + k_3 \cos^2 \phi) \left(\frac{d\phi}{dz}\right)^2 + \epsilon_a \epsilon_o E^2 \sin \phi, \quad (3.1.11)$$

$$\int_0^{\frac{d}{2}} (\varepsilon_o \varepsilon_a)^{1/2} E dz = \int_0^{\varphi_m} \left( \frac{k_1 \sin^2 \varphi + k_3 \cos^2 \varphi}{\sin^2 \varphi_m - \sin^2 \varphi} \right)^{1/2} d\varphi, \quad (3.1.12)$$

$\phi_m=0$  for threshold value

$$E_{th} = \frac{\pi}{d} \sqrt{\frac{K_3}{\varepsilon_o \varepsilon_a}}, \quad (3.1.13)$$

and in MKS units is rewritten as

$$V_{th} = \pi \frac{l}{d} \sqrt{\frac{K_3}{\varepsilon_o \varepsilon_a}}, \quad (3.1.14)$$

As a result, the effective refractive index of the NLC layer will be changed with applied electric field. The threshold voltage or field,  $V_{th} = \pi \frac{l}{d} \left( \frac{k_3}{\varepsilon_o \varepsilon_a} \right)^{1/2}$  or  $E_{th} = \frac{V_{th}}{l}$ ,

where  $l$  is the distance between two electrodes,  $d$  is thickness of the NLC layer,  $k_3$ ,  $\varepsilon_a = \varepsilon_{\parallel} - \varepsilon_{\perp}$  and  $\varepsilon_o$  are the bend elastic constant, dielectric anisotropy, and electric permittivity of free space, respectively. For double E7 layers  $2\pi$  phase shifter, we

calculated that  $E_{th} = 11.62$  V/cm, with  $L=10.2$  mm,  $d=1012$   $\mu\text{m}$ ,  $k_3=17.1 \times 10^{-12}$  N,  $\varepsilon_a=13.8$  (from Merck). The usual analysis of electrically controlled birefringence of

an NLC cell used applied voltage. It implied that the expression  $V = EL$  is a good approximation. Because of the thick cell used in this work, the uniformity of the

electrical field is a concern. We have thus taken a more general approach and formulated phase shift as a function of electrical field. The phase shift,  $\Gamma(E)$ ,

experienced by the THz beam transmitted through the cell biased at a electric field  $E$  is given by

$$\Gamma(E) = \int_0^d \frac{2\pi f}{c} \Delta n_{eff}(E, z) dz, \quad (3.1.15)$$

where  $\Delta n_{eff}(E, z)$  is the change of effective birefringence for NLC at a position  $z$  along the propagation direction of the THz beam. The effective birefringence can be written as

$$\Delta n_{eff} = \left( \frac{\cos^2 \theta}{n_o^2} + \frac{\sin^2 \theta}{n_e^2} \right)^{-\frac{1}{2}} - n_o, \quad (3.1.16)$$

where  $\theta$  is the reorientation angle of NLC molecules from the initial orientation. For  $E > E_{th}$  the angle  $\theta$  at any point  $z$  in the cell can be computed using the relation [17],

$$\frac{z}{d} = \frac{E_{th}}{\pi E} \int_0^\theta \left( \frac{1 + q \sin^2 \theta}{\sin^2 \theta_m - \sin^2 \theta} \right)^{\frac{1}{2}} d\theta, \quad (3.1.17)$$

where  $q = (k_1 - k_3)/k_3$ , and  $k_1$  ( $= 11.1 \times 10^{-12} \text{ N}$  for E7) is the splay elastic constant of NLC. The angle  $\theta_m$  is the maximum reorientation angle located at  $z = d/2$ . It is related to  $E/E_{th}$  by

$$\frac{E}{E_{th}} = \frac{2}{\pi} \int_0^{\theta_m} \left( \frac{1 + q \sin^2 \theta}{\sin^2 \theta_m - \sin^2 \theta} \right)^{\frac{1}{2}} d\theta. \quad (3.1.18)$$

In a uniform electric field approximation,  $E$  can be written as  $V/l$ . Equations 3.17 and 3.18 allow us to calculate the profile of molecular orientation in the cell for a given applied voltage or electric field.

The temporal waveforms of the THz pulse transmitted through the double layers device at several applied voltages are shown in Fig. 3.1.8 (a). Figure 3.1.8 (b) shows the transmitted THz temporal signals in two different ways to apply voltages. One is increase of applied voltages from 0V to 45V (solid curves), the other is

decrease of applied voltages from 45V to 0V (dash curves). The correspondent transmission curves do not coincide with each other in two manipulating ways at the same voltages. It may arise from that the gap of cell, compared with traditional LC cell in the visible, is too thick and the distance of electrodes is too far. The translation stage in our system is driven by a stepper motor with a 10 μm step resolution (equivalent to a temporal resolution of 66.67 fs). The total scanning duration of one measurement was 68 ps. The transmitted THz pulses exhibit clearly larger delay and higher transmittance at higher applied voltages. This trend is explained by the same reason as the Fresnel equations. The experimentally measured ratio of power transmittance for e-ray and o-ray is 1.37, which is almost identical to the theoretically calculated value of 1.03. According to Eq. 3.1.4, larger phase shift is expected at higher frequencies. For a 45.0V, the measured phase shift varied linearly with frequency, with a slope of 362.6°/THz. Fig. 3.1.9 shows the phase shift as a function of driving voltage. The curves are theoretical predictions according to Eqs. 3.1.15 - 3.1.18 (The curves are calculated by Hsin-Ying Wu and Tsung-Ta Tang). The theories and measurements fitted together neatly except in low applied bias near threshold. The rise and fall time of LC device may cause this phenomenon. The turn on (rise) and turn off (fall) time of LC molecules in the cell are described as

$$\tau_{\text{on}} = \frac{\gamma l^2}{(V^2 - V_{th}^2)\epsilon_0 \epsilon_a}$$

$$\tau_{\text{off}} = \frac{\gamma l^2}{V_{th}^2 \epsilon_0 \epsilon_a}, \quad (3.1.19)$$

where  $\gamma$  is rotational viscosity of NLC. Form Eq. 3.1.19, the rise time and fall time of our double layers device are around 30 and 600 sec, respectively. In each measurement, we characterize the device after changing applied voltage for 30 min. So the curves in Fig. 3.1.10 (a), (b) and (c) may mainly be postponed by backflow of NLC rather than response time.

A maximum phase shift of  $367^\circ$  was achieved at 1.05 THz when the cell was driven at 45.0 V/cm. The theoretically predicted phase shift was  $363.9^\circ$ . The threshold field was found to be 13.73 V/cm, also in agreement with the theoretically predicted value, 11.62 V/cm. To confirm that the present device can be used as a wave plate, we also recorded the transmittance through the device as it was rotated with angle  $\phi$  about the axis of propagation at 0.29 and 0.59 THz (Fig. 3.1.11). The results (solid circles) show clearly the squared sinusoidal law dependence for the transmittance and the correct period for a  $\lambda/4$  and  $\lambda/2$  plate at 0.29 and 0.59 THz, respectively. The transmittance of the ideal  $\lambda/4$  and  $\lambda/2$  plate,  $1 - \frac{1}{2} \sin^2(2\phi)$  and  $1 - \sin^2(2\phi)$ , are also plotted as the solid curve in Fig. 3.1.11 (a) and (b), which fit the experimental data. The error bar is due to Ti: sapphire laser power fluctuation and possibly scattering losses by the THz beam propagating through the NLC layer.

Far above threshold, the NLC molecules are essentially aligned with the electrical field. The theoretical curves are in good agreements with the experiments. For applied field near and about threshold, the theoretical phase shift values tend to be larger than those of the experimental ones. The experimental threshold field was found to be 13.73 V/cm, higher than the theoretically predicted values, 11.62 V/cm. This is reasonable, as the actual electric field reorienting the NLC molecules in the thick cell is lower than the average electric field given by  $V/L$ . We have calculated the field distribution in our device using FEMLab (a finite element software by COMSOL, Inc.). Within more than 80% of the 1.0-cm-diameter THz beam area, the actual electric field is smaller than the average electric field. At the center of the cell, the actual electric field is 95% of  $V/L$ . Because the average electric field is used in the theoretical calculation, the theoretical phase shifts will be larger than the experimental values. This is may another reason to cause the hysteresis phenomena in Fig. 3.1.10.

### 3.5 Discussion

The magnetically controlled LC THz are more stable than the electrically one because the applied magnetical field ( $\sim 0.43$  T) is always enormously greater than threshold value ( $\sim 0.01$  T). We can omit the quality of the LC molecules alignment by substrates. The continuous tuning phase shifts can be obtained by magnetically controlled LC THz phase shifter. However, the electrically controlled NLC THz



phase shifter are compact to work as THz wave plate. We should point out that it is difficult to tune the desired phase shift accurately near the threshold because of sharp slope. This drawback can be overcome by using the hybrid aligned structure as shown in Fig.3.1.5 (d). The distance of two electrodes of single-hybrid layer device is 12.2 mm. We compare phase shift versus applied voltage of single-homeotropic and single-hybrid aligned devices in Fig. 3.1.12. From Fig. 3.1.12, there is no threshold effect in the single-hybrid sample and the curve shows moderate slope. To achieve phase shift of 90 degree, the interaction thickness of single-homeotropic sample is just a half of single-hybrid one. But the response of the electrical device is still slow, due to its thickness. It is thus not suitable for applications that require fast modulation. In the principle, we can use the multi-layers structure to make the response time faster. We define the parameter to present figure of merit of our electrical THz phase shifter in Fig. 3.1.13. Figure of merit is defined as phase shift (degrees) / insertion loss (dB). The double-homeotropic layers device performs best figure of merit in THz frequency range. Alternatively, one can design a homogeneously aligned cell with negative dielectric anisotropy NLC. Unfortunately, Indium-Tin-Oxide (ITO), commonly employed as transparent electrodes for LC cells in the visible, strongly attenuates electromagnetic waves in the THz frequency range [18].

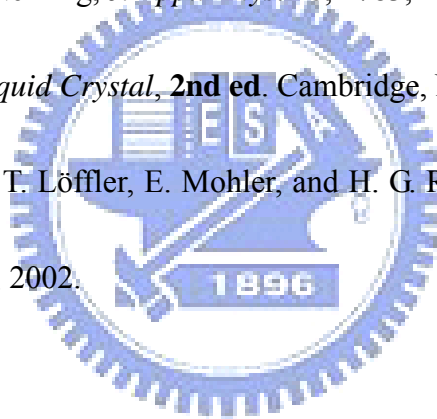
In summary, we have demonstrated a room temperature magnetically and electrically controlled THz phase shifter by using a sandwiched LC cell. Double-thick liquid crystal layers are constructed in this work to increase the interaction length while minimizing interface Fresnel losses. The vertical alignment of the thick liquid crystal layer (200 ~ 2100  $\mu\text{m}$ ) is checked by conoscopy system. A maximum phase shift of  $368^\circ$  at 1.03 THz has been achieved successfully by magnetically controlling. The phase shift can be continuously tuned magnetically by controlling the effective refractive index of LC layer. And a maximum phase shift of  $367^\circ$  at 1.05 THz is realized by using electrically controlled birefringence in a homeotropically aligned nematic LC (E7) dual cell, 1012  $\mu\text{m}/\text{layer}$  in thickness. The driving voltage required for a phase shift of  $367^\circ$  is 45 V (rms). The electric field distribution in the device has been calculated by using FEMLab. We also demonstrate that the phase shifter works as the electrically switchable quarter wave ( $\lambda/4$ ) plate at 0.29 THz and half wave ( $\lambda/2$ ) plate at 0.59 THz. The double-homeotropic cell has better figure of merit about 40  $\text{degree}/^\circ\text{B}$ . The results are in good agreement with theoretical predictions. Alternatively, newly developed liquid crystal material with high birefringence can be explored for this application.

## References

1. I. H. Libon, S. Baumgärtner, M. Hempel, N. E. Hecker, J. Feldmann, M. Koch, and P. Dawson, *Appl. Phys. Lett.* **76**, 2821, 2000.
2. R. Kersting, G. Strasser, and K. Unterrainer, *Electron. Lett.* **36**, 1156, 2000.
3. T. Kleine Ostmann, M. Koch, and P. Dawson, *Microwave Opt. Tech. Lett.* **35**, 343, 2002.
4. R. P. Pan, C. L. Pan, C. Y. Chen, and C. F. Hsieh, *J. Appl. Phys.*, **103**, 093523, 2008.
5. C.Y. Chen, T.R. Tsai, C.L. Pan, and R.P. Pan, *Appl. Phys. Lett.* **83**, 4497, 2003.
6. C. Y. Chen, C. F. Hsieh, Y. F. Lin, R. P. Pan, and C. L. Pan, *Opt. Exp.*, **12**, 2625, 2004.
7. T.R. Tsai, C.Y. Chen, R.P. Pan, C.L. Pan, and X.-C. Zhang, *IEEE Microwave Wireless Comp. Lett.* **14**, 77, 2004.
8. C. F. Hsieh, R. P. Pan, T. T. Tang, H. L. Chen, and C. L. Pan, *Opt. Letts*, **31**, 1112, 2006.
9. H. Y. Wu, C. F. Hsieh, T. T. Tang, R. P. Pan, and C. L. Pan, *IEEE Photonic Tech. Lett.*, **18**, 1488, 2006.
10. P. G. de Gennes and J. Prost, “*The Physics of Liquid Crystals*”, **2nd ed.** (Oxford, New York, 1983).



11. D.-D. Huang, X.-J. Yu, H.-C. Huang, and H.-S. Kwok, *Appl. Opt.* **41**, 4638, 2002.
12. K. Komori, T. Sugaya, M. Watanabe, T. Hidaka, *Jan. J. Appl. Phys.* **39**, 2347 2000.
13. F. J. Kahn, *Appl. Phys. Lett.* **22**, 386, 1973.
14. Eugene Hecht, “*Optics*”, **3rd ed.** (Addison Wesley Longman, New York, 1998),  
Chap. 4.
15. Shoichi Matsumoto, Masahiro Kawamoto and Kiyosgi Mizunoya, *J. of Appl. Phys.*, **47**, 3842, 1976.
16. T. J. Scheffer and J. Nehring, *J. Appl. Phys.* **48**, 1783, 1977.
17. S. Chandrasekhar, *Liquid Crystal*, **2nd ed.** Cambridge, New York, 1992.
18. T. Bauer, J. S. Kolb, T. Löffler, E. Mohler, and H. G. Roskos, U. C. Pernisz, *J. of Appl. Phys.* **92**, 2210, 2002.



## Figures:

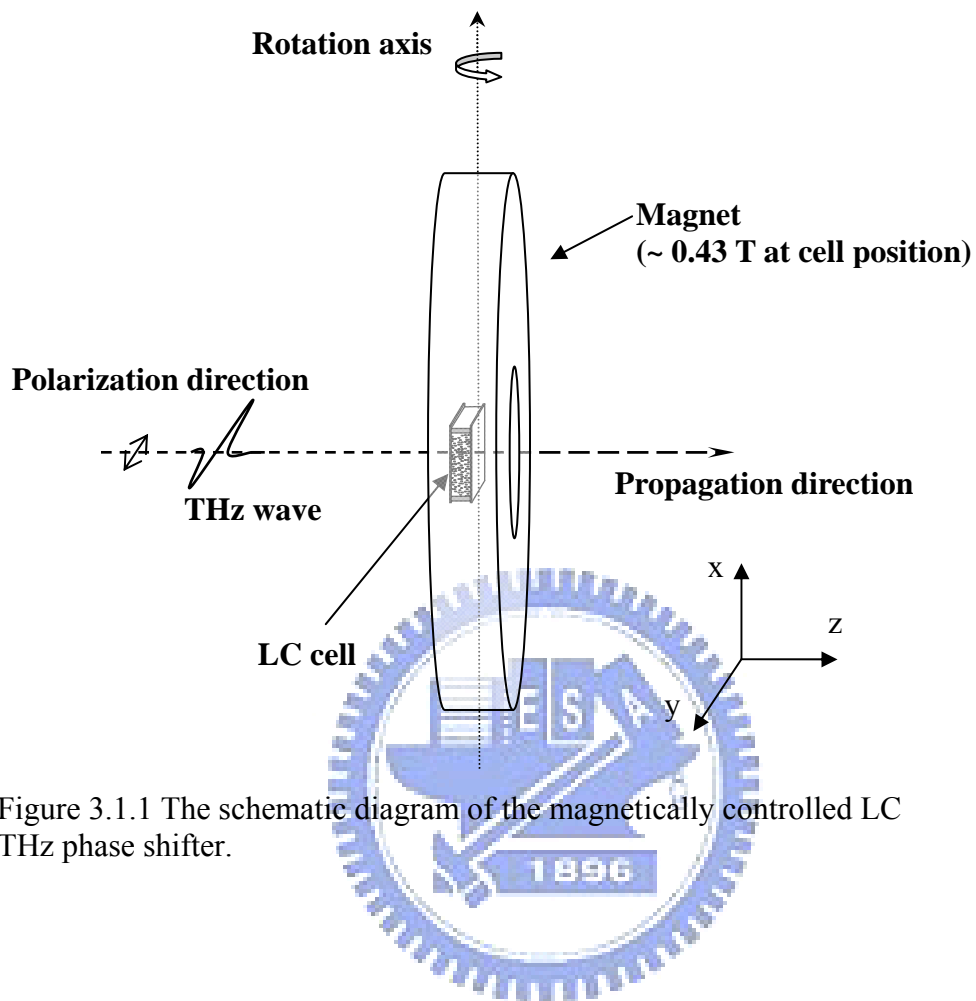


Figure 3.1.1 The schematic diagram of the magnetically controlled LC THz phase shifter.

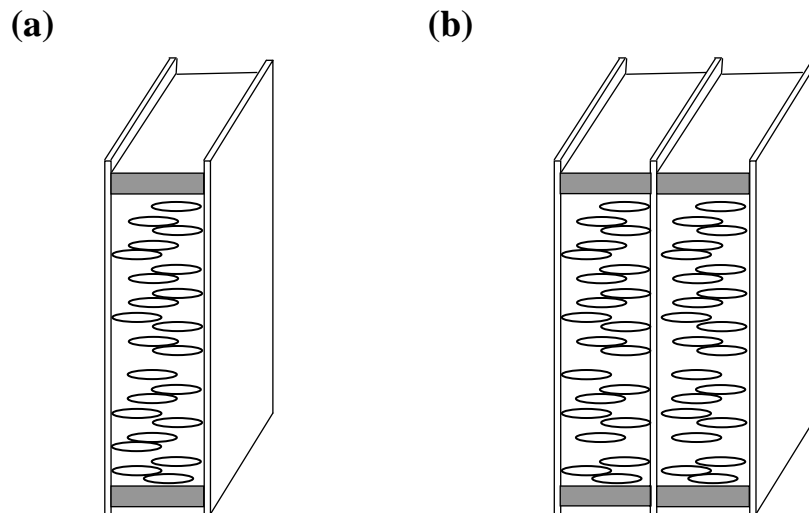


Figure 3.1.2 The sample of the magnetically controlled LC THz phase shifter. The substrates are fused silica plates. The Teflon spacers are used for controlling the thickness. (a) The cell with one layer of LC, and (b) the cell with two layers of LC.



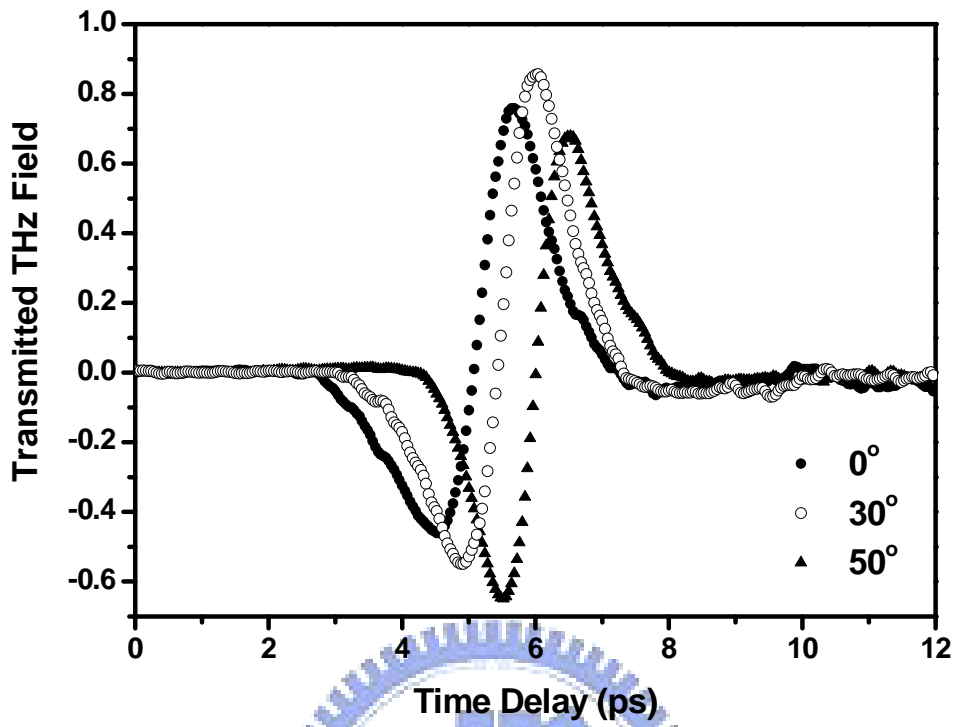
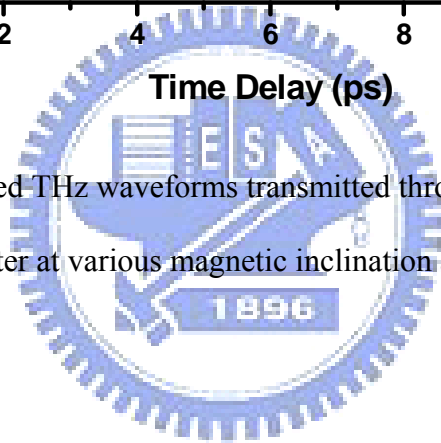


Figure 3.1.3 The measured THz waveforms transmitted through the magnetically controlled LC phase shifter at various magnetic inclination angles.



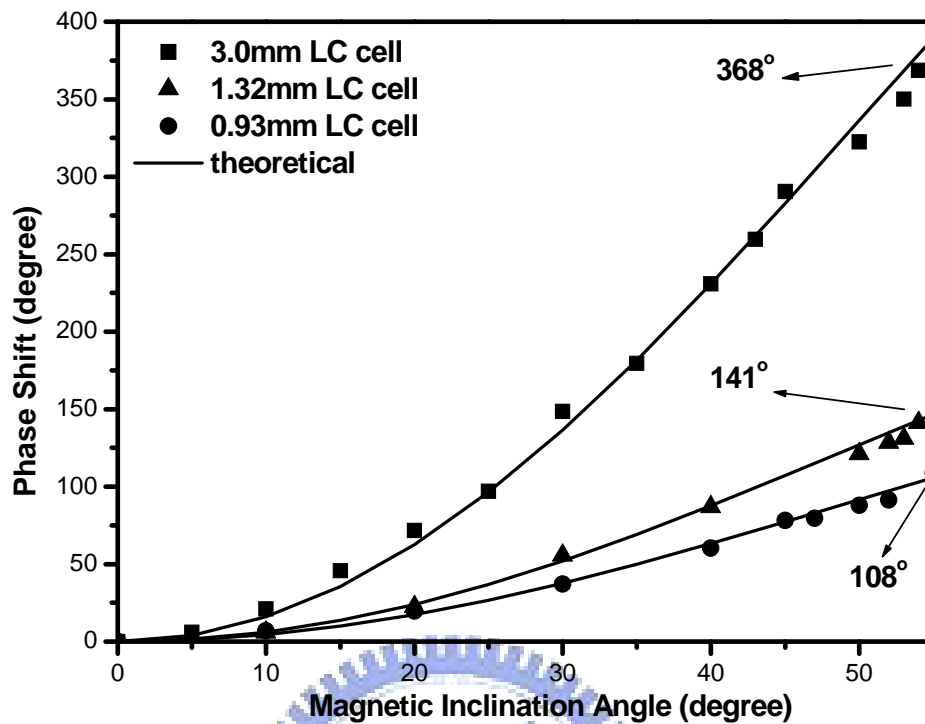


Figure 3.1.4 The phase shift of the THz waves passing through the 0.93-mm LC cell, the 1.32-mm cell and 3.00-mm cell versus the magnetic inclination angle  $\theta$  at 1.03 THz. The solid curves are from the theoretical predictions. The symbols “●”, “▲” and “■” show the measured data from 0.93-mm, 1.32-mm and 3.00-mm cells, respectively.



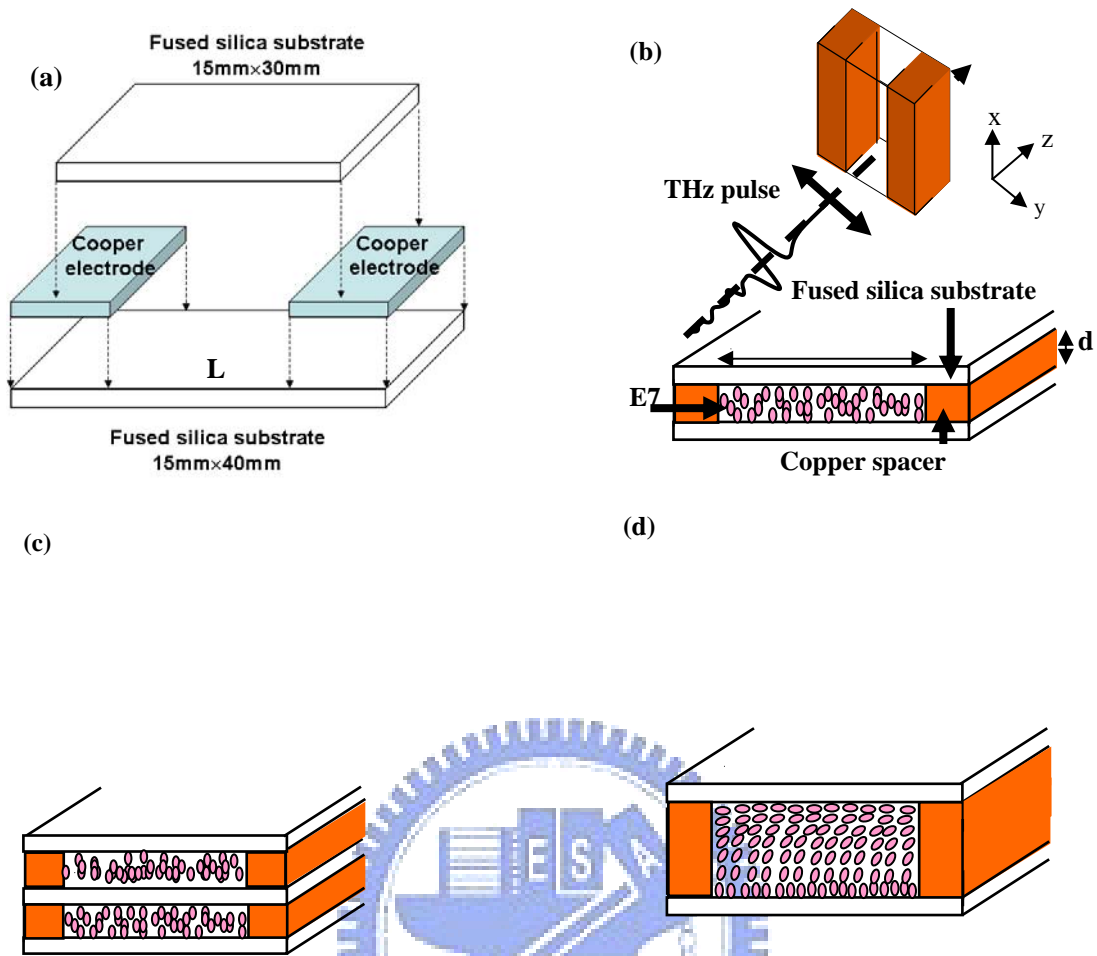
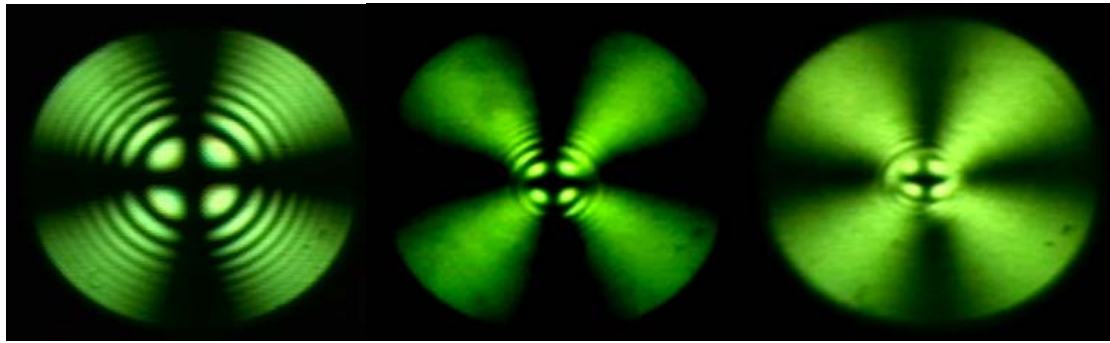


Figure 3.1.5 (a) Schematic drawing of the improved electrically tunable liquid crystal THz phase shifter. The coppers are used as spacers and electrodes. (b) the cell with one homeotropic layer of E7, (c) the cell with two homeotropic layers of E7, and (d) the cell with one hybrid layer of E7. The THz wave propagation and polarization directions are z and y, respectively.



(a)

(b)

(c)

Figure 3.1.6 Conoscopic intensity patterns of 0.44-, 1.64- and 2.10-mm LC cells are shown in (a), (b) and (c), respectively.



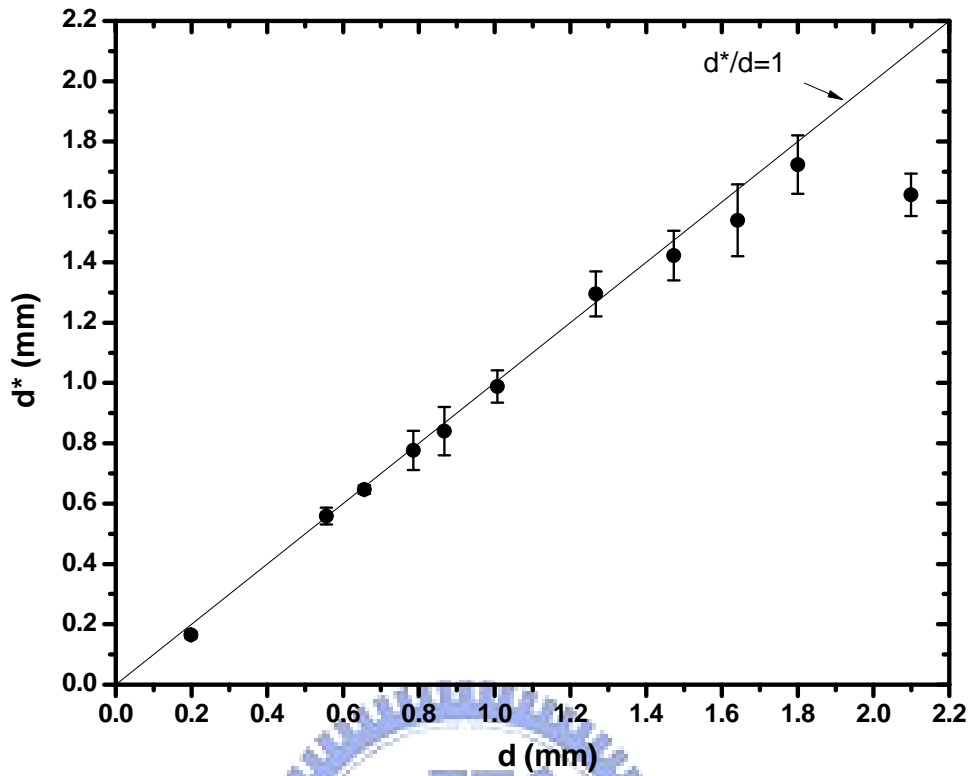


Figure 3.1.7 The measured thickness of well-aligned NLC layer as indicated by  $d^*$  from conoscopic intensity pattern of cells with different spacing  $d$ . The solid line is ideal curve with slope  $d^*/d=1$ .

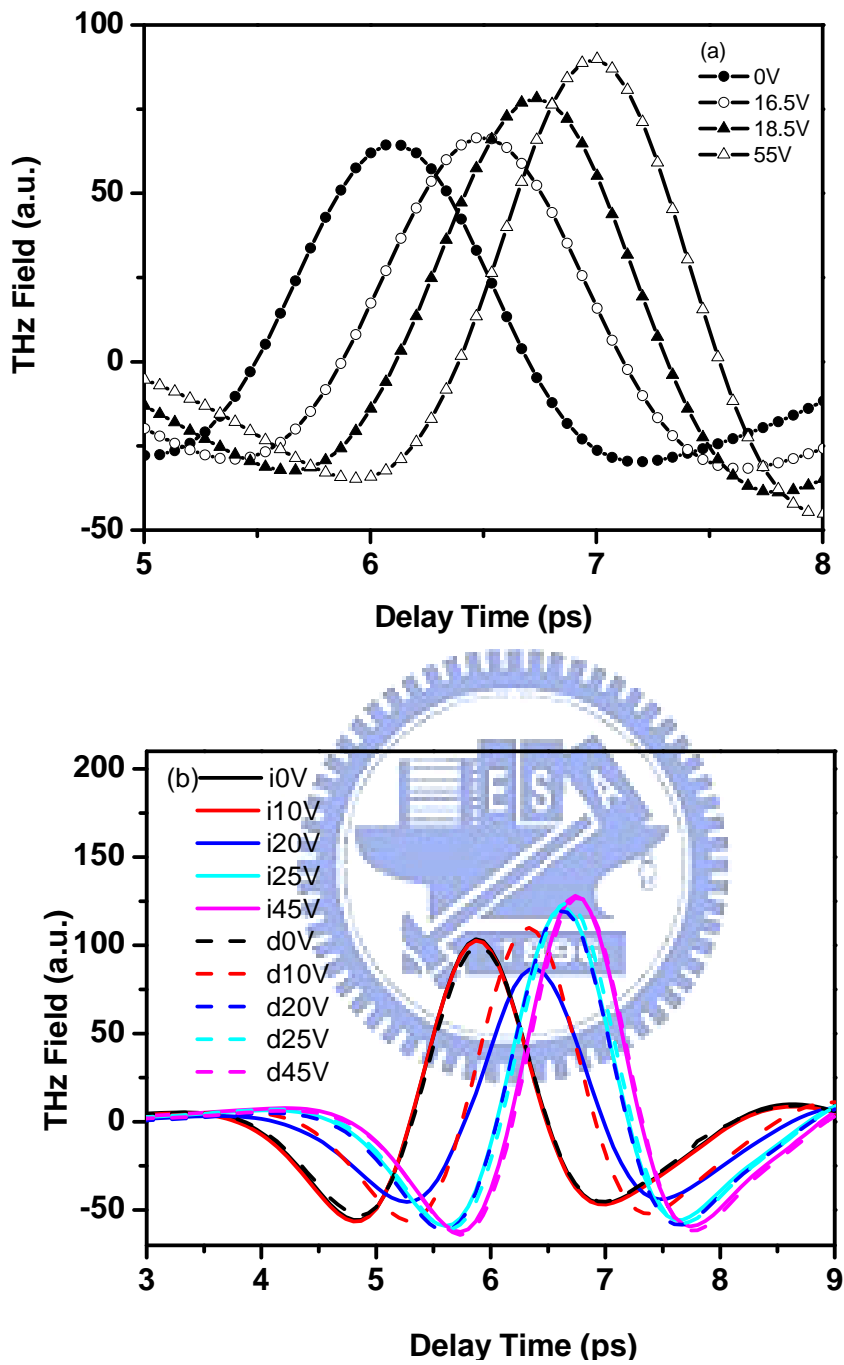


Figure 3.1.8 (a) The temporal waveforms of the THz pulse transmitted through the double layers LC cell at various applied voltages. (b) The solid and dash lines present the increase way and decrease way to apply bias, respectively.

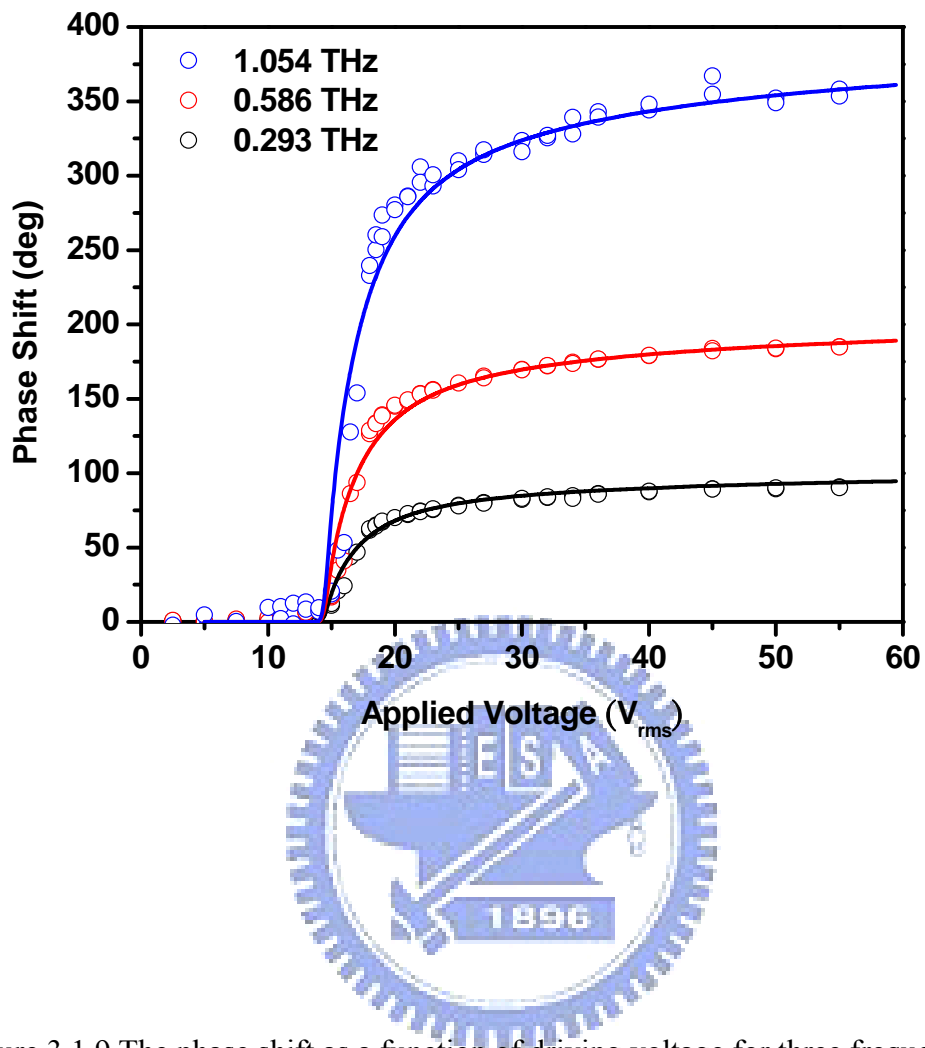


Figure 3.1.9 The phase shift as a function of driving voltage for three frequencies. The solid curves are from the theoretical prediction.

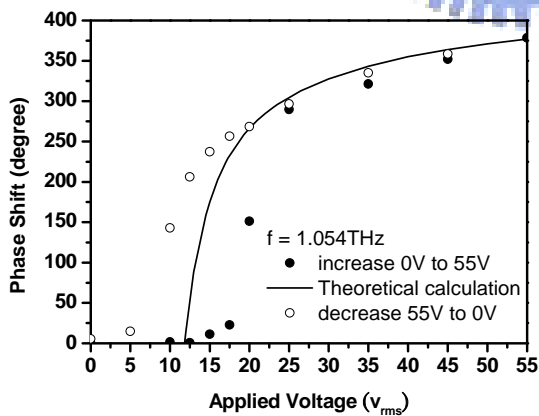
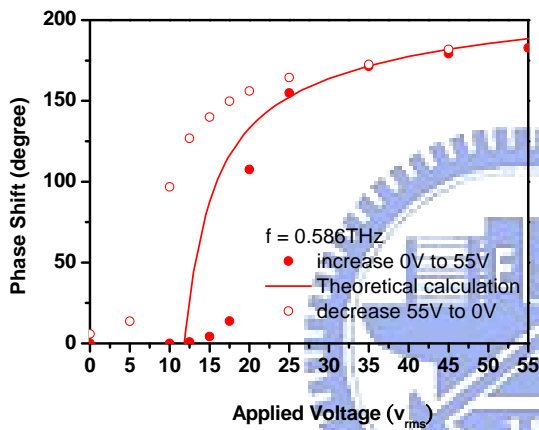
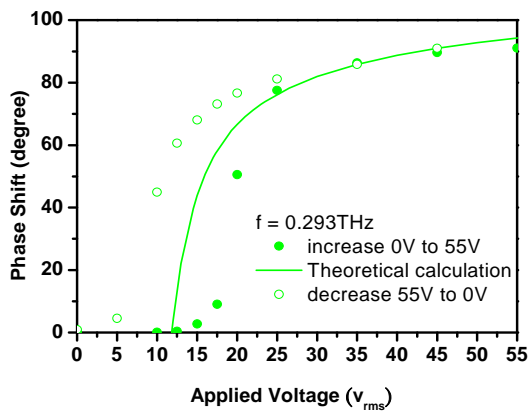
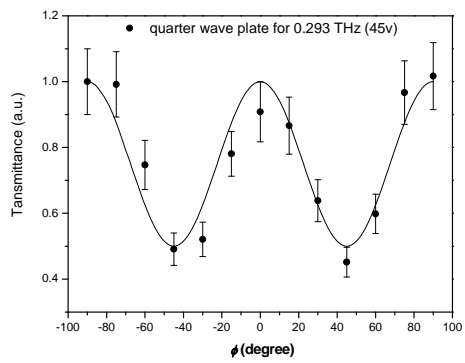


Figure 3.1.10 The phase shift as a function of driving voltage for three frequencies.

The hysteresis phenomenon is shown in these three data.

(a)



(b)

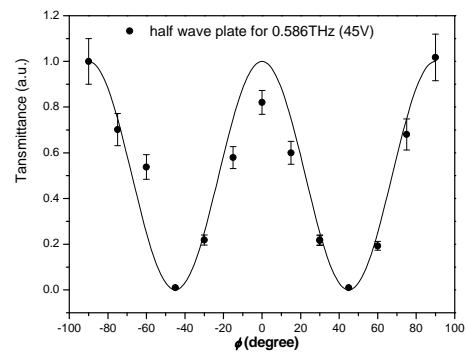
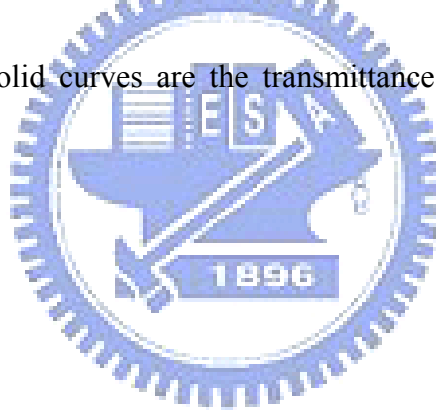


Figure 3.1.11 Transmittance of the device as it was rotated about the THz beam propagation axis. The solid curves are the transmittance for the ideal  $\lambda/4$  and  $\lambda/2$  plate.



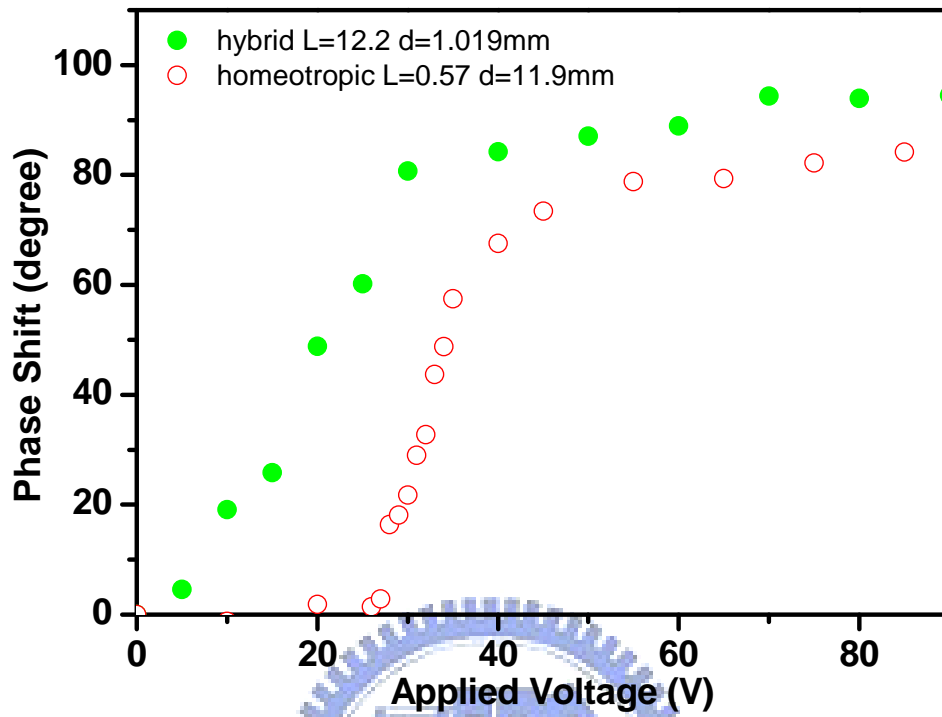


Figure 3.1.12 Phase shift versus applied voltage of single-homeotropic and single-hybrid aligned devices.



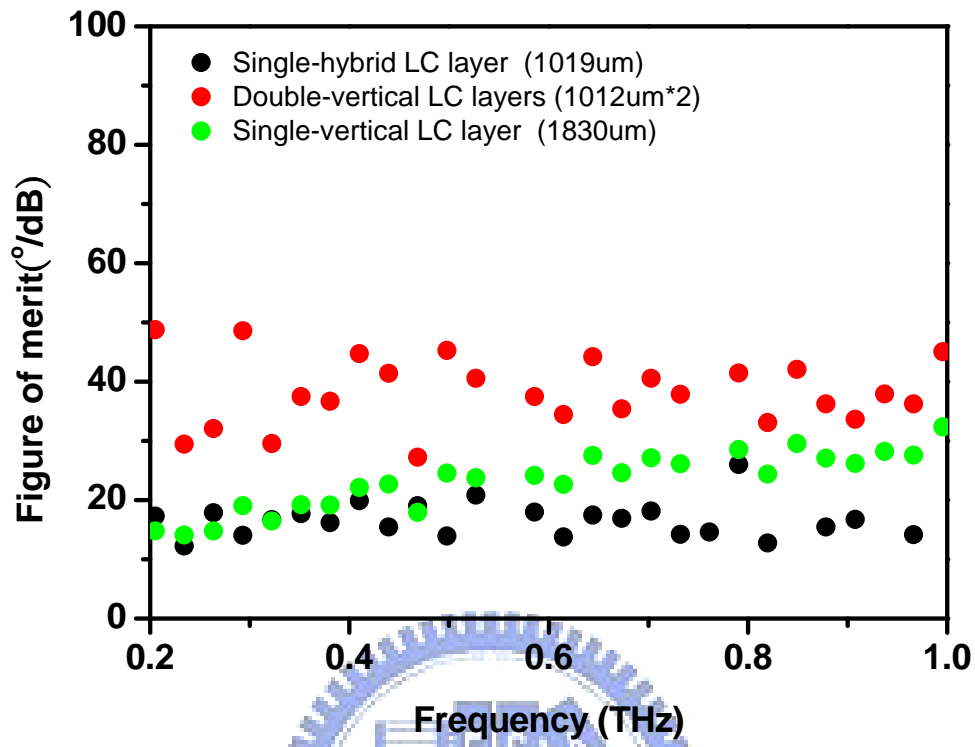


Figure 3.1.13 Figure of merit of single-homeotropic, double-homeotropic and single-hybrid structure devices.

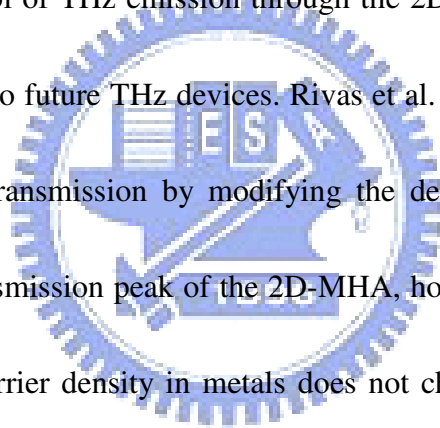
# Chapter 4 Control of Extraordinary Transmission of Metallic Holes Array by Nematic Liquid Crystal

## 4.1 Metallic Holes Array

Metal films with two-dimensional periodic arrays of sub-wavelength holes (2D-MHA), can exhibit extraordinary optical transmission characteristics [1-3]. This discovery attracts much attention because of its potential applications for sub-wavelength optics, data storage, microscopy and bio-photonics [4]. Extensive work on the mechanism of the extraordinary transmission has been carried out both theoretically and experimentally [2, 5-7]. The enhanced transmission is now understood to be due to the resonant coupling of incident light with surface plasmon polaritons (SPPs) [8]. The SPP enhancement is observed in the case where no propagation mode is supported in the metal hole and the transmission peak frequency depends on the geometry of the structure [9], the angle of incidence of the radiation [1,2], depth of the holes [10], and can be tuned by the refractive index of the adjacent medium [5-7,9,11]. The tunability of extraordinary transmission might lead to applications such as brighter flat-panel displays, spatial light modulators and tunable optical filters [2,11].

In the millimeter wave and terahertz (THz) regions, a 2D-MHA acts as a band-pass filter or frequency selective surface [12,13]. The band-pass peak frequency

is above the cutoff frequency of the hole in this case. For such band-pass filters, the transmittance is several times larger than the porosity of the holes, and hence such transmission characteristics can also be called extraordinary transmission similar to that observed at optical wavelengths [1]. Very recently, enhanced THz transmission has been reported for sub-wavelength hole arrays in metal films [14,15] and doped semiconductor plates [16]. These advances are significant as they could lead to the realization of efficient THz sub-wavelength optics for ultra-sensitive THz sensing and imaging systems. Control of THz emission through the 2D-MHA is also expected to add new functionalities to future THz devices. Rivas et al. [17] demonstrated thermal switching of the THz transmission by modifying the density of free carriers in a silicon grating. The transmission peak of the 2D-MHA, however, can not be tuned in this way because the carrier density in metals does not change with temperature. A metallic photonic crystal was made tunable over the range of 365-386 GHz by a relative lateral shift of 140  $\mu\text{m}$  between two micromachined metallic photonic crystal plates [18]. The insertion loss and Q of the device are 3-7 dB and 20-30, respectively. By use of  $\text{SrTiO}_3$  as a defect material inserted into a periodic structure of alternating layers of quartz and high-permittivity ceramic, Nemeč et al. [19] was able to tune a single defect mode in the 1D photonic crystal from 185 GHz at room temperature down to 100 GHz at 100 K by thermal tuning. The peak transmittance exceeds -9 dB.



In the near IR, Kim et al. [11] modulated the transmission amplitude (by 25%) of a perforated metal film–liquid crystal–indium tin oxide cell by varying the voltage applied to the LC. The spectral shift in the data is not immediately apparent, however, because the spectral features were quite broad in that experiment.

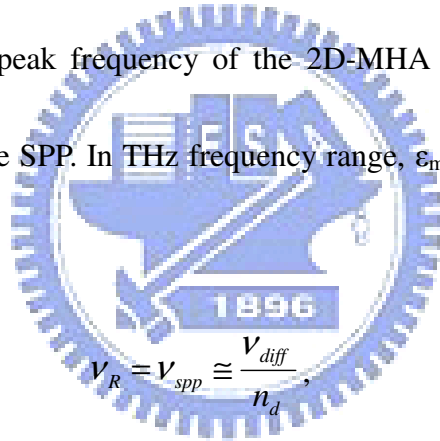
Perhaps the transmission peak of the 2D-MHA can be tuned by using magnetically controlling refractive index of NLC filling in the metal interface. It can be achieved in room temperature. We also analyze the transmission of dielectric material (Certified Refractive Index Liquids) filling in the MHAs. We will discuss the differences of transmission properties between filled with NLCs and Certified Refractive Index Liquids.

## 4.2 Theoretical Prediction

For a perfect metal, the transmission spectrum of the 2D-MHA with a hexagonal lattice of circular holes in the THz region is characterized by three characteristic frequencies; the cutoff frequency of the  $TE_{11}$  mode,  $\nu_c = 1.841c/\pi d$ , where  $c$  is the speed of light in the holes and  $d$  is the diameter of the hole; the diffraction frequency,  $\nu_{\text{diff}} = 2c'/1.732s$ , where  $c'$  is the speed of light in the medium adjacent to the metal interface,  $s$  is the hexagonal lattice constant; and the resonant frequency of the SPP on a structured surface [2],

$$v_R = v_{spp} = \left| \vec{k}_{in} + \vec{G} \right| \frac{c_0}{2\pi} \sqrt{\frac{\epsilon_m + \epsilon_d}{\epsilon_m \epsilon_d}}, \quad (4.1)$$

where  $k_{in}$  is the in-plane wave vector component of the incident THz wave,  $c_0$  is the speed of light in vacuum,  $G$  is the reciprocal lattice vectors of the periodic structure,  $\epsilon_m$  and  $\epsilon_d$  are the dielectric constants of the metal and the adjacent dielectric medium, respectively;  $v_c$  determines the lower frequency limit below which electromagnetic waves become evanescent in the metallic circular hole.  $v_{diff}$  determines the lowest frequency above which electromagnetic waves are diffracted into the first diffraction lobe. The transmission peak frequency of the 2D-MHA almost coincides with the resonant frequency of the SPP. In THz frequency range,  $\epsilon_m \gg \epsilon_d$ , the peak frequency of the 2D-MHA,



$$v_R = v_{spp} \cong \frac{v_{diff}}{n_d}, \quad (4.2)$$

where  $v_{spp}$  is the SPP resonance frequency, where  $n_d$  is the refractive index of the dielectric medium. It is possible to tune  $v_{spp}$  monotonically by varying  $n_d$ .

### 4.3 Experimental Methods

The large birefringence and small extinction coefficient of LCs (4'-n-pentyl-4-cyanobiphenyl or 5CB) is measured and has been employed at THz wave signals by our group [20]. We have measured the complex refractive index of 5CB at room temperature by THz time-domain spectroscopy. Consequently, we demonstrate frequency tuning of enhanced THz radiation transmitted through a

2D-MHA by controlling the effective refractive index of 5CB filling the holes and adjacent to the 2D-MHA on one side. Then we use two Certified Refractive Index Liquids (the refractive indices are close to  $n_e$  and  $n_o$  of 5CB, respectively) in the holes and adjacent to the 2D-MHA on one side. Comparing the difference between these two transmissions helps us to understand the fundamental physics of MHA.

The THz tunable filter consists of a 2D-MHA with 5CB layer and a pair of rotary permanent magnets as shown in Fig. 4.1. And the 2D-MHA with CRIL has the same structure except the assembly of the rotating magnets. The 2D-MHA is a 0.5 mm-thick aluminum plate perforated with circular holes arrayed in a hexagonal lattice of lattice constant  $s = 0.99$  mm and the diameter of each hole,  $d = 0.56$  mm. The 2D-MHA is machined on the one side and sandwiched by a pair of Mylar sheets (75  $\mu\text{m}$  in thickness) so that a box-like structure of dimension,  $0.15 \times 15.0 \times 15.0$  mm<sup>3</sup>, in the center of the 2D-MHA is formed for holding the 5CB (Aldrich, 98% purity) or CRIL. The holes of the MHA are also filled with 5CB or CRIL. Two Nd-Fe-B sintered magnets are used to align the LC molecules and provide a rotatable external field for tuning the effective refractive index of 5CB.  $\theta$  and  $\phi$  are defined as the angle between the magnetic field and the polarization direction of THz signal (y axis) in x-y and y-x plates. The rotation axis of  $\theta$  and  $\phi$  is Z and X, respectively. The effective refractive index of LC changes with the LC molecular orientation, which is controlled by  $\theta$ . The magnetic field at the center on the sample is 0.15 T, which is triple larger than the critical field ( $\sim 0.05$  T) required for aligning the LC molecules to the field [21]. The LC cell is not aligned by any other means.  $n_d$  of the LC infiltrated in and on one side of the 2D-MHA is changed from extra-ordinary refractive index,  $n_e = 1.75$  to ordinary refractive index,  $n_o = 1.57$ . The refractive indices of CRIL are 1.7 and 1.58, respectively. The effective refractive index of LCs,

$$n_d = \left\{ \left[ \frac{\sin^2(\theta)}{n_o^2} + \frac{\cos^2(\theta)}{n_e^2} \right]^{-\frac{1}{2}} \right\}, \quad (4.3)$$

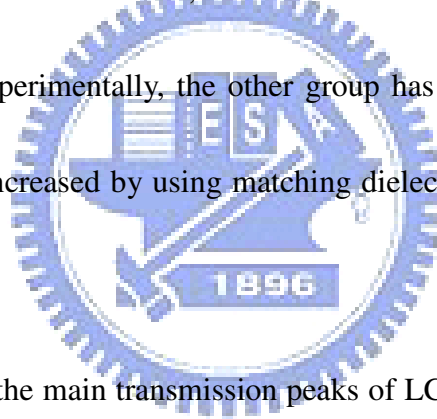
By rotating the magnet assembly along  $\theta$  while keeping the sample stationary, we only change  $n_d$  without affecting the polarization direction of the THz wave. The maximum  $\theta$  is  $55^\circ$ . Beyond that, the THz beam would be blocked by the magnet in the current experimental setup. As for rotating along X-axis ( $\phi$ ), we affect the polarization direction of the THz wave. We can image that a birefringent material with its optical axes rotated in the Y - Z plane. Because of the rotation of birefringence, the THz waves which pass through this sample will be separated into e-ray and o-ray. In theory, the transmittance can be changed but the peak frequency is constant.

Spectral transmission of the filter is characterized by using a photoconductive-antenna-based THz time-domain spectrometer. The polarization direction of THz waves is perpendicular to the normal of optical table. The size of the 2D-MHA (about 250 holes in the aperture) is large enough to avoid the finite size effect [21].

## 4.4 Results and Discussions

Figure 4.2 shows the measured zeroth-order transmission spectra for the 2D-MHA in two configurations. The spectral power of the transmitted THz wave is deduced from the temporal waveforms by fast Fourier transform algorithms. A view of the power spectra of THz signals transmitted through the device at various magnetic inclination angles,  $\phi$  and  $\theta$ , are shown in Fig. 4.2 (a) and (b), respectively. In

Fig. 4.2 (a), the effective refractive index of 5CB is constant. Besides  $\phi = 0^\circ$  and  $90^\circ$ , the polarization of THz wave rotates with  $\phi$  and the transmitted peak frequency should be fixed. The illusion of shift of peak frequency is due to the transmittance of e-ray is larger than o-ray. The results have good agreement with that. The experimentally obtained tuning range is 0.0047 THz as we vary  $\phi = 0^\circ$  and  $90^\circ$ . In Fig. 4.2 (b), the changes in peak frequency with  $\theta$ , or the effective refractive index of the 5CB, are evident. The transmitted THz waves show obviously blue shift for larger  $\theta$ . For the ideal case, if the LC substrate is infinite, the maximum tuning range using 5CB should then be  $\sim 0.02$  THz. Experimentally, the other group has previously shown that the frequency shift can be increased by using matching dielectric substrates on both side of the 2D-MHA [22].



The frequencies of the main transmission peaks of LC-filled 2D-MHA for o-ray (magenta trace in Fig. 4.2 (a)) and e-ray (black trace in Fig. 4.2 (a)), i.e., 5CB aligned perpendicular and parallel to the polarization of the incident THz wave, respectively, are red-shifted further to 0.193 THz and 0.188 THz. Using the refractive indices of 5CB ( $n_o = 1.57$  and  $n_e = 1.75$ ), we estimate that  $\nu_c = 0.200$  THz,  $\nu_{\text{diff}} = 0.222$  THz and  $\nu_{\text{spp}} = 0.191$  THz for the perpendicular geometry (o-ray). Similarly,  $\nu_c = 0.179$  THz,  $\nu_{\text{diff}} = 0.199$  THz and  $\nu_{\text{spp}} = 0.171$  THz for the parallel geometry (e-ray). Thus the observed peak transmission frequencies are close to that of the theoretical estimates.



As we change from the perpendicular (o-ray) to the parallel (e-ray) geometry, the peak transmission (see Fig. 4.2 (a)) increases from 0.58 to 0.70. As a THz wave filter, the insertion loss of the present device is thus 2.35 to 1.55 dB. Considering the porosity of the tunable 2D-MHA, 0.29, we observe an enhancement factor of 2.42.

The change in peak transmittance of the 2D-MHA by varying the effective refractive index of 5CB is shown in Fig. 4.3. The THz transmission peak increases with  $\theta$  for  $\theta < 30^\circ$ . This can be explained by how close the refractive index of LC matches that of Mylar. The ordinary and extraordinary refractive indices of 5CB are 1.57 and 1.75, respectively, at 0.3 THz. With increasing  $\theta$ , the effective refractive index of LC will descend from 1.75 to 1.70 (from  $\theta = 0^\circ$  to  $\theta = 30^\circ$ ) and the refractive index of Mylar substrate, which is 1.70. Over  $30^\circ$ ,  $n_d$  will decrease from 1.70 to 1.57 with increasing  $\theta$ . The transmission peak will then decrease according to the same theory.

Then the effect of thickness-dependence of 5CB layer and 2D-MHA was concerned. When the thickness of 5CB Layer and 2D-MHA were both increased to 500  $\mu\text{m}$ , the second peak emerged. The power transmittance of the sample is shown in Fig. 4.4. Owing to the complicated sample structure (5CB layer and 2D-MHA was sandwiched by 2 sheets of Mylar substrates), it was very difficult to analyze the phenomena which we obtained. So we decided to simplify the sample structure. Only use CRIL instead of 5CB, the refractive index of CRIL is not changed.

Based on the expression of SPP, enhanced transmission frequencies should be

independent of the hole material and thickness of 2D-MHA [8]. In SPP theory for our sample,  $\nu_{\text{diff}} = 0.349$  THz and  $\nu_c = 0.314$  THz. The zero-order transmission peak for the bare 2D-MHA at normal incidence is observed at 0.304 THz with a transmittance about 1, which is more than 3 times higher than that according to the porosity of the circular holes (0.29). When we filled CRIL (index of refraction are 1.7 and 1.58 in the THz region, with negligible dispersion and absorption), the transmission peaks have larger shift than filled LC. These are record in table 4.1. We can explain that the polarization of THz wave is changed in the holes of MHA. It is not pure linear polarized light, that is why we can not get theoretically large tunability in transmission peak by using LC.

## 4.5 Summary

Metal plates perforated with two-dimensional sub-wavelength holes arrays (2D-MHA) exhibit extraordinary transmission at selective THz frequencies. The transmittance is several times larger than the porosity of 2D-MHA plate. This mechanism of the enhanced transmission characteristic is attributed to the resonant coupling between the incident light and Surface Plasmon Polariton (SPP) which is located at the metal-dielectric interfaces. The shift of the transmission peak frequency can be realized by altering the adjacent material owing to the change of the resonant frequency of the SPP. We demonstrated a THz tunable filter by controlling the

refractive index of nematic liquid crystal (NLC) filling the holes and adjacent to the 2D-MHA on one side. Its index of refraction is varied by magnetically controlling birefringence of the NLC. With the NLC, the peak transmission frequency of the 2D-MHA shifts to the red by 0.112 THz and can be tuned from 0.193 THz to 0.188 THz. As a tunable THz filter, the device exhibits a continuously tuning range of 4.7 GHz, relatively low insertion losses of 2.35 to 1.55 dB. The maximum transmission of the device is well above (2.42 times) that according to the porosity of the holes and varies from 55% to above 70%. However, new phenomena appeared when holes of the 2D-MHA are filled with dielectric material. The effect of filling dielectric material into the holes cannot simply be explained by increased effective hole-diameter of the 2D-MHA. We experimentally investigate the role of material in the holes on transmission characteristics of the 2D-MHA. Theoretically speaking, the tuning range can be as high as 0.037 THz by employing matching LC substrates on both sides of the 2D-MHA and highly anisotropic LC materials. But we also understand the polarization state of THz wave is very complicated in the holes of MHA. In the last of this chapter, we measure six different MHAs. And all of the characteristic frequencies and structural parameters are list the in table 4.2. In table 4.2, the cutoff and diffractive frequencies are theoretic calculation and others are all recorded from experiments.

## References:

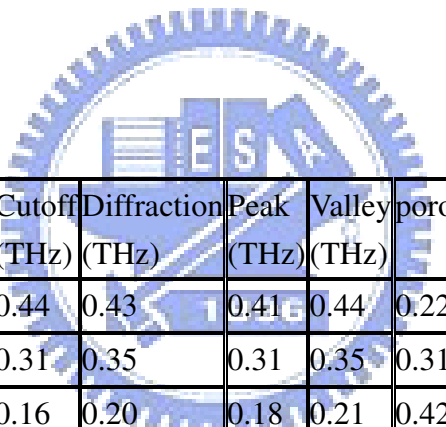
1. T. W. Ebbesen, H. J. Lezec, H. F. Ghaemi, T. Thio, and P. A. Wolff, *Nature* (London) **351**, 667, 1998..
2. H. F. Ghaemi, T. Thio, D. E. Grupp, T. W. Ebbesen, and H. J. Lezec, *Phys. Rev. B* **58**, 6779, 1998.
3. E. Popov, M. Nevière, S. Enoch, and R. Reinisc, *Phys. Rev. B* **62**,16100, 2000.
4. W. L Barnes, A. Dereux, and T. W. Ebbesen, *Nature* (London) **424**, 824, 2003.
5. D. E. Grupp, H. J. Lezec, T. W. Ebbesen, K. M. Pellerin and T. Thio, *Appl. Phys. Lett.* **77**, 1569 2000.
6. A. Krishnan, T. Thio, T. J. Kim, H. J. Lezec, T. W. Ebbesen, P. A. Wolff, J. B. Pendry, L. Martín-Moreno, and F. J. García-Vidal, *Opt. Commun.* **200**, 1, 2001.
7. L. Martín-Moreno, F. J. García-Vidal, H. J. Lezec, K. M. Pellerin, T. Thio, J. B. Pendry, and T. W. Ebbesen, *Phys. Rev. Lett.* **86**, 1114, 2001.
8. H. Raether, *Surface Plasmons on Smooth and Rough Surfaces and on Gratings* (Springer-Verlag, Berlin, 1988).
9. T. Thio, H. F. Ghaemi, H. J. Lezec, P. A. Wolff, and T. W. Ebbesen, *J. Opt. Soc. Am. B* **16**, 1743, 1999.
10. A. Degiron, H. J. Lezec, W. L. Barnes, T. W. Ebbesen, *Appl. Phys. Lett.* **81**, 4327, 2002.

11. T. J. Kim, T. Thio, T. W. Ebbesen, D. E. Grupp, and H. J. Lezec, *Opt. Lett.* **24**, 256, 1999.
12. T. K. Wu, *Frequency Selective Surface and Grid Array* (Wiley, New York, 1995).
13. C. Winnewisser, F. T. Lewen, M. Schall, M. Walther, and H. Helm, *IEEE Trans. Microwave Theory Tech.* **48**, 744, 2000.
14. H. Cao and A. Nahata, *Opt. Exp.* **12**, 1004, 2004.
15. D. Qu, D. Grischkowsky, and W. Zhang, *Opt. Lett.* **29**, 896, 2004.
16. J. Gómez Rivas, C. Schotsch, P. Haring Bolivar, and H. Kurz, *Phys. Rev. B* **68**, 201306 2004.
17. J. Gómez Rivas, P. Haring Bolivar, H. Kurz, *Opt. Lett.* **29**, 1680, 2004.
18. T. D. Drysdale, I. S. Gregory, C. Baker, E. H. Linfield, W. R. Tribe, D. R. S. Cumming, *Appl. Phys. Lett.* **85**, 5173, 2004.
19. H. Némec, P. Kužel, L. Duvillaret, A. Pashkin, M. Dressel, M. T. Sebastin, *Opt. Lett.* **30**, 549, 2005.
20. R. P. Pan, C. F. Hsieh, C. L. Pan and C. Y. Chen, *J. Appl. Phys.*, **103**, 093523, 2008.
21. F. Miyamaru, M. Hangyo, *Appl. Phys. Lett.* **84**, 2742, 2004.
22. M. Tanaka, F. Miyamaru, and M. Hangyo, *Opt. Lett.* **30**, 1210, 2005.

## Tables

Refractive index	Peak freq (THz)
CRIL( $n=1.70$ )	1 <sup>st</sup> : 0.183
CRIL( $n=1.58$ )	1 <sup>st</sup> : 0.198
5CB( $n_e=1.75$ )	1 <sup>st</sup> : 0.189
5CB( $n_o=1.57$ )	1 <sup>st</sup> : 0.192

Table 4.1 THz transmitted peak frequency of MHA filled with 5CB or CRIL layer.



sample	Diameter (mm)	Spacing (mm)	Cutoff (THz)	Diffraction (THz)	Peak (THz)	Valley (THz)	porosity	Transmittance	enhancement	$v_d/v_c$
A (H)	0.40	0.81	0.44	0.43	0.41	0.44	0.22	0.43	1.91	0.98
B (H)	0.57	0.98	0.31	0.35	0.31	0.35	0.31	0.93	3.04	1.13
C (R)	1.09	1.50	0.16	0.20	0.18	0.21	0.42	1.00	2.41	1.25
D (H)	0.80	1.19	0.22	0.29	0.23	0.29	0.41	0.91	2.21	1.32
AA (H)	0.43	0.80	0.41	0.43	0.40	0.44	0.26	0.70	2.69	1.05
BB (H)	0.50	0.89	0.35	0.39	0.35	0.40	0.29	1.00	3.45	1.11

Table 4.2 The characteristic frequencies and structural parameters of six different

MHAs. H and R represent the hexagonal and rectangular lattice, respectively.

## Figures:

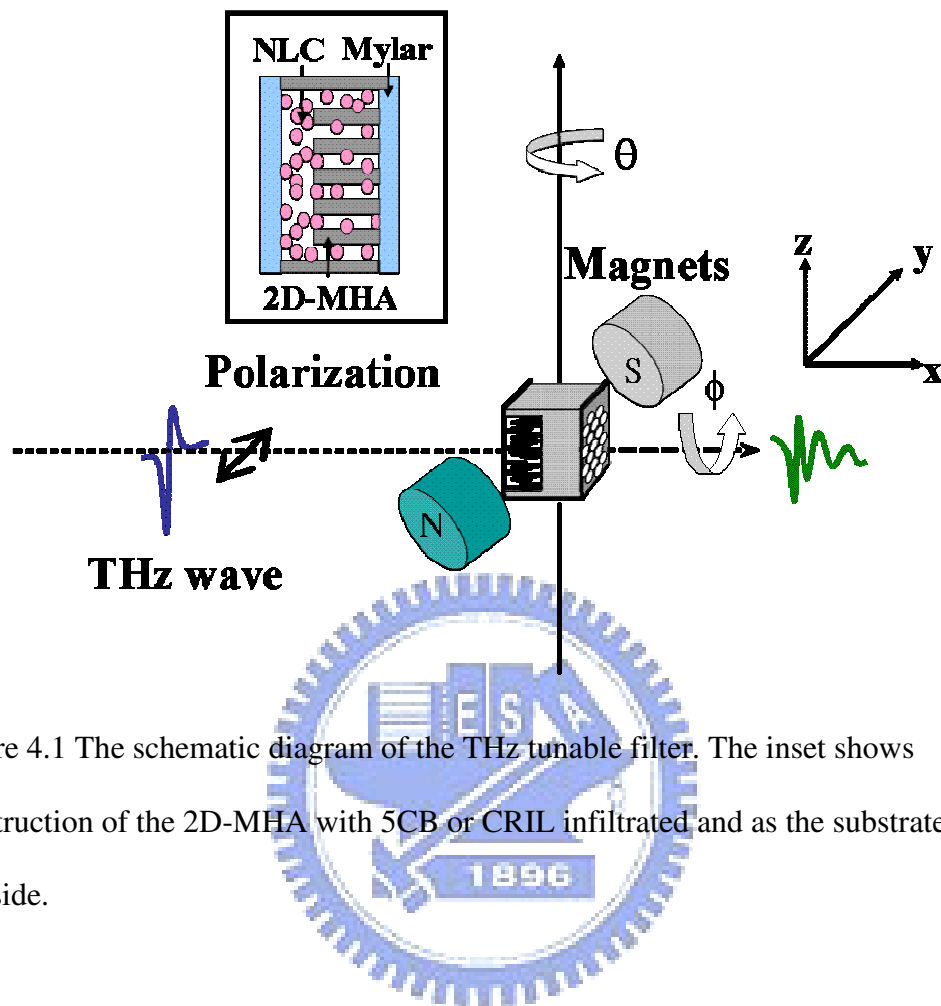


Figure 4.1 The schematic diagram of the THz tunable filter. The inset shows construction of the 2D-MHA with 5CB or CRIL infiltrated and as the substrate on one side.

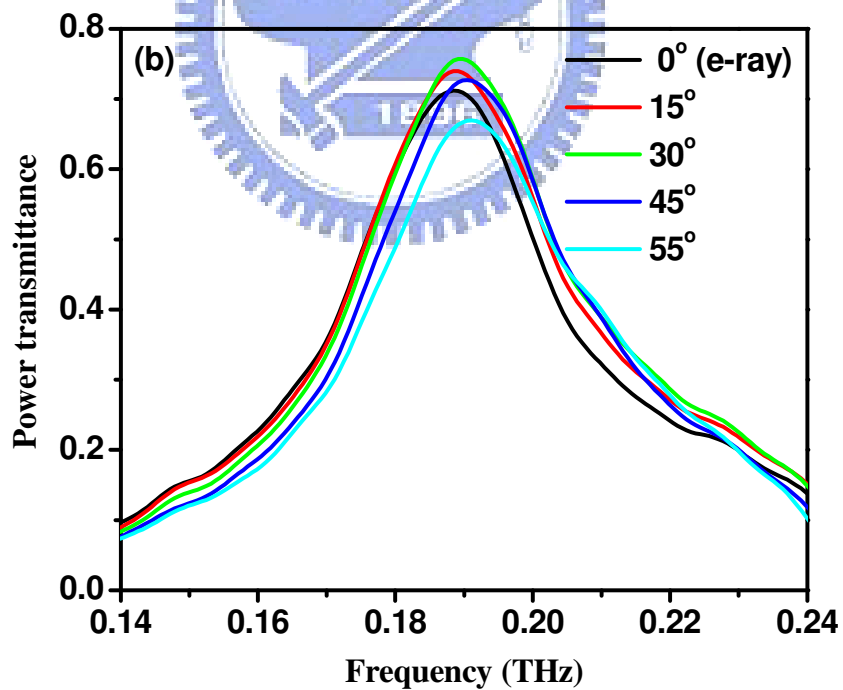
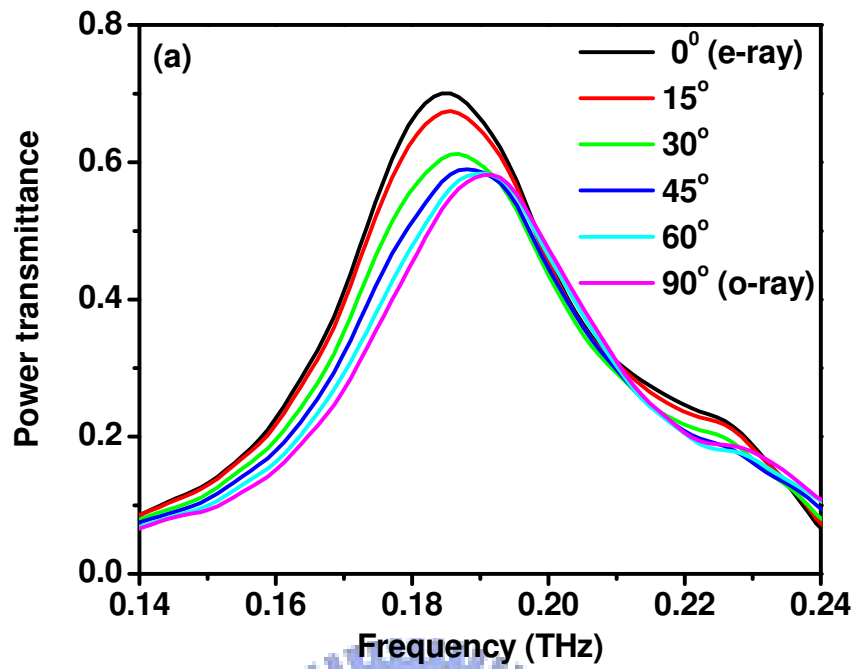


Figure 4.2 The power spectra of THz signals transmitted through the device at various magnetic inclination angles. The rotation axis in (a) and (b) is X and Z, respectively.



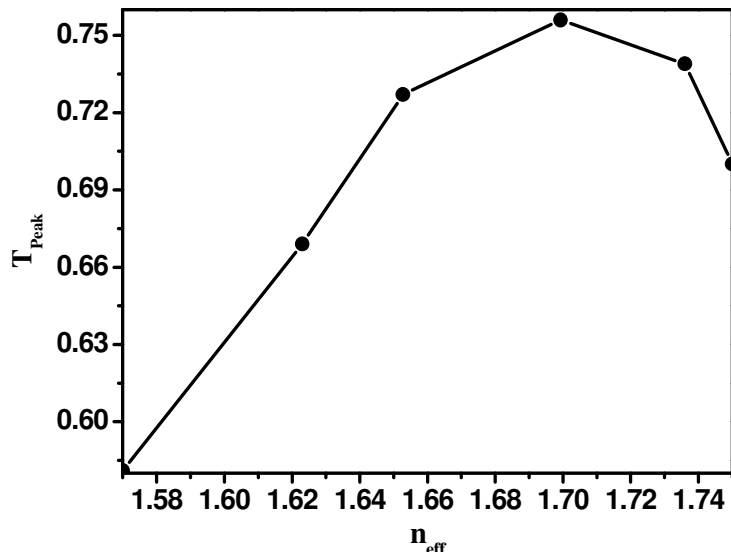


Figure 4.3 The peak transmittance  $T_{peak}$  of the 2D-MHA is plotted as a function of the effective refractive index of 5CB.

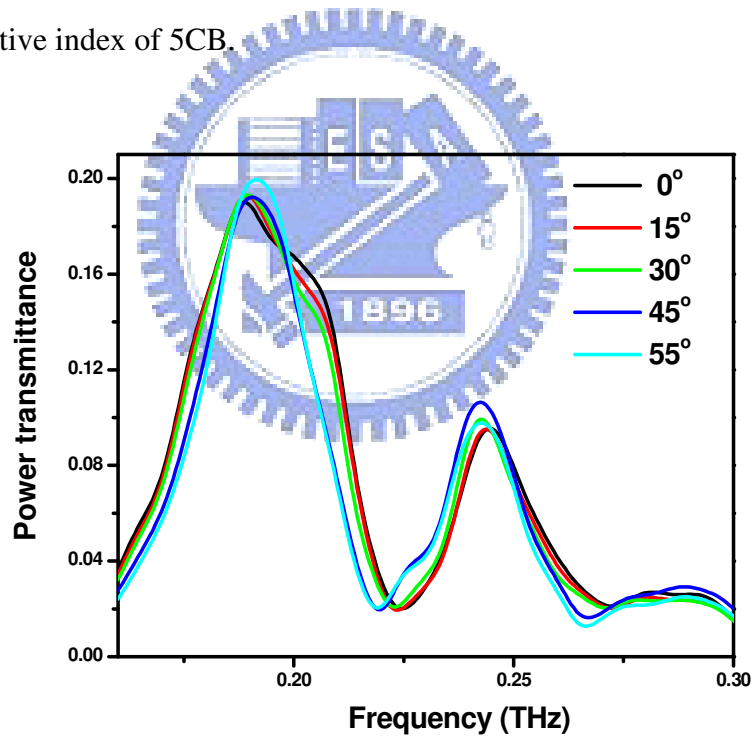


Figure 4.4 The transmitted spectrum of the broadband THz pulse through the 2D-MHA with 5CB layer, obtained by taking the FFT of the time-domain transmitted THz signal, and normalized to the air reference. Both of the thickness of 5CB and 2D-MHA are 500  $\mu\text{m}$ .

# Chapter 5 A Liquid-Crystal-Based Tunable Terahertz Achromatic Quarter-Wave Plate

An achromatic tunable terahertz birefringence quarter-wave plate is demonstrated. Standard birefringent wave plates can be exploited only at a specific frequency. The phase retardation of this device is  $90^\circ \pm 9^\circ$  from 0.20 to 0.50 THz and could be changed the operation range from 0.30 to 0.70 THz by using magnetically controlled birefringence in three nematic liquid crystals phase retarders. The insertion loss of the present device is about 8 dB.

## 5.1 Achromatic Quarter-Wave Plate

Terahertz (THz) science ranges from investigations of ultrafast dynamics in materials to biological tissue imaging [1-3]. In the past two decades, the development of ultrashort pulse (femtosecond) lasers and advanced optoelectronic THz-devices create a new era of THz technologies. As a result of the increasing importance of these techniques, quasi-optic components such as phase shifters, gratings, polarizers and filters are indispensable. We have demonstrated a room temperature THz phase shifters based on magnetically or electrically controlled birefringence in NLCs [4, 5]. These devices are capable of more than  $360^\circ$  of phase shift around 1 THz. However, traditional birefringent wave plates can be used only at a single corresponding

frequency, because the phase retardation has strongly wavelength dependence [6]. Several types of achromatic phase retarders have been demonstrated of late. In the infrared, R. M. A. Azzam and Cristina L. Spinu reported achromatic dephasing properties of total reflection in Si-SiO<sub>2</sub> interface [7]. In the visible range, others demonstrated achromatic wave plates by using gratings [8, 9] and twisted nematic liquid crystals (LC) [10]. For THz wave device, it is too thick to align twisted nematic LCs by boundary due to scale of THz wavelength. From the above-mentioned works, we know that the combination of two or more wave plates of different retardations can allow partial cancellation between the dispersion of these materials [11].

## 5.2 Experiment

In this work, we have constructed and characterized a LC based THz achromatic quarter-wave plate that is insensitive to the wavelength which can be tuned by changing the effective refractive index of LC. The design of this device is based on the idea from S. Pancharatnam [12]. It consists of a standard half-wave plate and two standard third-wave plates. The critical concept is the partial cancellation of the change of retardation from each wave plate with respect to the frequency. To shift THz operation range, we extended the design to a combination of three magnetically controlled LC phase retarders. Nematic LC E7 is reasonably transparent in the THz range [4] and it also exhibits large birefringence. In THz frequency, the ordinary and

extraordinary refractive indices of E7 are  $n_o=1.58$  and  $n_e=1.71$ , respectively [4]. The corresponding imaginary indices are  $\kappa_o$  (0.01) to  $\kappa_e$  (0.007). Each LC wave plate is described by its corresponding Jones matrix  $J_i$  ( $i=A, B$  and  $C$ ) [13],

$$J_i(\Gamma_i, \psi_i) = R \begin{pmatrix} \cos \psi & -\sin \psi \\ \sin \psi & \cos \psi \end{pmatrix} \begin{pmatrix} e^{-i\Gamma/2} & 0 \\ 0 & e^{i\Gamma/2} \end{pmatrix} R \begin{pmatrix} \cos \psi & \sin \psi \\ -\sin \psi & \cos \psi \end{pmatrix} \\ = \begin{bmatrix} \cos \frac{\Gamma_i}{2} - i \cos 2\psi_i \sin \frac{\Gamma_i}{2} & i \sin 2\psi_i \sin \frac{\Gamma_i}{2} \\ i \sin 2\psi_i \sin \frac{\Gamma_i}{2} & \cos \frac{\Gamma_i}{2} + i \cos 2\psi_i \sin \frac{\Gamma_i}{2} \end{bmatrix}, \quad (5.1)$$

which the phase retardation  $\Gamma_i$  and the orientation angle  $\psi_i$  with respect to the optical axis are two key parameters in Eq. (5.1). The total Jones matrix of achromatic wave plate is given by [14],

$$J = \prod_i J_i = \begin{bmatrix} A & B \\ -B^* & A^* \end{bmatrix}, \quad (5.2)$$

and the total resulting retardation is obtained by

$$t \tan^2 \frac{\Gamma}{2} = \frac{|\text{Im } A|^2 + |\text{Im } B|^2}{|\text{Re } A|^2 + |\text{Re } B|^2}. \quad (5.3)$$

For LC wave plates, the inclination angle,  $\theta$ , is defined as the angle between the director of LC molecules and the polarization direction of electromagnetic wave. The effective refractive index of LC changes with the LC molecular orientation [15], which is corresponding to the angle  $\theta$ . The phase retardation,  $\Gamma_i(\theta)$ , due to magnetically controlled birefringence is given by

$$\Gamma_i(\theta) = \int_0^d \frac{2\pi f}{c} \Delta n_i(\theta, z) dz, \quad (5.4)$$

where  $d$  is the thickness of LC layer,  $\Delta n_i$  is the change of effective birefringence,  $f$  is the frequency of the THz waves and  $c$  is the speed of light in vacuum.

If the magnetic field is large enough such that the LC molecules are reoriented parallel to the magnetic field. The phase retardation,  $\Gamma_i(\theta)$ , in Eq.(5.4) can then be re-written as

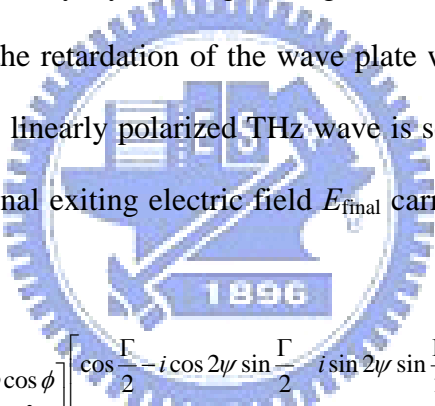
$$\Gamma_i(\theta) = 2\pi d \frac{f}{c} \left\{ \left[ \frac{\cos^2(\theta)}{n_e^2} + \frac{\sin^2(\theta)}{n_o^2} \right]^{-\frac{1}{2}} - n_o \right\}, \quad (5.5)$$

where  $n_o$  and  $n_e$  are the ordinary and extra-ordinary refractive indices of the LC. As expected, the tunable operation range of achromatic quarter wave plate is achieved by using three magnetically controlled LC retarders.

The LC-based achromatic wave plate has three elements, A, B and C, which are shown in Fig. 5.1. Each tunable retarder (TR) consists of a pair of rotatable permanent magnets and a homeotropically aligned LC cell. The LC cell in the TR was constructed with two fused silica substrates and filled with NLC, E7 (Merck). The substrates of LC cells were coated with N,N-dimethyl-n-octadecyl-3-aminopropyltrimethoxysilyl chloride (DMOAP) for homeotropic alignment [16]. Thicknesses of LC layers in TR<sub>A</sub>, TR<sub>B</sub> and TR<sub>C</sub> were  $d_A = 2.56$  mm,  $d_B = 3.86$  mm, and  $d_C = 2.56$  mm, controlled by Teflon spacers. The threshold field required to reorient LC molecules with the magnetic field is less than 0.004 Tesla [15]. The maximum magnetic field at cell position in the rotary permanent magnets (sintered Nd-Fe-B) is 0.25 Tesla. Sufficiently large magnetic field is applied for stable homogeneous alignment of LC molecules in the thick LC cell. The rotation axis of rotary magnets is perpendicular to the propagation direction of the THz wave and has an azimuthal angle  $\rho_i$  with respect to the normal axis of the table ( $\rho_A = 0^\circ$ ,  $\rho_B = 20^\circ$  and  $\rho_C = 0^\circ$ ). So TR<sub>A</sub>, TR<sub>B</sub>, and TR<sub>C</sub> are used to achieve the desired variable phase retardation,  $\Gamma_A(\theta)$ ,  $\Gamma_B(\theta)$  and  $\Gamma_C(\theta)$ . The TRs were placed between a pair of wire-grid polarizers (Specac, No. GS57204). We set the polarizer at fixed azimuthal

angle  $\rho_p = -75^\circ$ , it made the optic axis of achromatic quarter wave plate has  $45^\circ$  with respect to the polarization direction of THz wave in our photoconductive-antenna-based THz time-domain spectrometer (THz-TDS) [17]. In this work, the rotation angle  $\theta = 0^\circ$  and  $\theta = 30^\circ$  for all TRs were demonstrated. The corresponding birefringence of LCs is 0.13 and 0.095, respectively. By rotating the magnetic field, the operation frequency range was shifted for that corresponding retardations were equal to quarter wave.

Photoconductive-antenna-based THz-TDS only can detect the linear polarized THz field. To measure the retardation of THz LC based quarter wave plate, we introduced a new method of ellipsometry by rotating wire grid analyzer [18]. This technique allows determination of the retardation of the wave plate without rotating or moving the detector. A horizontal linearly polarized THz wave is sent through the wave plate to be investigated. The final exiting electric field  $E_{final}$  carries out information on the wave plate as follows



$$E_{final}(\phi) = \begin{bmatrix} 1 & 0 \\ 0 & 0 \end{bmatrix} \begin{bmatrix} \cos^2 \phi & \sin \phi \cos \phi \\ \sin \phi \cos \phi & \sin^2 \phi \end{bmatrix} \begin{bmatrix} \cos \frac{\Gamma}{2} - i \cos 2\psi \sin \frac{\Gamma}{2} & i \sin 2\psi \sin \frac{\Gamma}{2} \\ i \sin 2\psi \sin \frac{\Gamma}{2} & \cos \frac{\Gamma}{2} + i \cos 2\psi \sin \frac{\Gamma}{2} \end{bmatrix} \begin{bmatrix} \cos^2 15^\circ & -\sin 15^\circ \cos 15^\circ \\ -\sin 15^\circ \cos 15^\circ & \sin^2 15^\circ \end{bmatrix} \begin{bmatrix} 1 \\ 0 \end{bmatrix}$$

$$P_{exp}(\phi) = (E_{final}(\phi))^2, \quad (5.6)$$

where  $\phi$  is the angle between the analyzer with respect to the detecting direction of antenna. And  $P_{exp}(\phi)$  is the power of THz wave which can be obtained from experimental measurement. We can extract the phase retardation of our device by using Eq. (5.6).

### 5.3 Result

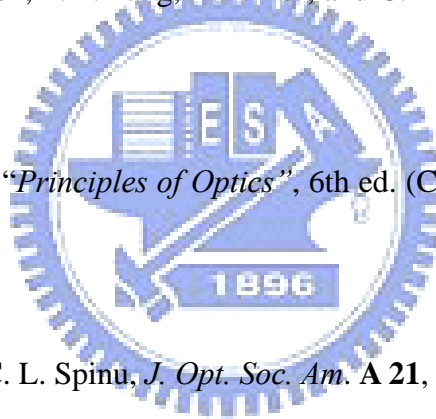
The signal has been recorded in steps of  $15^\circ$  of the analyzer angle  $\phi$ , leading to 24 times. The temporal waveforms of the THz pulse transmitted through the tunable achromatic quarter wave plate with the E7 layer aligned at magnetic inclination angle  $\theta = 0^\circ$  with different rotating angles  $\phi$  are shown in Fig. 5.2. The transmitted

amplitude of THz fields exhibit symmetry with respect to  $\phi = 0^\circ$  in time domain, because the most of transmitted broadband THz signals are circular polarized and only horizontal polarization of THz wave can be detected by photoconductive antenna. Then, power spectral data can be achieved by using fast Fourier transform of the temporal data. In Fig. 5.3, the transmittance values with different  $\phi$  (when  $\theta = 0^\circ$ ) are drawn with theoretic prediction at frequency of 0.44 THz. The experimental retardations obtained with the combination of the three LC plates at  $\theta = 0^\circ$  and  $\theta = 30^\circ$ , depicted in Fig. 5.4 and 5.5, respectively. In Fig. 5.4, the phase retardation of this device is about  $90^\circ$  from 0.20 to 0.50 THz, when  $\theta = 0^\circ$ . And in Fig. 5.5, the phase retardation of this device is about  $90^\circ$  from 0.30 to 0.70 THz, when  $\theta = 30^\circ$ . The operation THz frequency range have been shifted by rotating the magnet set. The experimental data and the theoretical curves from the Jones matrices calculation are in very good agreements.

In summary, we have demonstrated for the first time an achromatic tunable THz birefringence quarter-wave plate using liquid crystal cells as the birefringent elements. The phase retardation of this device is  $90^\circ \pm 9^\circ$  from 0.20 to 0.50 THz and could be tuned the operation range from 0.30 to 0.70 THz by using magnetically controlled birefringence in three nematic liquid crystals retards. The insertion loss of the present device is about 8 dB. The experimental data are in good agreements with theoretical predictions. To achieve the much larger bandwidth in THz frequency range, one can extend the design to a combination of more wave plates.

## References:

1. D. Mittleman, ed., “*Sensing with Terahertz Radiation*” (Springer-Verlag, Berlin, 2003).
2. P. H. Siegel, *IEEE Trans. Microwave Theory Tech.* **50**, 910, 2002.
3. B. Ferguson and X.-C. Zhang, *Nature Materials*, **1**, 26, 2002.
4. C. Y. Chen, C. F. Hsieh, Y. F. Lin, R. P. Pan, and C. L. Pan, *Opt. Exp.*, **12**, 2625, 2004.
5. H. Y. Wu, C. F. Hsieh, T. T. Tang, R. P. Pan, and C. L. Pan, *IEEE Photonic Tech. Lett.*, **18**, 2006.
6. M. Born and E. Wolf, “*Principles of Optics*”, 6th ed. (Cambridge University Press, 1997).
7. R. M. A. Azzam and C. L. Spinu, *J. Opt. Soc. Am. A* **21**, 2019, 2004.
8. N. Bokor, R. Shechter, N. Davidson, A. A. Friesem, and E. Hasman, *Appl. Opt.* **40**, 2076, 2001.
9. G. P. Nordin and P. C. Deguzman, *Opt. Exp.* **5**, 163, 1999.
10. S. Shen, J. She, and T. Tao, *J. Opt. Soc. Am. A* **22**, 961, 2005.
11. J. M. Beckers, *Appl. Opt.* **10**, 973, 1971.
12. S. Pancharatnam, *Proc. of the Indian Academy of Sciences*, **41**, 130, 1955.
13. R. C. Jones, *J. Opt. Soc. Am.* **31**, 488, 1941.





14. H. Hurwitz and R. C. Jones, *J. Opt. Soc. Am.* **31**, 493, 1941.
15. P. G. de Gennes and J. Prost, “*The Physics of Liquid Crystals*”, 2nd ed. (Oxford, New York, 1983), Chap. 3
16. F. J. Kahn, *Appl. Phys. Lett.* **22**, 386, 1973.
17. C. L. Pan, C. F. Hsieh, and R. P. Pan , M. Tanaka, F. Miyamaru, M. Tani, and M. Hangyo, *Opt. Exp.* **13**, 3921, 2005.
18. Jean-Baptiste Masson and Guilhem Gallot, *Opt. Lett.*, **31**, 265, 2006.





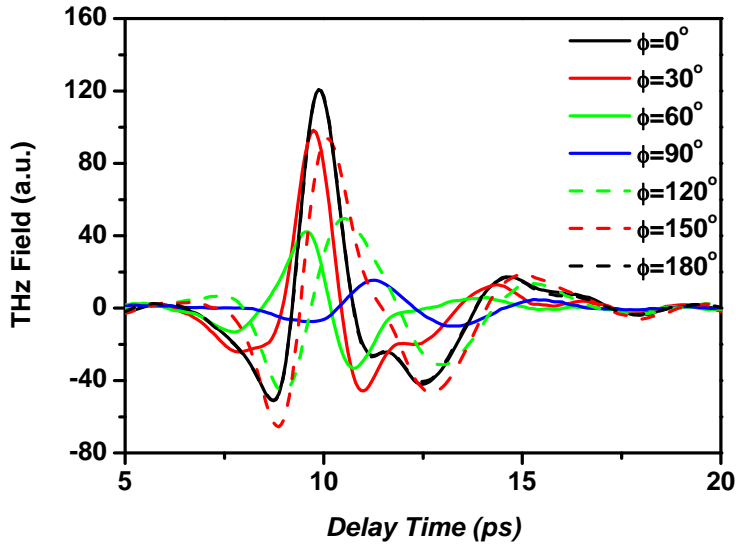


Figure 5.2 The temporal waveforms of the THz pulse transmitted through the tunable achromatic quarter wave plate with the E7 layer aligned at magnetic inclination angle  $\theta = 0^\circ$  with different rotating angles  $\phi$  are shown together. Here we just show the temporal waveforms at  $\phi = 0^\circ, 30^\circ, 60^\circ, 90^\circ, 120^\circ, 150^\circ$  and  $180^\circ$ .

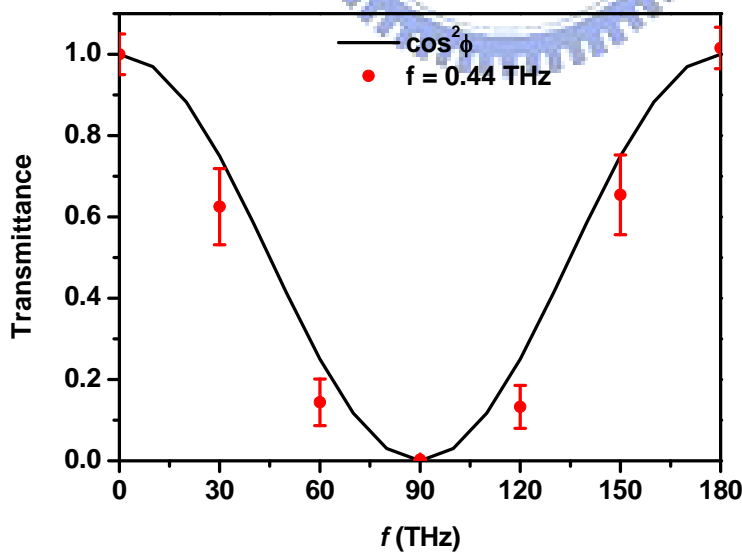


Figure 5.3 The transmittance values with different  $\phi$  (when  $\theta = 0^\circ$ ) are drawn together with theoretic prediction at frequency of 0.44 THz.

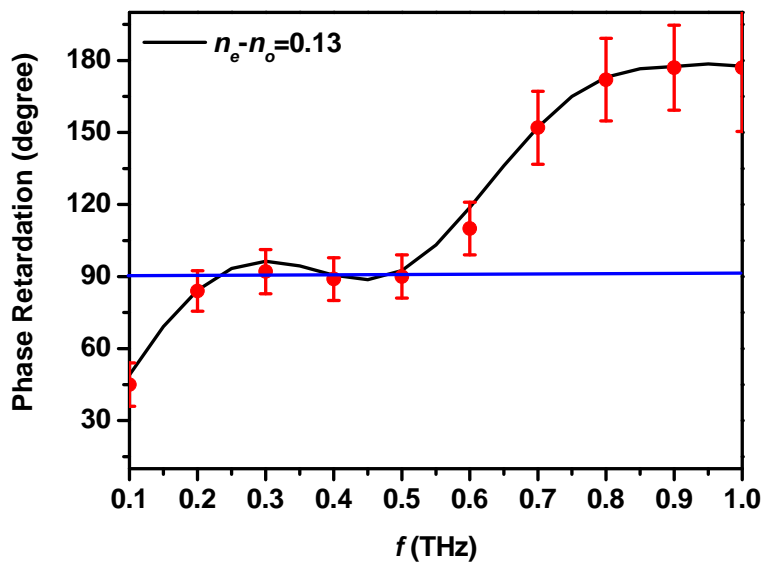


Figure 5.4 The phase retardation of this device is about  $90^\circ$  from 0.20 to 0.50 THz,

when  $\theta = 0^\circ$ .

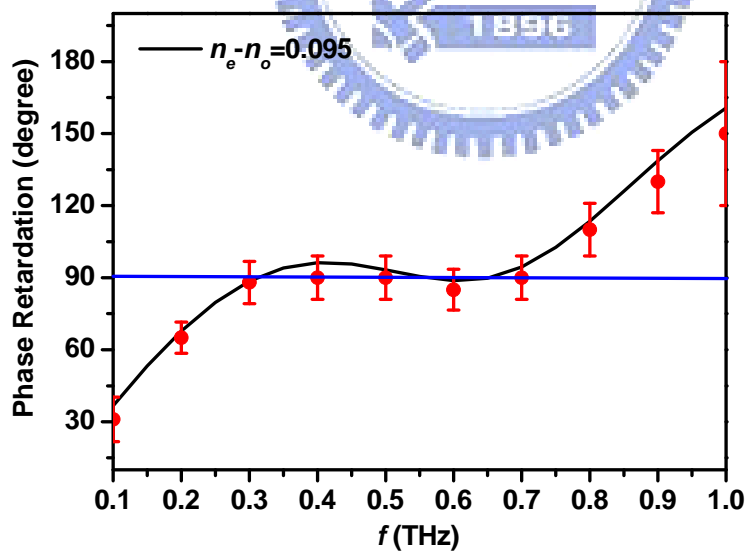


Figure 5.5 The phase retardation of this device is about  $90^\circ$  from 0.30 to 0.70 THz,

when  $\theta = 30^\circ$ .

## Chapter 6 Conclusion

In conclusion, we report the frequency dependence and the temperature dependence of the optical constants of PCH-5 in the nematic phase by using THz time-domain spectroscopy. The behavior of temperature dependence of PCH-5 is quite similar to it in visible range. The temperature dependent birefringence, which relates to the order parameter has also been reported. And we also measure the frequency dependence of the optical constants of E7 in nematic phases at room temperature. We found that the imaginary part of refractive index of PCH-5 and E7 are relatively small and without resonant sharp absorption and clear dispersion in the frequency range of 0.2 to 1.0 THz. By using thick E7 layer, we can obtain the  $\kappa_o$  is larger than  $\kappa_e$  in THz frequency range. The studies of the optical constants of E7 in THz range show the attractive potential of the applications in this range, such as phase shifter and wave plate, due to the comparable large birefringence and relative small imaginary part of refractive index.

For the tunable phase shifter, we have demonstrated the magnetically and electrically controlled tunable LC THz phase shifters. A maximum phase shift of  $368^\circ$  at 1.03 THz has been achieved successfully by using mechanical magnets. The phase shift can be continuously tuned magnetically by controlling the effective refractive index of LC layer. And a maximum phase shift of  $367^\circ$  at 1.05 THz is realized by using electrically controlled birefringence in a homeotropically aligned nematic LC (E7) dual cell, 1012  $\mu\text{m}/\text{layer}$  in thickness. The driving voltage required for a phase shift of  $367^\circ$  is 45 V (rms). The double-homeotropic cell has better figure of merit about  $40 \text{ degree}/^\circ\text{B}$ . The results are in good agreement with theoretical predictions.

As for the tunable filter, we demonstrated a THz tunable filter by controlling the refractive index of NLC filling the holes and adjacent to the 2D-MHA on one side. Its index of refraction is varied by magnetically controlling birefringence of the NLC. With the NLC, the peak transmission frequency of the 2D-MHA shifts to the red by 0.112 THz and can be tuned from 0.193 THz to 0.188 THz. The device exhibits a continuously tuning range of 4.7 GHz, relatively low insertion losses of 2.35 to 1.55 dB. The maximum transmission of the device is well above (2.42 times) that according to the porosity of the holes and varies from 55% to above 70%.

Nonetheless, traditional birefringent devices can be used only at a single corresponding frequency, because the phase retardation has strong wavelength dependence. We have demonstrated for the first time an achromatic tunable THz birefringence quarter-wave plate by using LC cells as the birefringent elements. The phase retardation of this device is  $90^\circ \pm 9^\circ$  from 0.20 to 0.50 THz and could be tuned the operation range from 0.30 to 0.70 THz by using magnetically controlled birefringence in three NLC retards. The insertion loss of the present device is about 8 dB. The experimental data are in good agreements with theoretical predictions. To achieve the much larger bandwidth in THz frequency range, one can extend the design to a combination of more wave plates.

In the future, we want to find the LCs, which possesses larger birefringence or lower absorption for developing the new LC-based THz achromatic devices.

# Appendix Sample dimensions

## Chapter 2

Sample	Substrate	LC layer (d)
PCH-5	3.32 mm	617 $\mu\text{m}$
E7	3.32 mm	8.087 mm
Reference	3.00 mm	

## Chapter 3

Applied magnetic sample	Area	LC	LC layer (d)
Double VA cell	1.0 cm by 1.0 cm	E7	1.50*2 mm
Single VA cell	1.0 cm by 1.0 cm	5CB	1.32 mm
Single VA cell	1.0 cm by 1.0 cm	5CB	0.93 mm

Applied electric sample	Area	LC	LC layer (d)	Spacing of electrodes (L)
Double VA cell	1.0 cm by 1.0 cm	E7	1012*2 $\mu\text{m}$	10.2 mm
Single VA cell	1.0 cm by 1.0 cm	E7	1830 $\mu\text{m}$	11.0 mm
Single VA cell	1.0 cm by 1.0 cm	E7	570 $\mu\text{m}$	11.9 mm
Single hybrid cell	1.0 cm by 1.0 cm	E7	1019 $\mu\text{m}$	12.2 mm

## Chapter 4

2D-MHA	Thickness (t)	Lattice constant (s)	Diameter of hole (d)	LC
	0.5 mm	0.99 mm	0.56 mm	5CB

## Chapter 5

Wave plate	Retardation for 0.3THz	LC	LC layer (d)	Area
TR <sub>A</sub>	$\lambda/3$	E7	2.56 mm	$\pi \text{ cm}^2$
TR <sub>B</sub>	$\lambda/2$	E7	3.86 mm	$\pi \text{ cm}^2$
TR <sub>C</sub>	$\lambda/3$	E7	2.56 mm	$\pi \text{ cm}^2$